Invasion of Heterogeneous Breast Cancer Spheroids in Collagen Matrices

An in Vitro Study to Explore the Impact of ECM Porosity and Source on Heterogeneous Tumor Spheroid Invasion

Ayesha Bhairo

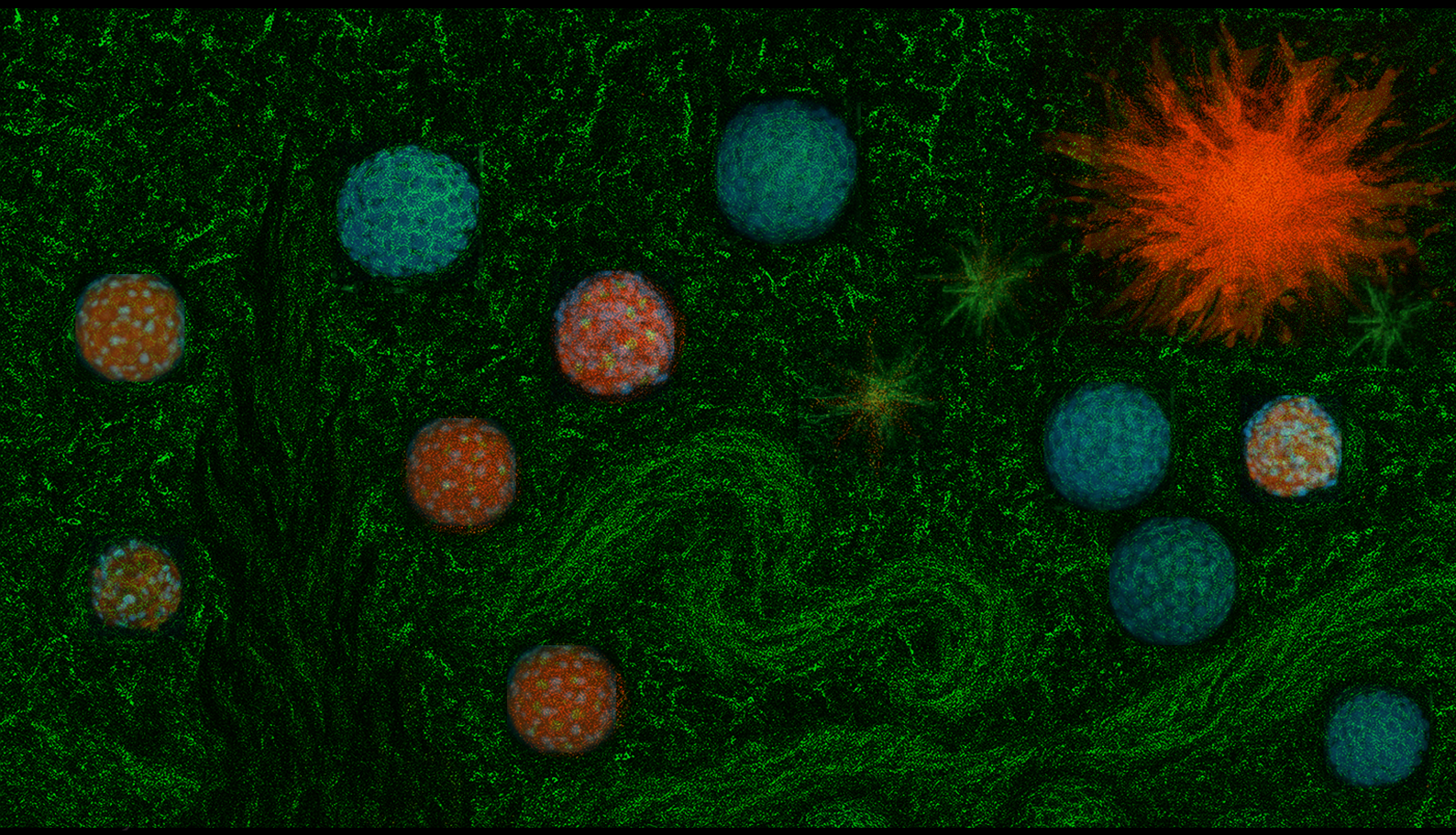

TU Delft

Invasion of Heterogeneous Breast Cancer Spheroids in Collagen Matrices

An in Vitro Study to Explore the Impact of ECM Porosity and Source on Heterogeneous Tumor Spheroid Invasion

by

Ayesha Bhairo

to obtain the degree of Master of Science in Chemical Engineering
at the Delft University of Technology,
to be defended publicly on Wednesday July 9, 2025 at 13:00.

Student number:	4540808	
Project duration:	November 20, 2024 – July 9, 2025	
Thesis committee:	Dr. P. Boukany,	TU Delft, supervisor
	Prof. Dr. G. Koenderink,	TU Delft, committee member
	Dr. R. Eelkema,	TU Delft, committee member
Daily supervisor:	MSc. S. Smink,	TU Delft

An electronic version of this thesis is available at http://repository.tudelft.nl/.

TU Delft

Abstract

Triple Negative Breast Cancers (TNBCs) account for 20% of breast cancer cases and are characterized by poor prognosis and limited treatment options. The Tumor Microenvironment (TME), particularly the collagen-rich Extracellular Matrix (ECM), plays a critical role in TNBCs progression. Collagen remodeling, including fiber realignment and degradation, significantly influences cancer cell adhesion, migration, and invasion.

Given the importance of collagen in modulating tumor invasion, this study investigates how collagen matrix porosity regulates the invasive behavior of 3D breast cancer cell clusters, spheroids. Spheroids composed purely of breast cancer cells, purely of fibroblast cells, and mixed spheroids containing both cell types in equal proportions, are used to mimic the TME. Spheroid behavior was examined in collagen gels of varying concentrations (1.5 and 4.0 mg/mL for rat tail collagen, and 2.4 and 3.3 mg/mL for bovine collagen). The size and number of pores in the collagen gels were quantified, and changes in spheroid growth and morphology patterns were monitored over time.

Invasion was most pronounced in low-concentration gels with larger pores (1.5 mg/mL rat tail; 2.4–3.3 mg/mL bovine). Breast cancer-only spheroids were most invasive, fibroblast-only were least invasive, and mixed spheroids showed intermediate behavior more closely resembling that of the fibroblast-only spheroids. In contrast, invasion was greatly restricted in the 4.0 mg/mL rat tail collagen due to reduced porosity and denser networks which acted as physical barriers for all three spheroid types.

These results highlight collagen porosity as a key factor in TNBCs invasion. This has important implications for designing physiologically relevant in vitro tumor models that better capture the complexity of the ECM in cancer progression.

Acknowledgments

Ayesha Bhairo
Delft, July 2025

Completing this thesis comes with a mix of emotions: it has been both challenging and deeply rewarding. A wild ride involving long days in the lab, and longer nights trying to analyze the results; with plenty of head-scratching, a few meltdowns, and the occasional small victory that made me want to dance in my lab coat. The process taught me not only technical skills, but also patience, resilience, critical thinking, and that science is definitely a team sport.

Therefore I would like to thank my supervisor Dr. Pouyan Boukany, for making this project possible and for his invaluable guidance throughout. I'll admit, I often came into our meetings feeling confident in my ideas, only to leave rethinking most of them. But those conversations challenged me in the best way, pushing me to approach problems more critically. I would also like to sincerely thank my daily supervisor Simone Smink, who experienced all the highs and lows of this project with me, and graciously endured my enthusiastic messages whenever I had successfully transferred spheroids. The countless brainstorming sessions and invaluable guidance were essential throughout this journey. Truly, I could not have completed this work without your support, and I am deeply grateful for your steadfast commitment. A special thank you to Ir. Anouk van der Net for generously taking the time to discuss bovine collagen, and providing a way to continue the project with almost no delay. I am deeply grateful for your support, including your prompt and helpful email correspondence. I would also like to thank Kristen David for guiding me through the lab techniques and for the insightful discussions along the way. And a heartfelt thanks to Sophie de Boer for listening to my frustrations and offering support.

I would also like to thank my friends who have been with me throughout this emotional rollercoaster. I truly don't think I could have completed this project without their unwavering support. My gratitude goes out to Anirudh and Sereno, for helping me make it through this challenging program. A special thanks to Jessy for being there every step of the way and for listening to my endless complaints and frustrations, I enjoyed listening to yours as well. Robin, Paul, Monique, and Thirza, whose support has been essential to who I am today. Your kindness has meant more to me than words can express, and I will carry your encouragement with me always.

Finally, I want to express my deepest gratitude to my family for their unwavering love and support throughout this journey. Mom and Dad, thank you for setting such a strong example of perseverance and dedication. Bik and Nani, thank you for the peptalks that kept me going when things got tough. Raoul and Sara, it was comforting to navigate similar challenges together. Although Raoul, you were not always relatable, your presence still meant a lot. Grace and Jira, thank you for welcoming me into your family with open arms and for your kindness and support throughout this journey. Sas and Tahira, I truly appreciate your love and encouragement throughout all these years every step of the way. And last but certainly not least, my Bugs and CheRo, you've been my steady anchors and my greatest comfort, your unwavering love and support have meant more to me than words could ever express. Bugs, I also want to apologize for the many moments of frustration you had to endure, your patience deserves a medal.

It has been a long road filled with challenges, growth, and unforgettable moments. Looking back, I'm grateful not just for reaching the destination, but for everything the journey has taught me along the way.

Contents

List of Abbreviations

BM	Basement Membrane.
CAFs	Cancer-Associated-Fibroblasts.
CSC	Cancer Stem Cells.
CXCR4	CXC Chemokine Receptor-4.
ECM	Extracellular Matrix.
EMT	Epithelial-to-Mesenchymal Transition.
ER	Estrogen Receptor.
HCCG	High Concentration Collagen Gel.
HER2	Human Epidermal Growth Factor Receptor 2.
IGF II	Insulin-like Growth Factor II.
LCCG	Low Concentration Collagen Gels.
MCS	Multicellular spheroids.
MMPs	Matrix Metalloproteinases.
NAFs	Normal-Associated-Fibroblasts.
PR	Progesterone Receptor.
SDF-1	Stromal Cell-Derived Factor 1.
TGF-β	Transforming Growth Factor β.
TME	Tumor Microenvironment.
TNBCs	Triple Negative Breast Cancers.
uPA	Urokinase Plasminogen Activator.
α-SMA	α-smooth muscle actin.

1 Introduction

This chapter provides the necessary background and context to understand the scope and significance of this report. Section 1.1 outlines key information about Triple Negative Breast Cancers (TNBCs), while Section 1.2 identifies the focus of the study and addresses gaps in existing research. Section 1.3 illustrates the thesis outline.

1.1. TNBCs: A High-Stakes Challenge in Oncology

According to data from the World Cancer Research Fund (2024), breast cancer is by far the most prevalent cancer in women [1]. If detected in an early, non-metastatic stage, the curability rate is approximately 80% [2]. However, if left untreated, tumors can metastasize, spread to other parts of the body and become life-threatening [3].

At the molecular level, breast cancer is a heterogeneous disease, comprising molecular subtypes that are Human Epidermal Growth Factor Receptor 2 (HER2)-positive, Estrogen Receptor (ER)-positive, Progesterone Receptor (PR)-positive, each characterized by the expression of specific biomarkers [2][4]. Breast cancers with inherited harmful mutations on the BRCA1[1] gene are more likely to be TNBCs [4]. TNBCs lack expression of ER, PR, and have little to no HER2 protein, classifying them as triple-negative.

As a result, TNBCs represents an aggressive breast cancer subtype with poor survival outcomes, largely due to the absence of targeted therapeutic options [3][4][5][6]. For example, endocrine therapies and HER2-targeted therapies are not effective [7]. Moreover, patients with advanced TNBCs typically develop resistance to chemotherapy (which is still the frontline treatment strategy for TNBCs) and radiation therapy [6] [8].

Groups most at risks for this subtype of breast cancer include younger women, African (American) and Hispanic women [9]. This heightened risk is driven by a combination of biological factors, like tumor heterogeneity, somatic mutations, and genetic predispositions; and non-biological factors like socioeconomic disadvantage, healthcare barriers, and comorbidities. These elements interact to increase TNBCs incidence, aggressiveness, and reduce survival outcomes in this population [10].

Given the aggressive nature and limited treatment options for TNBCs, especially in cases involving resistance to chemotherapy and radiotherapy, there is an urgent need to better understand the Tumor Microenvironment (TME) (Section 2.1) and its role in cancer progression. With its components like stromal cells, the Extracellular Matrix (ECM) (Subsection 2.1.3), and immune cells, it plays a critical role in tumor growth, invasion, and metastasis [11][12][13]. Therefore, cancer–microenvironment interactions are key drivers of resistance to chemo- and radiotherapy in TNBCs. Thus, understanding these mechanisms is essential for identifying new therapeutic targets and improving treatment strategies.

1.2. Research Objective

Among stromal cells, fibroblasts are the main producers of the ECM, which they, and macrophages, can actively remodel [13]. Together with cancer cells, these stromal components contribute to the

[1] BRCA genes produce proteins that help repair damaged DNA.

formation of a complex and disorganized architecture characteristic of tumor tissue. Research indicates that fibroblasts and macrophages are involved from the earliest stages of tumor development and metastasis [13]. They remain in close proximity to cancer cells and co-evolve with them during tumor progression. Notably, under normal physiological conditions, tissue homeostasis may suppress the expansion of transformed cells, and normal mammary fibroblasts have even been shown to inhibit tumor cell proliferation [14].

However, when the tissue microenvironment becomes dysregulated, this suppressive effect can be lost. For example, breast tissue stiffening, primarily due to elevated levels and increased cross-linking of type I collagen, emerges as a significant risk factor for breast cancer and is associated with higher mammographic density, a clinical marker used in cancer detection [15]. More broadly, the ECM undergoes complex molecular and structural alterations during tumor initiation and progression [16]. However, how these transformations from normal to malignant state affect the mechanical behavior of cells within the TME is still poorly characterized [16] [17][18][19].

In addition to tissue stiffening, ECM porosity, determined by collagen fiber density and organization, plays a crucial role in regulating cancer cell invasion [11]. Porosity influences not only the physical constraints experienced by migrating cells, but also the accessibility of signaling molecules within the TME. Smaller pore sizes can restrict the ability of cancer cells to move through the matrix, thereby acting as a physical barrier to invasion [11]. Conversely, larger pores can provide less resistance to migration, enabling more rapid and extensive cell dispersion. Furthermore, increased porosity can enhance the diffusion of soluble factors such as cytokines, growth factors, and proteases, which in turn may promote Epithelial-to-Mesenchymal Transition (EMT), angiogenesis, and matrix remodeling [11]. These are all processes that drive tumor progression. Thus, ECM porosity is a key biophysical property that directly influences the invasiveness and aggressiveness of cancer cells [11][20][21].

Because matrix stiffness is challenging to quantify consistently from the literature, this study solely focuses on the relationship between source-dependent type I collagen gel concentration and matrix pore size, and how these factors influence the time-dependent behavior of spheroids composed of either 4T1 mouse breast cancer cells, NIH3T3 mouse fibroblasts, or a combination of both. The working hypothesis is that mono 4T1 spheroids will exhibit the most rapid and aggressive growth, followed by heterospheroids. In contrast, NIH3T3-only spheroids are anticipated to show the slowest growth. Additionally, invasion is expected to be more pronounced in lower collagen concentrations, as the reduced matrix density may facilitate both cell proliferation and migration compared to the more restrictive environment of higher-density gels.
The following research question will be answered:

”How does collagen matrix porosity influence invasion of hetero-tumor spheroids?”

The following list of subquestions will provide aid in answering the research question:

1. How does varying collagen gel porosity affect heterospheroid growth and invasion?
2. How does varying collagen gel porosity affect mono cancer spheroid growth and invasion?
3. How does varying collagen gel porosity affect mono fibroblast spheroid growth and invasion?

1.3. Thesis Outline

The structure of this thesis is as follows: Chapter 2 presents the theoretical foundation of the study. Section 2.1 introduces the TME and its major components, followed by Section 2.2, which discusses the limitations of conventional research models. Section 2.3 covers the use of spheroids, and collagen-based hydrogels.

Chapter 3 presents the methodologies employed in this study. Section 3.1 details the cell culturing procedures, followed by Section 3.2 on spheroid seeding and Section 3.3 on collagen hydrogel preparation. Section 3.4 describes the imaging techniques used, and Section 3.5 explains the software tools applied for data analysis.

Chapter 4 presents the findings of this study. Section 4.1 examines the observed matrix porosity across the different gel conditions, while Section 4.2 discusses spheroid growth and morphology in both rat tail and bovine collagen gels.

Chapter 5 provides an in-depth analysis of the findings. Section 5.1 explores the correlation between pore size and the source-dependent variability. Section 5.2 discusses spheroid behavior in Low

Concentration Collagen Gels (LCCG) and High Concentration Collagen Gels (HCCG).

Chapter 6 highlights the key findings of this study and revisits the research question.

Chapter 7 concludes the thesis by outlining the key challenges encountered during the study and providing recommendations for future experiments to address these limitations and build upon the current findings.

2

Theoretical Background

This chapter reviews the scientific literature that forms the basis for the research in this thesis. It begins by discussing the TME (Section 2.1) and the limitations of conventional research models (Section 2.2) to establish the scientific context. It then introduces key experimental components; spheroids and collagen-based hydrogels (Section 2.3).

2.1. The Tumor Microenvironment

The TME is a complex system. In addition to cancer cells, the TME comprises of stromal cells like immune cells, adipocytes, blood vessels, endothelial cells, and particularly fibroblasts (Figure 2.1), which produce the ECM [22] [23] [13] [24]. Each of these cell types contributes distinct molecular features that drive tumor heterogeneity [22] [23] [25]. Thus, the TME actively promotes cancer progression through reciprocal interactions with cancer cells, supporting survival, (local) invasion, and metastasis [23]. Conditions like hypoxia, low nutrient availability, and acidity are common in the TME, triggering processes such as angiogenesis to supply the tumor with oxygen and nutrients and to support metabolic waste clearance [22]. Additionally, the immune cells in the TME and can exhibit either pro-tumorigenic or anti-tumorigenic effects, further influencing tumor development [23].

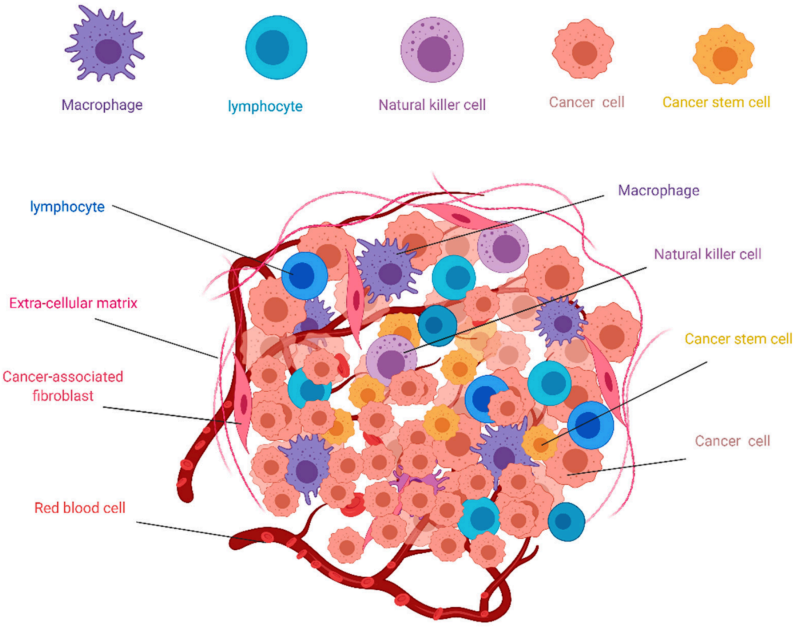

Figure 2.1: Representation of in vivo TME, emphasizing the heterogeneity of the different cells like lymphocytes, macrophages, and CAFs, which drives cancer progression and impacts therapeutic effectiveness. Image taken from [22].

2.1.1. Cancer cells

Cancer cells are cells that have undergone genetic changes and therefore no longer contribute to normal tissue architecture. Instead, they proliferate uncontrollably, are resistant to cell death, can evade the immune system, and can infiltrate surrounding tissue [26][27]. Many signaling and transcriptional mechanisms are shared between healthy and cancerous cells, but it is the specific combination of gene expression patterns that defines their identity within a particular tissue [27].

While molecular biology often models cancer cells as uniform populations using established cell lines, clinical observations reveal that tumors are highly heterogeneous in both composition and behavior [26]. This heterogeneity is shaped by dynamic interactions between cancer cells and their surrounding TME. These interactions play critical roles in promoting tumor progression, immune evasion, and therapeutic resistance [26].

To accurately understand cancer, it is essential to study cancer cells within the context of their native microenvironment, as tumorigenesis often arises from disruptions in these baseline physiological processes [27]. This integrated approach bridges the gap between in vitro models and clinical outcomes, providing deeper insight into tumor complexity and improving therapeutic strategies [26].

2.1.2. Fibroblasts

Fibroblasts are key stromal cells involved in maintaining tissue architecture and regulating ECM production. Fibroblasts emerge early during tumorigenesis and continuously co-evolve with cancer cells [13]. Within the TME, fibroblasts play a dynamic and multifaceted role. They influence tumor cell proliferation, invasiveness, and even contribute to therapy resistance [13].

Two main subtypes of fibroblasts exist in the TME: Normal-Associated-Fibroblasts (NAFs) and Cancer-Associated-Fibroblasts (CAFs). Fibroblasts from invasive mammary carcinomas (CAFs) differ biologically from normal fibroblasts (NAFs) [14][13]. While both can suppress early breast epithelial cell growth, NAFs are more effective. This suggests that fibroblasts progressively lose their tumor-suppressive capacity during breast cancer development [28].

Several mechanisms have been proposed for turning NAFs into CAFs [14][29][30].. The key distinction between these two fibroblast types is that CAFs contain a higher proportion of Transforming Growth Factor β (TGF-β) and myofibroblasts, activated fibroblasts characterized by elevated α-smooth muscle actin (α-SMA) expression [14][30]. These cells, typically involved in wound healing, exhibit enhanced contractility, promote angiogenesis, and stimulate epithelial growth through ECM production and cytokine secretion [14][30].

CAFs actively promote tumor vascularization and progression by secreting high levels of Stromal Cell-Derived Factor 1 (SDF-1). SDF-1 fosters tumor progression by recruiting endothelial progenitor cells, which enhance tumor angiogenesis, and activating CXC Chemokine Receptor-4 (CXCR4) (a receptor involved in stem cell migration) signaling in breast cancer cells [31][14]. They also release more peptide growth factors like Insulin-like Growth Factor II (IGF II), enhancing cell cycle progression and inhibiting apoptosis [28]. Notably, these tumor-promoting features persist in CAFs even without continued interaction with cancer cells [14]. This persistence suggests that CAFs undergo stable, long-term phenotypic changes, allowing them to maintain a pro-tumorigenic state independent of cancer cell signals [14].

Fibroblasts are key players in tumor progression and therapy resistance. While CAFs promote cancer development, even NAFs can support tumor survival under certain conditions, such as by protecting cancer cells from chemotherapy in 3D co-cultures [24]. Beyond signaling, fibroblasts also remodel the TME by producing and restructuring the ECM, a major driver of cancer progression [13].

2.1.3. The Extracellular Matrix

The ECM consists of proteins, glycoproteins, proteoglycans, and polysaccharides [32][33][34]. The filamentous architecture of the ECM, consisting primarily of collagen, fibrin, and fibronectin, provides structural support and shapes cancer cell adhesion and signaling. Within the tumor microenvironment (TME), multiple collagen types (I, II, III, V, VI, IX, X, XI) are upregulated [35]. Among these, collagen type I is the most abundant in mammalian tissues and its overexpression correlates with aggressive breast cancer traits, such as enhanced proliferation and resistance to apoptosis [35][36].

Cancer and stromal cells actively remodel the ECM, a process driven by CAFs activation, collagen crosslinking, and ECM protein accumulation (Figure 2.2) [37][38][21][30]. In 3D environments, this remodeling enables cell shape changes, spreading, and migration. It is especially crucial at the tumor

boundary, where the Basement Membrane (BM) acts as a barrier to nearby vessels [37][39]. This barrier is broken down by ECM-degrading enzymes, Matrix Metalloproteinases (MMPs). MMP-2 and MMP-9, highly expressed in aggressive breast cancers, are linked to poor prognosis [37][40][30]. In addition to degrading ECM, MMPs regulate adhesion, proliferation, and apoptosis, supporting tumor growth, angiogenesis, and metastasis [41].

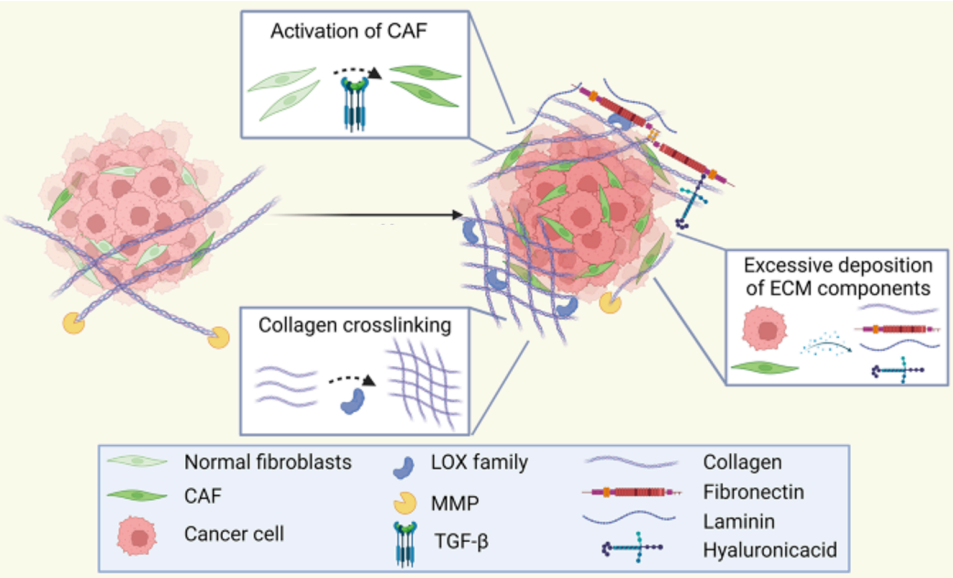

Figure 2.2: ECM remodeling is primarily driven by the activation of CAFs, enhanced collagen crosslinking, and the buildup of ECM proteins. Image taken from [30]

Key ECM properties like stiffness, pore size, composition, and organization critically affect tumor cell migration, proliferation, and treatment response [32][34]. Among these, pore size has emerged as a particularly important factor: tumor cell migration is more strongly influenced by ECM porosity than by stiffness, viscoelastic properties, or interstitial flow velocity [34][21][32]. Increasing ECM permeability (pore size), due to low collagen concentration, in turn increases tumor invasion and migration. Moreover, van der Net et al. (2024) identified matrix porosity as a significant factor influencing the timing of invasion onset [11]. Additionally, ECM fiber alignment and resistance to degradation influence tumor progression [34][21][11][16][38].

Increased ECM density, driven by collagen accumulation and crosslinking, reduces pore size and creates a confined, migration-restrictive environment. When pores shrink below cell size (<10 µm), cells face physical barriers that require deformation and matrix degradation to migrate [11][20][16][42]. Instead of tumor confinement, increased ECM density can therefore promote tumor spheroid invasion by inducing an “unjamming transition,” where the cell cluster becomes more fluid-like and motile (soft) [34]][11]. This increased flexibility allows the cells to squeeze through confined spaces and dense tissue architectures more effectively [16][33]. Thus facilitating invasion and enabling entry into the bloodstream or narrow capillaries, key steps in the metastatic cascade (Figure 2.3) [16].

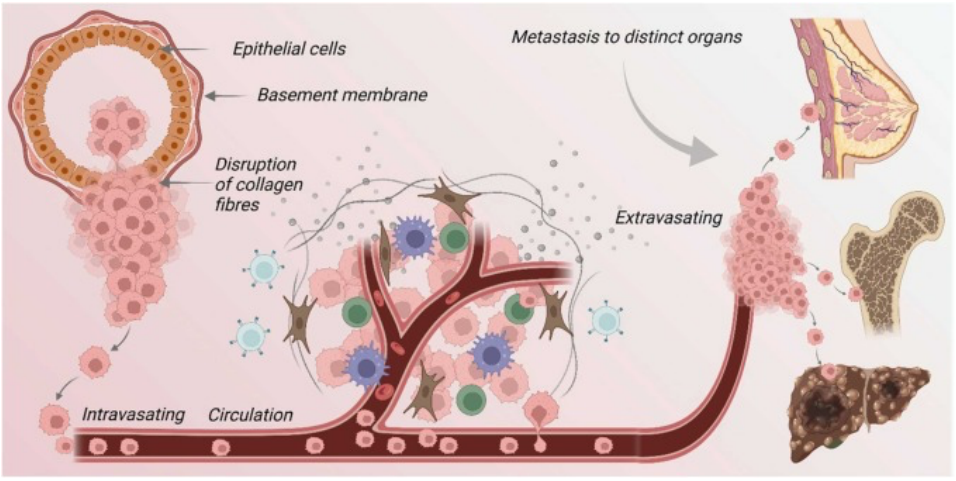

Figure 2.3: Basement membrane proteins influence cancer cell migration and metastasis. Cancer cells detach from the primary tumor, invade surrounding tissue by breaking through the BM, and enter the bloodstream. They travel through blood vessels, survive in circulation, and can settle in distant organs, where they may form secondary tumors after proliferation and blood vessel growth. Image taken from [39]

2.2. Limitations of Traditional Research Models

Cell–cell and cell–matrix interactions in the TME critically influence therapy response, making it an important therapeutic target. However, replicating the complexity of the TME in preclinical research remains a challenge [18][43].

While 2D cell culture systems are widely used in life sciences, they fail to capture critical aspects of the TME, such as cellular morphology, differentiation, and interactions with both neighboring cells and the ECM [18] [44][19][45][46]. In 2D cultures, cells are typically grown on rigid surfaces, such as polystyrene plates, where they are uniformly exposed to oxygen and nutrients, and cell morphology is unnatural (flat). This environment contrasts with the TME, where oxygen and nutrient distribution is uneven and cell populations continuously evolve [19]. Additionally, the limited number of neighboring cells in 2D cultures reduces opportunities for intercellular communication and impacts gene expression profiles [44][46][19]. Therefore, 2D cultures lack in vivo complexities, which can allow drugs to diffuse freely and interact directly with cells, leading to overestimation of a drug's efficacy [46]. Many anti-cancer drugs that show efficacy in 2D cultures ultimately fail in vivo, as breast tumors do not behave like flat monolayers. To more accurately study breast cancer and assess treatment responses, co-culture models that better replicate the complex TME are essential [24].

Animal models, like xenografts, where tissues or cells from one species are implanted into another, offer a more accurate recreation of the in vivo TME. However, they face notable limitations, including interspecies physiological differences, limited tumor heterogeneity, and lower mutation rates compared to human tumors [18]. Additionally, these models are costly, time-consuming, and subject to stringent regulatory and legal constraints [18].

Although it is unlikely that animal experiments can be entirely eliminated in the near future, their use can potentially be minimized and restricted primarily to the final stages of research. To bridge the gap between traditional 2D cell cultures and xenografts, 3D in vitro tumor models offer a means to more accurately simulate in vivo conditions, ex vivo [44][46][45].

2.3. 3D Cultures

The move toward 3D cultures stems from the need for more physiologically relevant models [44][46][45]. These 3D systems are expected to advance drug screening and reduce animal testing, particularly for toxicity studies [47].

3D cell culture models can be divided into scaffold based and scaffold-free cultures [46] [48]. Scaffold-based 3D cultures enable cells to anchor to 3D structures from natural or synthetic materials that simulate the ECM, such as collagen, chitosan, or polycaprolactone [46][44]. Scaffold-free 3D cultures rely on proteins secreted by the cells themselves during the formation process of a 3D structure, such as spheroids [46][19][18] [49].

2.3.1. Spheroids

Spheroids are scaffold-free 3D cell clusters, typically formed from cancer cells, that better replicate natural cell behavior, making them valuable for drug testing [46][19][18][49]. Spheroids can incorporate multiple cell types, like cancer and stromal cells, and in defined ratios, to model the cellular heterogeneity of tumors [46]. Structurally, they develop distinct zones: a proliferative, oxygen-rich outer layer; a quiescent middle zone; and a necrotic core (for diameters >250 µm) (Figure 2.4), which mimic the gradients found in poorly vascularized tumors [19][46][44][11]. Inner regions are hypoxic and nutrient-deprived, forcing cells to rely on the Warburg effect, while lactate buildup lowers pH in the necrotic core [46].
There are three stages to spheroid growth kinetics, which are also observed in in vivo solid tumors [46]:

- The early growth phase: during this phase exponential cellular growth is observed
- The dormant phase: during this phase cellular growth is sustained at a steady rate
- The vascular growth stage: during this phase ECM remodeling and secretion of angiogenic factors induce the formation of new vessels

.

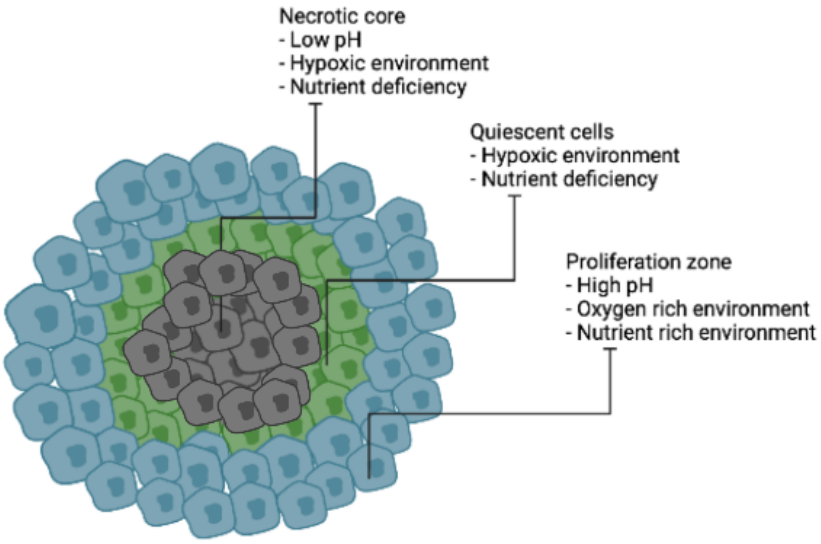

Figure 2.4: Internal spheroid structure, composed of a necrotic core, quiescent cells, and a proliferation zone. [Created with BioRender.com] Image taken from [50]

Multicellular spheroids (MCS) form through intrinsic self-assembly of cells suspended in biological fluids. This process relies on complex interactions involving both homotypic and heterotypic binding of cell adhesion molecules, ECM proteins, and integrins [51]. While the exact mechanism remains unclear, two main theories explain spheroid formation [51]:

- ECM proteins first bind to integrins, initiating loose aggregation. As cadherins are expressed, stronger cadherin-mediated adhesion compacts the spheroid.
- Alternatively, cadherin-mediated binding occurs first, forming initial aggregates. Cells then reorganize based on cadherin and integrin expression levels.

The close cell–cell proximity in spheroids promotes physical interactions and activates in vivo–like signaling pathways [46][52][42]. Because unlike 2D cultures, these 3D models exhibit distinct gene expression patterns. For instance, melanoma spheroids activate tumor-associated genes that remain inactive in 2D monolayers [47]. Ham et al. (2016) further showed that spheroids replicate key tumor features, such as oxygen and nutrient gradients that induce hypoxia [42]. This microenvironment supports cancer cell survival, promotes Cancer Stem Cells (CSC) traits, and contributes to therapy resistance and recurrence [42]. Furthermore, fibroblasts in 3D collagen adopt different morphologies and adhesion patterns than on flat substrates. Their migration, ranging from mesenchymal to amoeboid, is shaped by ECM confinement, not just integrin adhesion [47].

Techniques for 3D Spheroid Formation

Several methods have been devised to create MCS (Figure 2.5). These can be subcategorized into scaffold-based and scaffold-free methods. Advantages and disadvantages of the techniques are illustrated in Table 2.1.

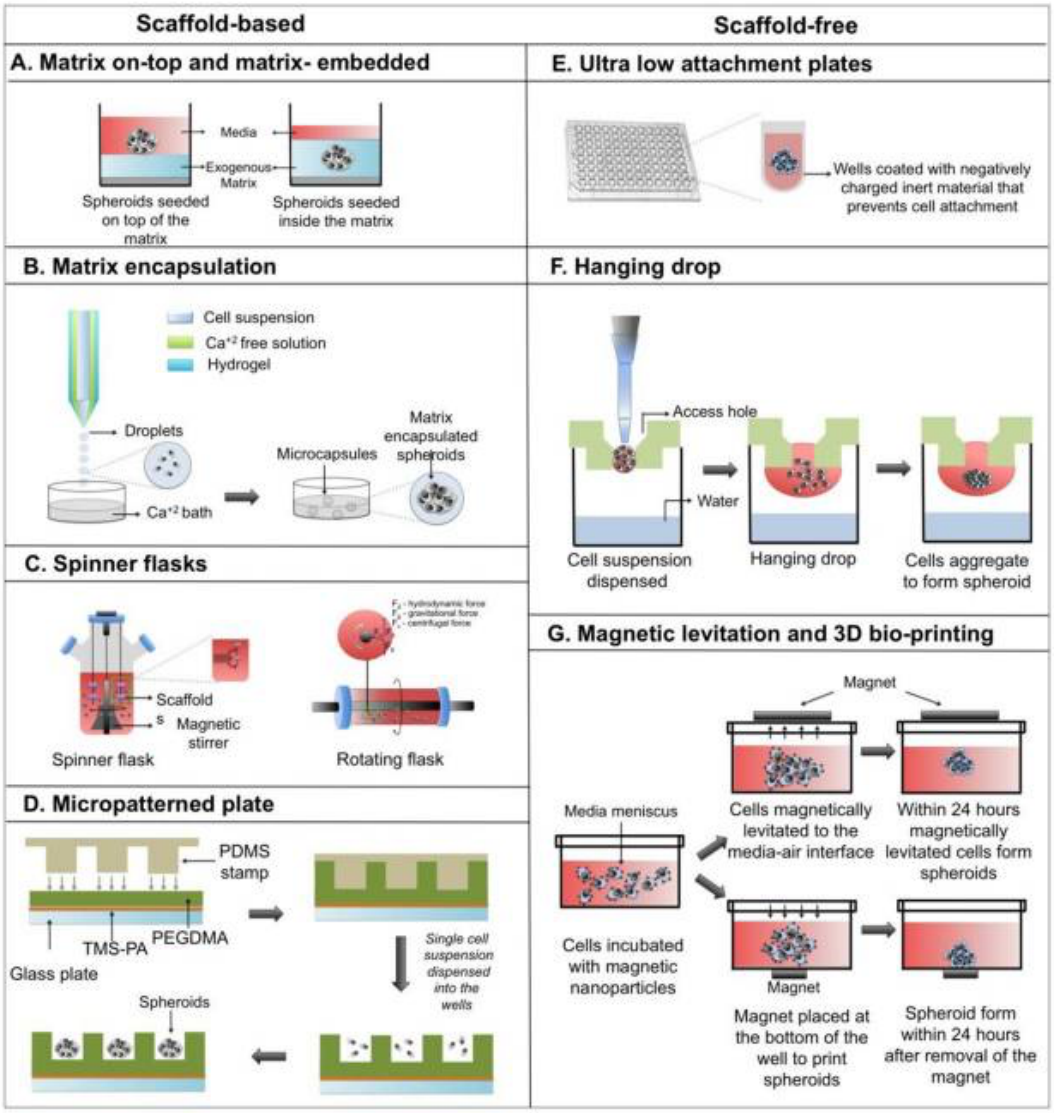

Figure 2.5: Different scaffold-based and scaffold-free techniques for spheroid formation. Advantages and disadvantages of each technique can be seen in Table 2.1. Scaffold-based techniques include A) Matrix on-top and matrix-embedded, B) Matrix encapsulation, C) Spinner Flasks, D) Micropatterned plates. Scaffold-free techniques include E) Ultra low attachment plates, F) Hanging drop, G) Magnetic levitation and 3D bioprinting. Image taken from [53]

Table 2.1: Advantages and disadvantages of various spheroid formation methods [53]

Matrix on-top and matrix-embedded	
Advantages	+ When using self-assembling protein-based hydrogels, cells can be retrieved after culture
Disadvantages	- Hydrogels necessitate specialized handling procedures - Often produce heterogeneous spheroids, requiring sorting prior to downstream analysis - Staining and imaging spheroids embedded within matrices present significant technical challenges
Matrix encapsulation (microfluidic device)	
Advantages	+ Uniform spheroids, eliminating the need for pre-assay sorting
Disadvantages	- Growth rate may be reduced due to physical confinement - Confinement can also lead to a higher incidence of necrotic regions - Thin matrix shells risk rupture under pressure
Micropatterned plates	
Advantages	+ Spheroids are relatively easy to image + Cells or spheroids can be retrieved after culture + Contains ECM components
Disadvantages	- Requires well surface treatment to prevent cell adhesion - Results in spheroids with inconsistent sizes - Excessive numbers of spheroids per well can interfere with assay accuracy
Hanging drop	
Advantages	+ Enables generation of many spheroids within a compact area + Minimizes reagent usage + Allows for recovery of spheroids after culture
Disadvantages	- Process can be labor-intensive - For extended culture periods, spheroids must be moved from the hanging drop setup to a plate with greater media capacity - Spheroids are transferred to a different plate for final analysis
Ultra low attachment plates	
Advantages	+ Cost-effective and user-friendly + High number of spheroids within a small footprint (such as 96-well plates) + Allows end-point analysis directly in the culture plate + Facilitates easy recovery of spheroids after culture + Compatible with multiplexing for imaging and other biochemical assays
Disadvantages	- Results in spheroids with variable sizes - May contain a mix of both attached cells and free-floating spheroids
Magnetic levitation and Magnetic Bio-printing	
Advantages	+ End-point analysis can be performed directly on the culture plate + Compatible with multiplexing for imaging and various biochemical assays
Disadvantages	- Produces a limited number of spheroids - Requires pre-treatment of cells with magnetic beads - Magnetic beads are costly - High concentrations of beads may have toxic effects on cells

As shown in Table 2.1, Ultra Low Attachment (ULA) plates offer significant advantages and are among the most user-friendly scaffold-free methods for generating MCS. In this study, spheroids were formed using the ULA plate method. However, as a scaffold-free technique, ULA plates lack mechanical support, structural (shape) control, and consistency, features more reliably provided by scaffold-based 3D culture systems (Figure 2.5) [48]. To overcome these limitations, the ULA-formed spheroids were embedded in a collagen hydrogel, thereby converting the system into a scaffold-based 3D culture platform. This hybrid approach offers improved physiological relevance and experimental versatility for studying cancer biology and therapy responses [51].

2.3.2. Collagen-Based Hydrogel

Aggressive cancer cells often do not thrive in standard 2D in vitro settings because they lack a supportive microenvironment [32]. The complexity of the in vivo ECM has driven the development of hydrogel-based 3D culture systems that better replicate the native microenvironment for in vitro MCS growth [32]. Composed of physically or chemically cross-linked polymer networks, hydrogels provide a biomimetic scaffold that supports cell growth and tissue-like organization. Consequently, natural and synthetic hydrogels offer versatile platforms for MCS formation, long-term maintenance, cancer research, and high-throughput drug screening [32].

Protein-based hydrogels, like collagen, Matrigel, or fibrin, contain natural binding sites that allow cells to attach, spread, and interact with the matrix (cell adhesion properties). This closely mimics the native ECM [32]. As discussed in Subsection 2.1.3, collagen type I is the most abundant fibrous protein in mammalian ECM and plays a crucial role in tumor progression by supporting cell adhesion and migration. Consequently, 3D collagen gels are widely used to mimic the ECM [32][36][44]. Collagen hydrogels are highly tunable. Their network structure can be precisely controlled by adjusting collagen concentration and gelation conditions like temperature and pH, allowing close replication of native ECM properties [32][34]. Specifically, type I collagen hydrogels have successfully supported MCS formation in various cancers, including osteosarcoma, breast, and colorectal tumors [32]. These 3D collagen scaffolds promote multilayered growth and strengthen cell–cell and cell–ECM interactions. Thus creating a hypoxic microenvironment that drives apoptosis resistance and upregulates pro-angiogenic factors and MMPs, mimicking key features of in vivo tumor progression [45].

ECM stiffness plays a key role in regulating tumor cell migration within 3D collagen matrices [32][12]. Yuan et al. (2019) showed that softer matrices from lower collagen concentrations promote migration in invasive breast cancer spheroids [12]. However, the relationship between collagen concentration and stiffness varies widely across studies. Yang et al. (2009) reported a moderate scaling law for type I rat tail collagen [54], whereas Blazquez et al. (2024) and Cameron et al. (2023) found much higher stiffness values for similar concentrations of bovine collagen [38][20]. These inconsistencies underscore a lack of standardization in measuring and reporting collagen stiffness.

Despite the influence of stiffness, matrix porosity is the dominant driver of cancer invasion and migration (Subsection 2.1.3). There is a general consensus in literature that smaller pore sizes are associated with higher fiber densities, and thus higher collagen concentrations [11] [20] [21] [55]. These small pore sizes can restrict cellular movement by making it more difficult for cells to physically squeeze through the matrix [11] [20] [21] [55]. In contrast, larger pores facilitate easier cell migration by providing less physical obstruction. For example, Chen et al. (2012) demonstrated using MCF-7 breast cancer cells that porous 3D collagen scaffolds offer sufficient space for cell proliferation, adhesion, and spreading [45]. Importantly, such porous environments also encourage heterogeneity in cell morphology, reflecting more closely the diversity observed within tumors in vivo [45]. Thus, matrix porosity not only controls the physical capacity for migration but also influences cellular behavior and phenotypic variability critical for cancer progression.

Building on these insights, this study generates spheroids using ULA plates, then embeds them in tunable 3D collagen hydrogels that mimic native ECM mechanics and architecture. By controlling collagen concentration and gelation conditions, it examines how matrix porosity affects the growth, morphology, and invasive behavior of heterogeneous breast cancer spheroids.

3

Methods

This chapter outlines the methods utilized during this study. For a complete overview of the (bio)chemicals, see Appendix A. An overview of the experimental research methodology is illustrated in Figure 3.1.

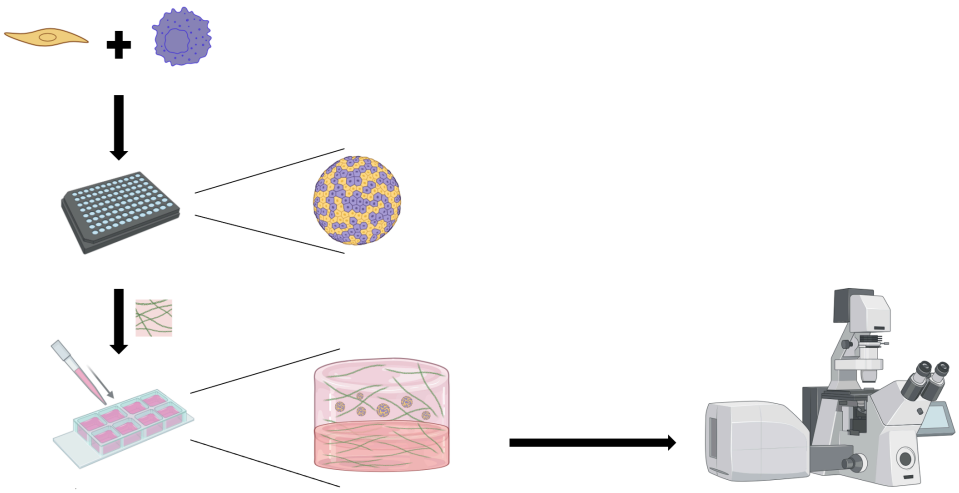

Figure 3.1: Experimental research methodology: Fibroblasts and cancer cells are combined in a ULA plate to form heterogeneous spheroids, which are then embedded in a collagen-based hydrogel via a bed protocol. Time-lapse imaging is conducted using confocal microscopy. [Created with BioRender.com]

3.1. Cell Culturing

For this study, mouse 4T1 and mouse NIH3T3 cells were maintained in culture medium consisting of 89% 1x RPMI, 10% FBS, and 1% Anti-Anti, and 89% 1x DMEM, 10% FBS, and 1% Anti-Anti respectively). Cells were passaged approximatly three times per week. Briefly, cells were washed with 1x DPBS, followed by treatment with trypsin to detach the cells from the bottom of the flask. After centrifugation (Eppendorf Centrifuge 5804 R), cells were resuspended in 1 mL of medium. To achieve the desired mixing ratio, the required volume of cell suspension was calculated based on cell concentration ratio, resulting in a final medium-to-cell suspension ratio of 1 mL to *x* µL. After transferring to a new flask, the cells were incubated at 37°C / 5% CO_2.

3.2. Spheroid Seeding

Spheroid seeding was performed in a 96-well ULA round-bottom plate (Corning) to encourage cell–cell interactions and prevent adhesion to the plastic surface. Spheroids were seeded after cell culturing, using a cell counter (Bio-Rad TC20 Automated Cell Counter), to achieve the desired number of cells per well. Then, each well of the ULA plate was pre-filled with 100 µL of culture medium and centrifuged using an Eppendorf Centrifuge 5804 R to ensure even distribution of medium and eliminate trapped air

bubbles. Cells were seeded at a density of 375 cells per spheroid, and the plate was centrifuged again to achieve a homogeneous distribution across the microwells. An additional 100 µL of culture medium was gently layered on top. Spheroids were cultured at 37°C and 5% CO_2 for 2 days prior to embedding in collagen gels. Spheroid diameter ranged from 110 to 180 µm.

3.3. Collagen Hydrogel

During this study, two protocols for collagen hydrogel were utilized (Subsection 3.3.1). Both protocols required all materials to be kept on ice throughout the experimental process, in order to prevent premature polymerization and maintain reagent stability [56] [11].

By utilizing a protocol adapted from van der Net et al. (2024), 100 µL of a collagen layer without cells was added to an 8-wells chamber (Sarstedt or Ibidi) [11]. The chamber slide was then incubated at 37°C and 5% CO_2 to allow for polymerization. After 45 minutes, the chamber slide was transferred onto tissue paper in the biosafety cabinet to minimize temperature fluctuations. This was done because cooling after polymerization can destabilize the collagen at the glass interface and cause matrix detachment [57]. A second 200 µL gel layer containing spheroids (see Appendix B for spheroid transfer details), was added on top. The chamber slide was then incubated at 37°C with 5% CO_2 for 45 minutes to allow this layer to polymerize.

3.3.1. Collagen Gel Protocols

To test how different collagen gelation conditions affect the final gel properties, two distinct protocols were evaluated (Table 3.1, Table 3.2, Table 3.3). These protocols varied in either the source of collagen (rat tail at 11.23 mg/mL or bovine at 10 mg/mL) or the buffer composition (for buffer recipes, see Appendix A.3). Protocol I uses either rat tail (11.23 mg/mL) (Table 3.1) or bovine (10 mg/mL) (Table 3.2) collagen with 10x DMEM and 10x RB as buffers. Protocol II uses rat tail collagen (Table 3.3) with 10x PBS as buffer. All protocols include NaOH for pH adjustment to 7.4.

The final gel formulations were assembled following the order of reagents listed in Table 3.1 and Table 3.2. The tables below summarize the volumes used for each component of the different protocols, detailing preparations for different collagen concentrations and sources. After all components had been added, air bubbles were removed through brief centrifugation (Thermo Scientific MicroCL 21R centrifuge). The pH of the gel was measured using pH strips. When a pH of 7.4 was reached, the gel was incubated at 37°C with 5% CO_2 to allow polymerization.

Table 3.1: Collagen protocol I, with rat tail collagen, based on Doyle et al. x denotes a variable quantity, with NaOH purely necessary for pH control (7.4). [56]

	Rat tail (11.23 mg/mL)		
		1.5 mg/mL	*4.0 mg/mL*
Step	**Chemical**	**Volume (µL)**	**Volume (µL)**
1	Collagen	40.1	107
2	10x DMEM	30	30
3	10x RB	30	30
4	NaOH	x	x
5	MilliQ	199.9	83
6	Cells	50	50
Total Volume		300 µL	300 µL

Table 3.2: Protocol I, with bovine collagen, x denotes a variable quantity, with NaOH purely necessary for pH control (7.4) [56]

	Bovine (10 mg/mL)		
		2.4 mg/mL	*3.3 mg/mL*
Step	**Chemical**	**Volume (µL)**	**Volume (µL)**
1	Collagen	72	99
2	10x DMEM	30	30
3	10x RB	30	30
4	NaOH	x	x
5	MilliQ	118	91
6	Cells	50	50
Total Volume		300 µL	300 µL

Table 3.3: Collagen protocol II, with rat tail collagen, based on van der Net et al. x denotes a variable quantity, with NaOH purely necessary for pH control (7.4) [11]

	Rat tail (11.23 mg/mL)		
		1.5 mg/mL	*4.0 mg/mL*
Step	**Chemical**	**Volume (µL)**	**Volume (µL)**
1	Collagen	40.1	107
2	10x PBS	37.5	37.5
3	NaOH	x	x
4	MilliQ	172.4	105.5
5	Cells	50	50
Total Volume		300 µL	300 µL

3.4. Imaging

To analyze spheroid architecture and behavior within the collagen network, imaging was performed using fluorescence microscopy (ZEISS LSM 980). Reflected light from the collagen matrix and fluorescence from the spheroids were captured simultaneously in time-lapse mode, where images were taken every hour for 24 hours. A 10x Air objective lens was used, with a resolution of 0.414 µm/pixel.

The experiment was conducted at predefined positions, capturing 10 z-slices across a total depth of 200 µm over a 24-hour period. Z-slices are sequential optical sections captured along the vertical (z) axis, generating the full structure in a 2D reconstruction of the sample. dTomato cytoplasmic labeled 4T1 cells (ex. 554 nm, em. 581 nm) were visualized with a 543 nm laser. mCerulean3 cytoplasmic labeled NIH3T3 cells (ex. 353 nm, em. 465 nm) were visualized with a 405 nm laser. To visualize the collagen fibers through reflection, a 488 nm laser was used. After 24 hours, (reflection) images of the collagen were captured using a 40x water immersion objective lens, resolution 0.1036 µm/pixel, for further analysis.

3.5. Image Analysis

Quantification of spheroid migration and ECM remodeling requires specialized image analysis tools. This subsection provides an overview of the software used for data processing and quantification.

3.5.1. Spheroid Morphology

Fiji/ImageJ, an open-source image analysis tool [58], was used to compile z-stacks from time-lapse images at each position, segment spheroids, and quantify morphological features. Brightness and thresholding parameters were adjusted as needed to ensure accurate analysis.

CellProfiler is an open-source tool for high-throughput biological image analysis [59]. In this study, it was used to extract quantitative morphological features from microscopy images to enable downstream analysis.

Morphological changes were quantified using growth and circularity (Eq. 1) (and aspect ratio (Eq. 2), Appendix G) measurements. To assess growth dynamics, the average spheroid radius was normalized to its initial value and tracked over time. Invasion onset was defined as the time point at which the normalized radius reached 1.1, indicating a 10% increase in spheroid size [11]. Circularity measures how close the spheroid is to a perfect circle, with values ranging from 1 (perfect circle) to 0 (irregular shape with protrusions). Aspect ratio describes the elongation of the spheroid, with a value of 1 indicating a circular shape and values greater than 1 indicating elongation or stretching in one direction. The effect of the spheroids on the collagen matrix can be found in Appendix D.

$$\text{Circularity} = \frac{4\pi \times \text{Area}}{\text{Perimeter}^2} \tag{1}$$

A circularity of 1 corresponds to a perfect circle.

$$\text{Aspect Ratio} = \frac{\text{Major Axis Length}}{\text{Minor Axis Length}} \tag{2}$$

Higher aspect ratios indicate more elongated spheroids.

3.5.2. Collagen Porosity

A Python script developed by Iain Muntz was modified during this study, and used to quantify the porosity of collagen hydrogels using the bubble method (Appendix E) [11]. In this method, bubbles are introduced into the interstitial spaces between collagen fibers, where the matrix lacks dense structural support. The script then quantitatively analyzes bubble diameters, which represent the void sizes within the gel, and generates a probability density function of their size distribution. This approach allows for precise and automated measurement of the hydrogel's porosity.

This method introduces bubbles into the interstitial spaces between collagen fibers. Confocal images are denoised, binarized, and converted into Euclidean distance maps to identify local maxima representing the largest pores. The script then analyzes these void diameters and generates a probability density function of their size distribution, enabling precise, automated porosity measurement.

4

Results

This section presents the key findings of the study, highlighting the main observations and trends across different experimental conditions. To study how collagen porosity affects invasion and growth of heterogeneous breast cancer–fibroblast spheroids, different collagen concentrations and sources were used. Experiments were conducted with three spheroid conditions: mono-cultured 4T1 spheroids, mono-cultured NIH3T3 spheroids, and 1:1 heterospheroids. To ensure consistency, both rat tail and bovine collagen gels were prepared using Protocol I (Chapter 3). Invasion and growth dynamics were assessed and quantified using metrics of area, perimeter, and circularity. For uniformity, protocol I (Chapter 3) was used to prepare both rat tail gels and bovine gels.

4.1. Collagen Matrix Porosity

The pore size of all collagen gels was analyzed to characterize the physical properties of the experimental ECM. Pore sizes in the collagen networks were quantified using a custom Python script based on the bubble method (Appendix E).

At 1.5 mg/mL rat tail collagen, the average pore size was 0.82 µm (Figure 4.1A). Increasing the (rat tail) collagen concentration to 4.0 mg/mL illustrated a large decrease in pore size, to 0.44 µm (Figure 4.1A). At 2.4 mg/mL bovine collagen, the average pore size was 0.98 µm (Figure 4.1B). Increasing the bovine collagen concentration resulted in a decrease in pore size, to 0.79 µm.

These results demonstrate that for both collagen sources, increasing the collagen concentration leads to a denser matrix with smaller pores. Notably, the rat tail collagen gels exhibited relatively small error bars, indicating consistent gelation and high reproducibility. In contrast, the bovine collagen gels exhibited greater variability, which may reflect batch-to-batch inconsistencies or increased sensitivity to the gelation process. This might be attributed to differences in fiber organization or polymerization kinetics.

The observed decrease in pore size with increasing collagen concentration, along with the differing degrees of structural uniformity, is expected to influence spheroid behavior. Denser matrices with smaller pores may restrict cell invasion, alter migration modes, and modulate mechanical signaling.

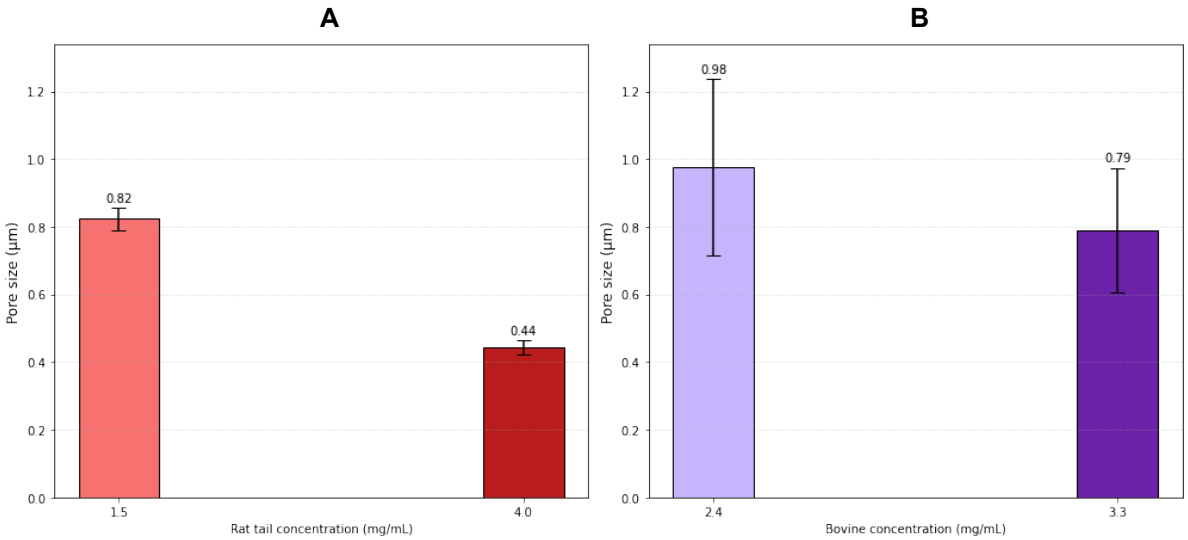

Figure 4.1: Pore sizes of different collagen concentration and sources. A) Pore sizes of 1.5 mg/mL and 4.0 mg/mL rat tail collagen. B) Pore sizes of 2.4 and 3.3 mg/mL bovine collagen.

4.2. Spheroid Growth and Morphology

Morphological changes were quantified by growth (normalized radius increase), circularity (1 = perfect circle, 0 = irregular), and aspect ratio (1 = circular, >1 = elongated; Appendix G). Invasion onset was defined as when normalized radius exceeded 1.1 (a 10% increase) [11], indicated by a dashed line.

4.2.1. Spheroid Growth and Morphology in Rat Tail Collagen Gels

In the 1.5 mg/mL collagen gel, all three spheroid types exhibited distinct invasion profiles and growth rates (Figure 4.2). Mono-cultured 4T1 spheroids exhibited rapid expansion, as seen by the early protrusions in Figure 4.2C. This is further supported by the prominent matrix remodeling, as indicated by the time-dependent change of fiber alignment (Figure D.1C). Local degradation was also observed, as indicated by the black voids near the spheroid at t = 24h (Figure D.1C). Invasion onset was characterized at t = 3h (Figure 4.4A). These mono 4T1 spheroids maintained a unified structure over time, but exhibited increasing protrusive extensions. (Figure 4.2C). By t = 24h, these spheroids displayed extensive spreading and irregular morphology, indicative of aggressive invasion (Figure 4.2C).

In contrast, mono NIH3T3 spheroids remained compact throughout the 24-hour period (Figure 4.2B). These spheroids exhibited only moderate collagen remodeling, as indicated by the slight increase of (fiber) fluorescence (Figure D.1B). Around t = 18h, individual fibroblasts began dispersing from the spheroid core(Figure 4.2B), yet without forming coordinated invasive structures. Therefore, they showed only minimal invasive activity starting at t = 18h (Figure 4.4,A). This indicates limited migratory potential in this context when fibroblasts are cultured independently.

Heterospheroids exhibited a combination of moderate expansion and partial invasion, displaying more spreading than fibroblasts alone but less extensive invasion than mono 4T1 spheroids. (Figure 4.2A). Interestingly, the heterospheroids exhibited the most extensive matrix degradation, evidenced by a prominent black void at the spheroid site (Figure D.1A). Minimal structural remodeling was observed, as the collagen fibers were not distinctly visible (Figure D.1A). Invasion onset started at around t = 5h (Figure 4.4A), with visible protrusions (Figure 4.2A). By t = 24h, invasion was evident but less extensive than in the mono 4T1 condition.

In the 4.0 mg/mL collagen condition, all three spheroid types exhibited a stark change in behavior compared to the 1.5 mg/mL condition. Here the spheroids maintained a compact, circular morphology throughout the entire observation period, where cells remained confined within the spheroid boundary (Figure 4.3). While modest spheroid growth is indicated by the gradual increase in radii of mono 4T1 and heterospheroids (Figure 4.4B), no invasive behavior was observed, as there were no visible protrusions, nor outward cell migration (Figure 4.3C, A). In contrast to the 1.5 mg/mL condition, the mono 4T1 spheroids and heterospheroids in the 4.0 mg/mL gels only exhibited matrix degradation, as indicated by the black voids at the spheroid sites (Figure D.2C, A). No apparent remodeling was seen, as no fibers were observed (Figure D.2C, A). Mono NIH3T3 spheroids exhibited neither invasion nor growth, as no

significant increase in radius, or protrusions were observed (Figure 4.4B) (Figure 4.3B). No remodeling or degradation was observed here either (Figure D.2B). This dramatic reduction in invasive activity and matrix remodeling in all three spheroid types strongly suggests that the denser hydrogel matrix is suppressing spheroid growth.

Interestingly, there was a noticeable drop in the normalized radius of the heterospheroids in 4.0 mg/mL between t = 18 and t = 19h (Figure 4.4B), likely due to out-of-frame cell migration along the z-axis, as Figure 4.3A illustrates a loss in fluoresence signal. The cells appear to have moved beyond the imaging field in the z-direction, which artificially reduced the measured area and radius.

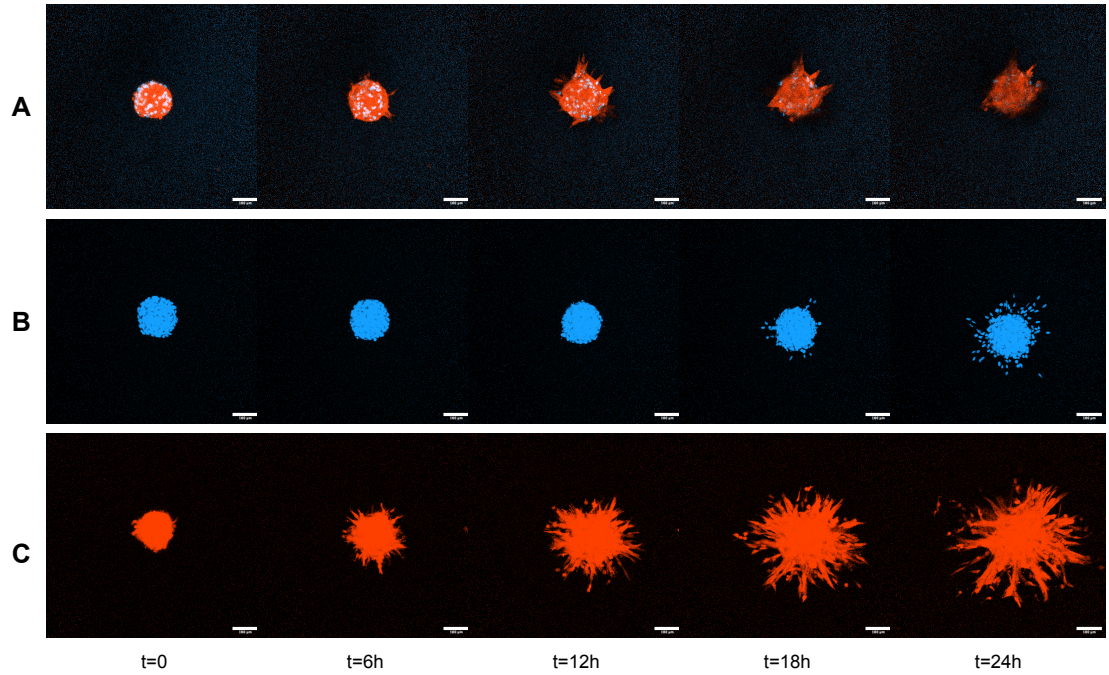

Figure 4.2: Temporal progression of spheroids in 1.5 mg/mL rat tail collagen gel. x-axis illustrates time in hours. A) Hetero-spheroids (1:1), showing the evolution from early compact structures to more irregular and invasive shapes. B) Mono NIH3T3 spheroids, which remain relatively compact, with some cellular dispersion over time. C) Mono 4T1 spheroids, displaying rapid expansion and pronounced invasive protrusions over time. Scale bars correspond to 100 µm.

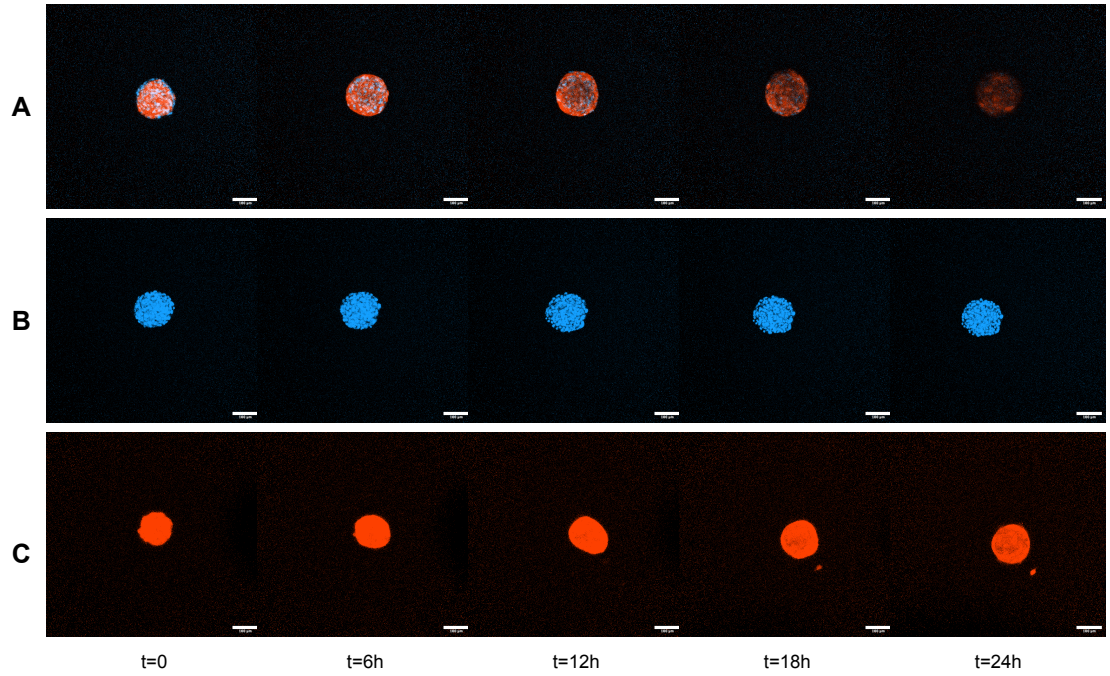

Figure 4.3: Temporal progression of spheroids in 4.0 mg/mL rat tail collagen gel. x-axis illustrates time in hours. A) Heterospheroids (1:1), which exhibit minimal morphological changes and no outward migration throughout the observation period. B) Mono NIH3T3 spheroids, which also remain tightly compact and show no signs of invasive behavior. C) Mono 4T1 spheroids, which also maintains a compact structure with limited expansion. Scale bar corresponds to 100 µm.

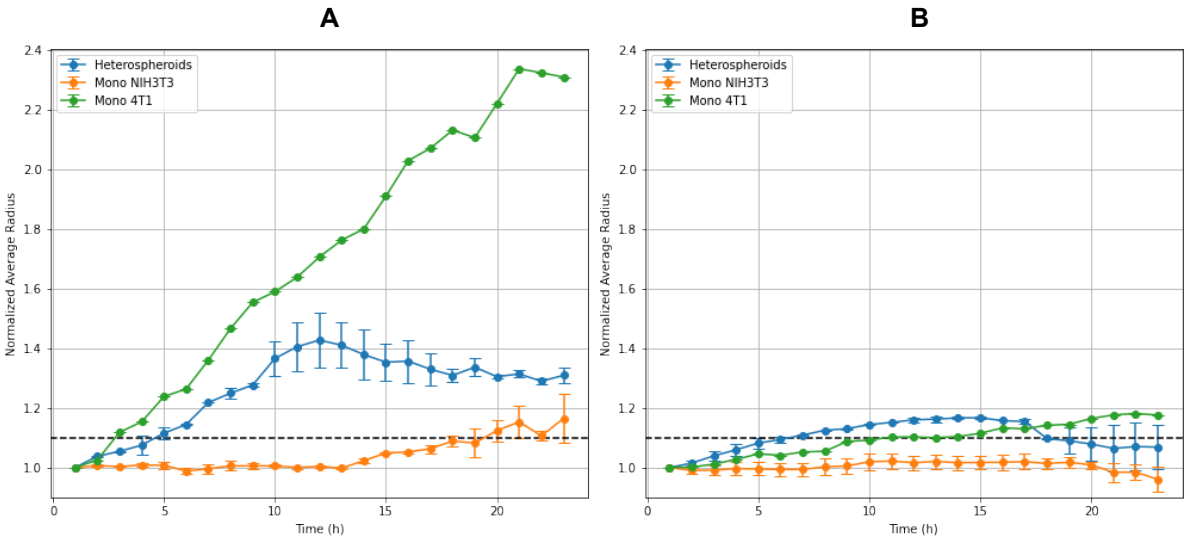

Figure 4.4: Increase in (normalized) radii over time. Invasion onset for each spheroid type is marked by the dashed line. A) 1.5 mg/mL condition. Mono 4T1 spheroids illustrate the most pronounced growth, with early invasion at t = 3h. Heterospheroids illustrated invasion onset at t = 5h. And finally, mono NIH3T3, illustrated slight invasion onset at t = 18h. B) 4.0 mg/mL condition. Mono 4T1 and heterospheroids illustrated a similar growth pattern, but no invasion was observed. Mono NIH3T3 spheroids did not illustrate growth or invasion.

Over time, a decrease in circularity is observed for all three spheroid types in the 1.5 mg/mL collagen gel (Figure 4.5). This observation is consistent with the invasive profiles demonstrated in Figure 4.2.

The decrease in circularity was most pronounced in the mono 4T1 spheroids (Figure 4.5C). Circularity sharply decreased from approximately 0.58 at t = 0 to 0.1 at t = 8h, after which it remained consistently low for the remainder of the experiment. (Figure, 4.5C). This aligns with the aggressive, irregular growth pattern seen in Figure 4.2C. Both mono NIH3T3 spheroids and heterospheroids also exhibited a gradual reduction in circularity, though to a lesser extent than mono 4T1 spheroids (Figure 4.5B and Figure 4.5A). Mono NIH3T3 spheroids exhibited a slower decline in circularity, decreasing

from 0.6 at t = 0 to 0.2 at t = 19h (Figure 4.5B), aligning with the celullar dispersion observed in Figure 4.2B. This suggests minimal invasive behavior, characterized more by individual cell dispersal than by coordinated outward growth. Heterospheroids showed a notable decrease in circularity from approximately 0.75 at t = 0 to 0.21 by t = 9h, after which the value remained relatively stable. This trend reflects a more restrained and cohesive invasion pattern, as observed in Figure 4.2A, likely influenced by interactions between the fibroblasts and 4T1 cells.

In contrast, in the 4.0 mg/mL collagen gel, the circularity of both mono NIH3T3 and mono 4T1 spheroids remains relatively stable over time, at 0.6 and 0.9 respectively (Figure 4.6B and Figure 4.6C). This stability suggests minimal morphological change in both spheroid types, aligning with the little to no invasive activity observed in Figure 4.3. This further indicated the restrictive effect of the denser matrix on spheroid behavior. However, the heterospheroids exhibited a noticeable drop in circularity at later time points, starting at 0.8 (t = 0) and ending at 0.7 (t = 24h) (Figure 4.6A). As previously noted, this deviation is likely due to cells having migrated out-of-frame, skewing the shape measurements.

Interestingly, the aspect ratio profiles are quite similar between the two gel concentrations, suggesting that matrix density had minimal influence on spheroid elongation. In both conditions, only the heterospheroids exhibited noticeable elongation (Figure G.1 and Figure G.2).

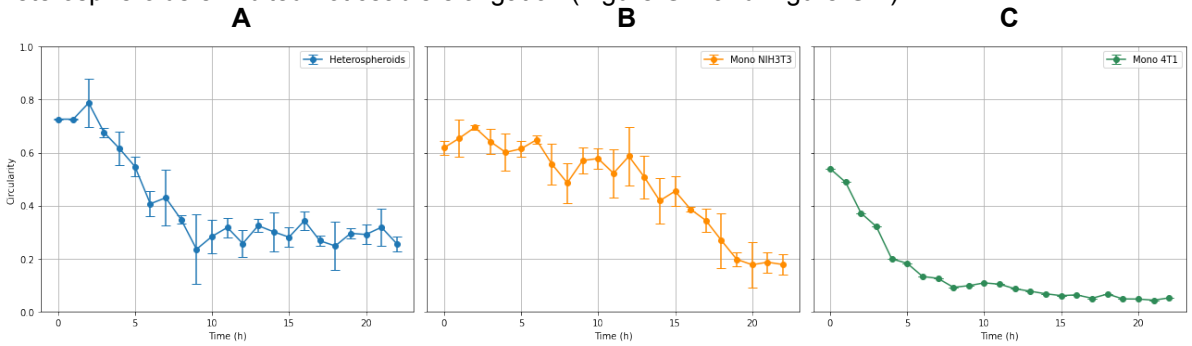

Figure 4.5: A decrease in circularity is observed for all three spheroid types in 1.5 mg/mL rat tail collagen

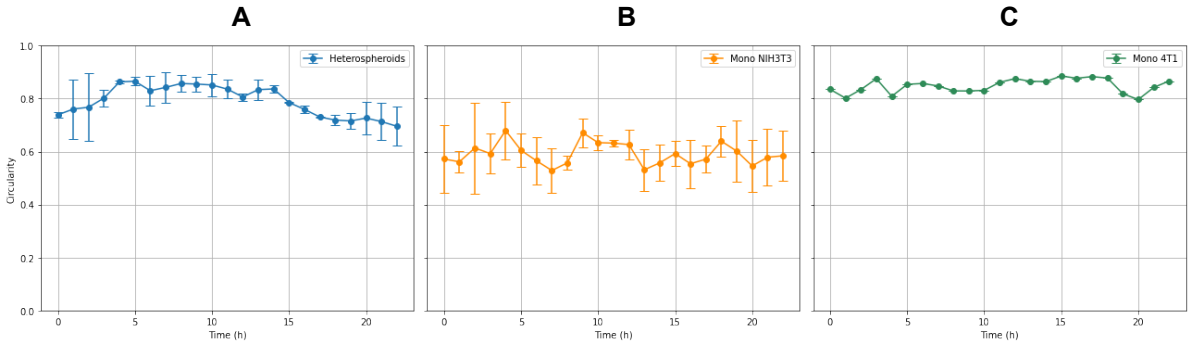

Figure 4.6: All three spheroid types illustrate relatively stable circularity in 4.0 mg/mL rat tail collagen. Heterospheroids show a slight decrease in circularity.

Another interesting observation was the rapid decline of the rat tail collagen quality. Thus resulting in a loss of structural integrity and allowing spheroids to migrate out of frame. A detailed account of the degradation process and its implications can be found in Appendix F.

4.2.2. Spheroid Growth and Morphology in Bovine Collagen Gels

In the 2.4 mg/mL (bovine) gel condition (Figure 4.7), all three spheroid types displayed behavior closely resembling that observed in the 1.5 mg/mL (rat tail) gel (Figure 4.2).

Mono 4T1 spheroids showed rapid expansion starting between t = 1h and t = 6h, while maintaining a cohesive structure throughout the experiment (Figure 4.7C). An increase in fluorescence indicated matrix remodeling, though the individual fibers were not readily discernible (Figure D.3C). Invasion onset occurred around t = 4h, as indicated by the normalized radius data (Figure 4.9A). By t = 24h, these spheroids had spread extensively and adopted irregular morphologies characteristic of aggressive invasion (Figure 4.7C).

Mono NIH3T3 spheroids remained mostly compact throughout the 24-hour period, and no significant growth was observed (Figure 4.7B). Consistent with this, they did not illustrate invasion (Figure 4.9A). Matrix degradation was not evident, and remodeling appeared minimal, indicated by subtle fluorescence changes, with individual fibers not clearly discernible (Figure D.3B).

Heterospheroids showed intermediate behavior, with moderate expansion and partial invasion. They exhibited more spreading than mono NIH3T3 spheroids, but less than mono 4T1 spheroids (Figure 4.7A) (Figure 4.9A). Contrary to the other two spheroid types, (only) matrix degradation was observed for the heterospheroids in this gel condition, as indicated by the black void at the spheroid site (Figure D.3A). Invasion onset occurred at t = 5h, as visible protrusions could be observed.

In contrast to the pronounced behavioral shift observed between the two rat tail collagen concentrations, the spheroid responses in the two bovine collagen conditions appeared largely similar. In the 3.3 mg/mL gel, again mono 4T1 spheroids exhibited invasive behavior early on, with visible protrusions forming between t = 1h and t = 6h (Figure 4.8C), and an invasion onset at approximately t = 3h, as indicated by the radius measurements (Figure 4.9B). Matrix remodeling was observed as well, as indicated by the increase in fluorescence, but no degradation (Figure D.4C).

Mono NIH3T3 spheroids remained predominantly compact, with limited cellular dispersion and growth becoming apparent only at t = 24h (Figure 4.9B) (Figure 4.9B). However, no coordinated invasive structures were observed, as well as no matrix degradation. However, minimal remodeling was observed (Figure D.4B).

Heterospheroids once again exhibited intermediate behavior, characterized by moderate expansion and partial invasion. They demonstrated greater spreading than mono NIH3T3 spheroids, but less extensive invasion than mono 4T1 spheroids (Figure 4.7A). Matrix degradation was observed, as evidenced by the black void at the spheroid site, with minimal remodeling (Figure D.4A). Invasion onset was observed around t = 4h (Figure 4.9B).

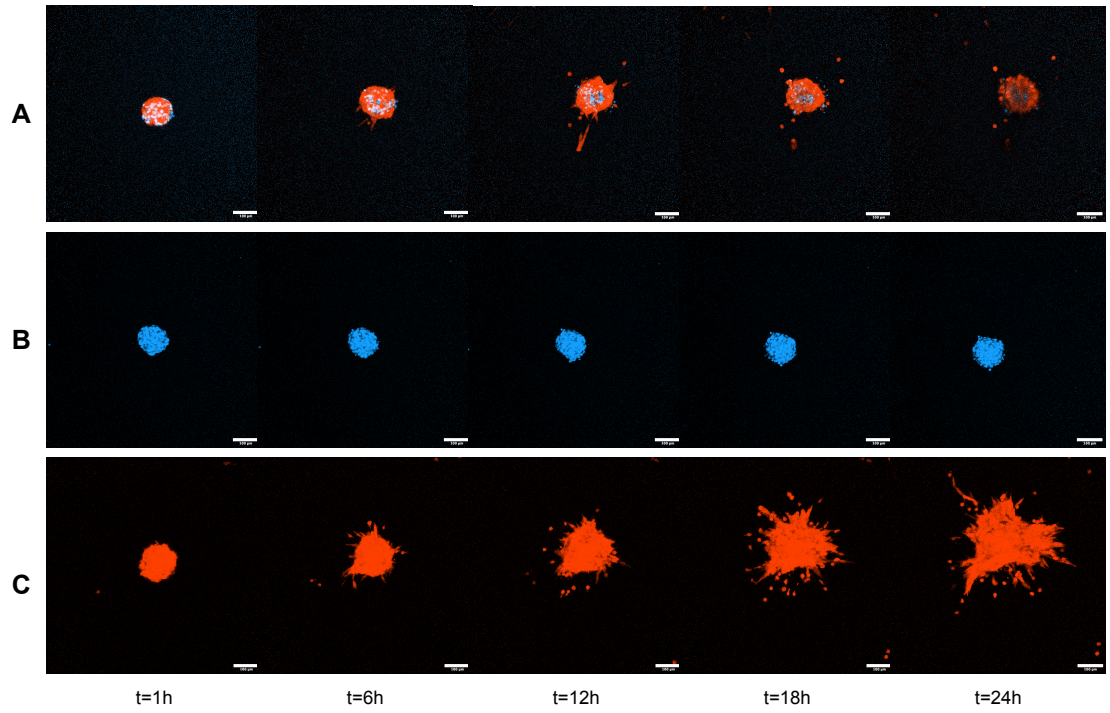

Figure 4.7: Temporal progression of spheroids in 2.4 mg/mL bovine collagen gel. x-axis illustrates time in hours. A) 1:1 heterospheroids, showing the evolution from early compact structures to more irregular shapes. B) Mono NIH3T3 spheroids, which remain relatively compact. C) Mono 4T1 spheroids, displaying rapid expansion and pronounced invasive protrusions over time. Scale bars correspond to 100 µm.

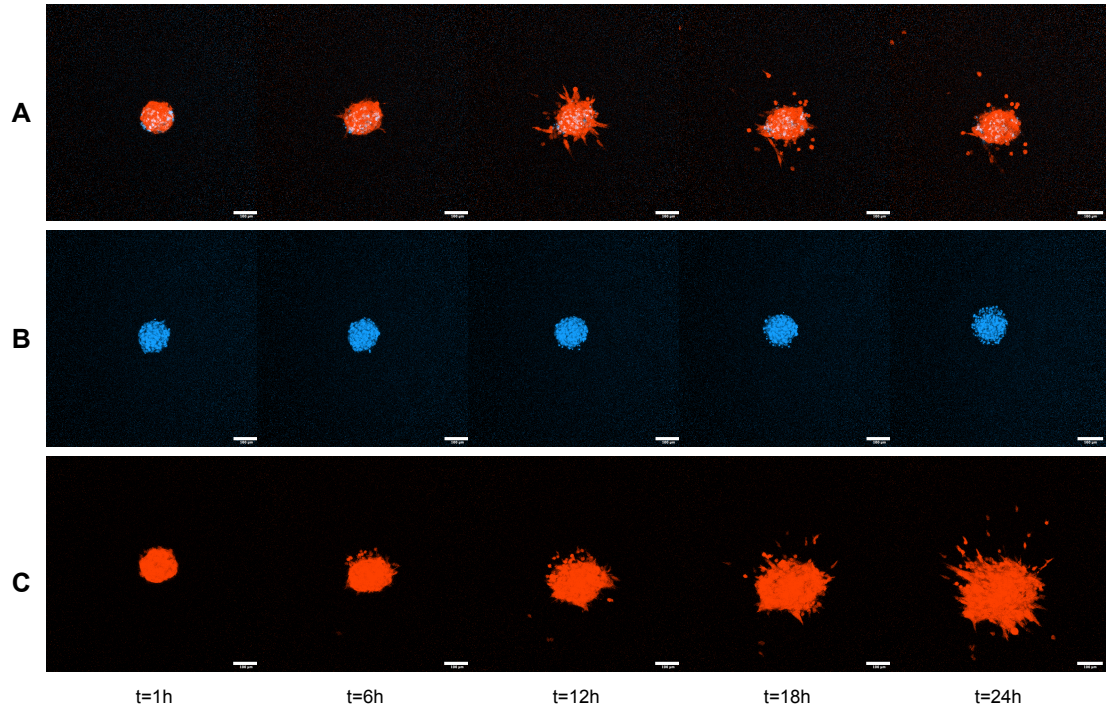

Figure 4.8: Temporal progression of spheroids in 3.3 mg/mL bovine collagen gel. x-axis illustrates time in hours. A) 1:1 heterospheroids, showing the evolution from early compact structures to more irregular and invasive shapes. B) Mono NIH3T3 spheroids, which remain relatively compact, with some cellular dispersion over time. C) Mono 4T1 spheroids, displaying rapid expansion and pronounced invasive protrusions over time. Scale bars correspond to 100 µm.

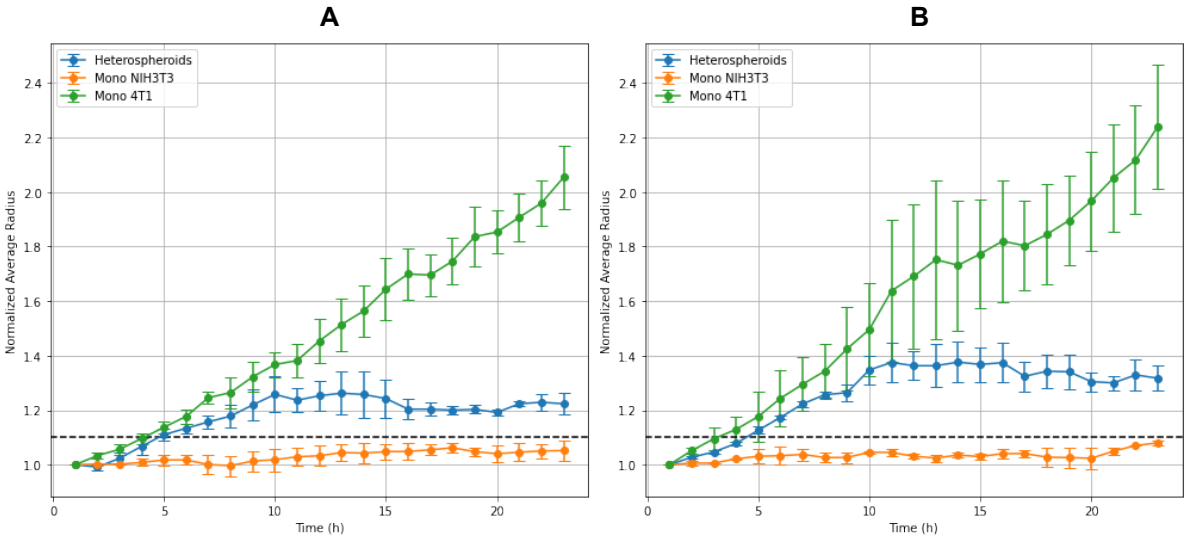

Figure 4.9: Increase in (normalized) radii over time. Invasion onset for each spheroud type is marked by the dashed line. A) 2.4 mg/mL condition. Mono 4T1 spheroids illustrate the most pronounced growth, with early invasion at t = 4h. Heterospheroids illustrated invasion onset at t = 5h. Mono NIH3T3 did not reach the criteria for invasion. B) 3.3 mg/mL condition. Comparable to the left image, mono 4T1 spheroids illustrate the most pronounced growth, with early invasion at t = 3h. Heterospheroids illustrated invasion onset at t = 4h. Mono NIH3T3 only reached invasion at t=24h.

In the 2.4 mg/mL gel condition mono 4T1 spheroids exhibited a sharp and sustained decrease in circularity, from an initial value of 0.7 to below 0.25 within the first 12 hours, which remained low thereafter (Figure 4.10C). This pronounced decline indicates rapid morphological changes consistent with the observed invasive behavior (Figure 4.7C) and active interaction with the surrounding matrix. Mono NIH3T3 spheroids showed a gradual and modest decline in circularity over time, beginning at approximately 0.6 and decreasing to around 0.45 after 24 hours (Figure 4.10B). This mild change implies

limited spreading or elongation of the fibroblast spheroids without significant invasion, as observed in Figure 4.7B. Heterospheroids maintained relatively stable circularity throughout the observation period, fluctuating around an average value of 0.5–0.6 (Figure 4.10A). A transient dip in circularity was observed around 10–12 hours, followed by partial recovery, suggesting moderate structural remodeling with no sustained loss of integrity, as also seen in Figure 4.7A.

In the 3.3 mg/mL gel condition, Mono 4T1 spheroids showed the most aggressive behavior. Circularity dropped sharply from 0.7 to 0.25 within the first 6 hours and remained low (0.2) thereafter (Figure 4.11C). This is indicative of strong invasive activity and rapid disruption of spheroid integrity, as also observed in Figure 4.8. Mono NIH3T3 spheroids displayed relatively stable circularity throughout the experiment, fluctuating around 0.4–0.5 with no consistent directional trend (Figure 4.11B). This indicates that the fibroblast-only spheroids retained their general morphology with minimal invasive behavior, as observed in Figure 4.8. Heterospheroids started with high circularity (0.8) and exhibited a rapid decline within the first 5 hours, plateauing at 0.35 for the remainder of the time course (Figure 4.11, left). This suggests an initial phase of active remodeling or invasion followed by stabilization, as observed in Figure 4.8A.

Interestingly, no significant changes in aspect ratio were observed for any spheroid type (Appendix B). Therefore indicating that the overall shape remained relatively stable throughout the experiment.

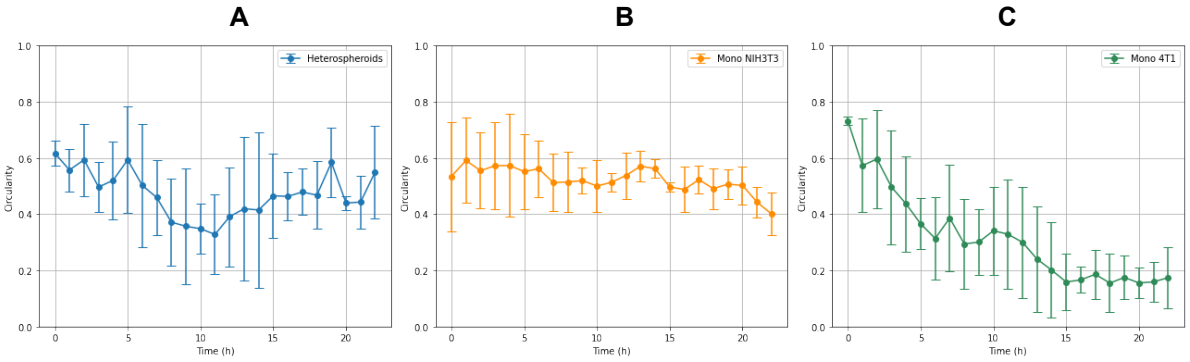

Figure 4.10: Mono 4T1 spheroids illustrate a decrease in circularity in the 2.4 mg/mL gel condition, while mono NIH3T3 spheroids and heterospheroids stay relatively consistent

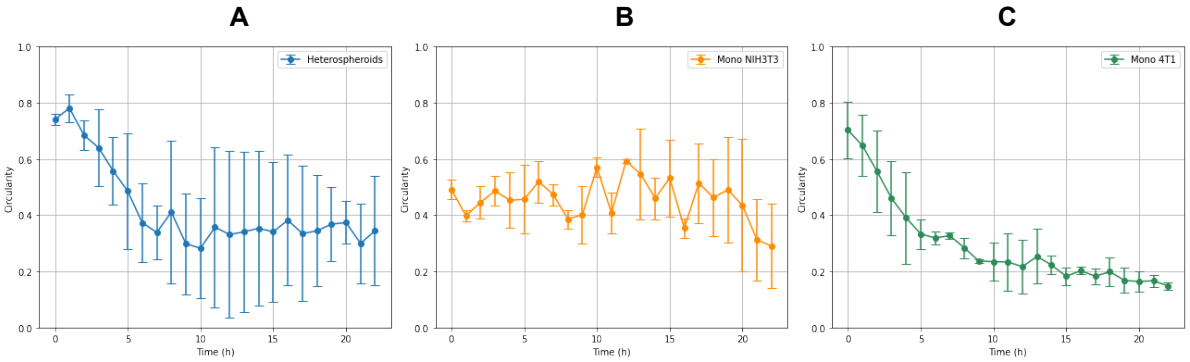

Figure 4.11: Mono 4T1 spheroids illustrate a decrease in circularity in the 3.3 mg/mL gel condition. Mono NIH3T3 spheroids stay relatively consistent, slightly dropping at the end of the experiment. Heterospheroids also illustrate a decrease in circularity

5

Discussion

This study investigated how varying type I collagen concentrations, and thus pore sizes, affect the invasion and growth of 4T1, NIH3T3, and heterogeneous spheroids. To address this, the following central research question was established:

”How does collagen matrix porosity influence invasion of hetero-tumor spheroids?”

The selected collagen concentrations were chosen to model a physiologically relevant ECM known to regulate tumor cell behavior. Low concentration gels (1.5 mg/mL rat tail, 2.4-3.3 mg/mL bovine) promote migration in invasive cancer phenotypes, while high concentration gels (4.0 mg/mL rat tail) suppress motility [32] [12].

The following discussion interprets the findings in relation to this question. Section 5.1 explores the relationship between pore size and source-dependent collagen concentration. Section 5.2 focuses on spheroid behavior in LCCG and HCCG.

5.1. Pore Size and Source-Dependent Variability in Type I Collagen Matrices

Using fibrillar type I collagen gels at varying concentrations, this study found that fibrillar architecture is a key regulator of breast cancer cell invasion. When collagen quality declined, as indicated by the loss of fiber fluorescence, fibrillar structure was lost (Appendix F). Spheroids rapidly migrated out of frame (z-direction), suggesting that fibrillar structures provide essential directional guidance and mechanical support for coordinated invasion. It is well established that aligned collagen fibers can act as physical tracks, guiding and facilitating the directed migration of breast cancer cells into surrounding tissue [21][33].

Fibrillar architecture also influences another critical parameter: pore size. Pore size plays a critical role in replicating the in vivo ECM, influencing cellular behaviors such as metabolism, motility, proliferation, and drug response [20] [60].

5.1.1. Rat Tail Collagen Gels

The 1.5 mg/mL collagen condition exhibited a mean pore size of 0.82 µm, whereas the 4.0 mg/mL condition demonstrated a significantly reduced mean pore size of 0.44 µm (Figure 4.1A). Cameron et al. (2023) observed that rat tail collagen gels at 2 mg/mL and 4.5 mg/mL had pore sizes of approximately 1.3 µm and 0.69 µm, respectively (Table 5.1) [20]. The large standard deviations in their measurements suggest considerable variability, making the pore sizes observed in the current study broadly comparable.

There was an inverse relationship observed between pore size and collagen concentration, similar to previous research [61]. In the 1.5 mg/mL condition, the pore size was relatively large compared to the 4.0 mg/mL condition.

Table 5.1: Comparison between current and reported rat tail collagen pore sizes

Collagen (mg/mL)	Collagen Source	Mean Pore Size(µm)	Reported Mean Pore Size (µm)	Reference
1.5	Rat tail	0.82	–	–
2.0	Rat tail	–	1.3 ± 1.93	[20]
4.0	Rat tail	0.44	–	–
4.5	Rat tail	–	0.69 ± 0.52	[20]

5.1.2. Bovine Collagen Gels

The 2.4 mg/mL collagen condition exhibited a mean pore size of 0.98 µm. This value is consistent with that reported by van der Net et al. (2024), who measured a mean pore size of approximately 1 µm in bovine collagen matrices using epithelial-like and mesenchymal-like cancer cell models. (Table 5.2) [11]. The 3.3 mg/mL condition had a pore size of 0.79 µm. Identifying comparable conditions with accurately reported pore size measurements in the literature proved challenging.

Although the bovine gels also showed an inverse relationship between collagen concentration and pore size, as previously reported [61], the difference in pore sizes between the 2.4 mg/mL and 3.3 mg/mL conditions was minimal.

Table 5.2: Comparison between bovine collagen pore sizes from the current study and literature

Collagen (mg/mL)	Collagen Source	Mean Pore Size (µm)	Reported Mean Pore Size (µm)	Reference
2.4	Bovine	0.98	1.00	[11]
3.3	Bovine	0.79	–	–

5.1.3. Comparison Between Rat Tail and Bovine Collagen Matrices

Both rat tail and bovine collagen gels exhibited a consistent trend: an inverse relationship between collagen concentration and pore size. However, the data revealed a distinct shift in pore size between lower collagen concentrations (1.5, 2.4, and 3.3 mg/mL) and the 4.0 mg/mL collagen concentration. Interestingly, 1.5 mg/mL rat tail collagen exhibited an average pore size between those of 2.4 mg/mL and 3.3 mg/mL bovine collagen (Figure 4.1). This can be attributed to differences in collagen source and fiber architecture. Rat tail collagen typically formed short, randomly oriented fibrils, resulting in a denser network (Appendix F) with smaller pores [62]. Bovine collagen gels featured large, elongated fiber bundles (Appendix F), with larger pores [62][63]. Further explanation can be due to compositional differences: rat tail collagen is pure Type I, whereas bovine collagen contains approximately 95% Type I and 5% Type III collagen, with the latter likely of human origin [64][65][62]. Such source-dependent variations can influence fiber architecture, affecting polymerization behavior and kinetics, and may explain the similar pore size (and spheroid responses) observed across these concentrations [66].

These findings highlight a pronounced source-dependent variability in pore size. Despite the widespread use of collagen type I hydrogels, there remains a limited understanding of how collagen source and extraction methods influence their mechanical behavior and biological performance [66]. This gap is likely due to the inherent complexity of evaluating hydrogels. Their functional properties emerge from a network of interrelated parameters, including fiber architecture, pore size, stiffness, and crosslinking kinetics. These factors are often difficult to isolate or compare across studies [66].

Consequently, relatively few studies have directly linked collagen composition and structure to hydrogel functionality [66]. As the next section demonstrates, these matrix-specific variations in pore architecture have significant consequences for spheroid behavior, particularly in terms of proliferation, invasion dynamics, and morphological adaptation.

5.2. Spheroid Behavior

When comparing all the gels, interestingly the 1.5 mg/mL rat tail (Figure 4.2), 2.4 mg/mL bovine (Figure 4.7), and 3.3 mg/mL bovine (Figure 4.8) yielded similar results in terms of spheroid growth and invasion. This illustrates a comparable porosity across conditions. Therefore, the spheroids from these three gel conditions are analyzed collectively as LCCG.

5.2.1. Spheroid Behavior in LCCG

Mono 4T1

The mono 4T1 spheroids exhibited the most aggressive and radial invasion compared to the heterospheroids or the mono NIH3T3 spheroids (Figures 4.2, 4.7, 4.8). Interestingly, local matrix degradation was exclusively observed in the 1.5 mg/mL rat tail condition, while prominent matrix remodeling was observed in the 1.5 mg/mL rat tail, and 2.4-3.3 mg/mL bovine collagen gels (Figure D.1, Figure D.3, Figure D.4). This suggests that matrix degradation may depend on collagen source and concentration, with rat tail's short fibrils potentially being more susceptible to degradation than the bundled fibers in bovine gels [62].

The observed invasive behavior of the mono 4T1 spheroids aligns with the well-established highly metastatic nature of 4T1 breast cancer cells, suggesting strong intrinsic motility and elevated secretion of matrix-degrading enzymes [31]. Amongst others, increased levels of Urokinase Plasminogen Activator (uPA) proteases, MMP-9, MMP-1, and MMP-2 likely contribute to their enhanced capacity for tissue invasion and metastasis [41][40][37]. uPA converts plasminogen to plasmin, which activates enzymes and growth factors involved in microenvironment remodeling, including MMPs [41]. Among them, MMP-9 is overexpressed in invasive tumors and plays a key role in degrading the ECM and BM, thereby promoting tissue invasion and metastasis [37]. In breast cancer, elevated MMP-9 levels are strongly linked to increased invasiveness [37]. In addition, van der Net et al. (2024) showed that spheroid expansion rate correlates strongly with increased MMP-1 levels [11].

Cancer invasion and metastasis are driven not only by matrix architecture but also by specific tumor subpopulations, CSC, which initiate and sustain metastatic spread [31]. Highly invasive cancers like 4T1 contain CSC and exhibit elevated CXCR4 expression compared to less aggressive types [31]. The invasiveness of mono 4T1 spheroids observed in this study aligns with findings by Krohn et al. (2009), who linked high CXCR4 levels to enhanced invasiveness (see also Subsection 2.1.2) [31]. CXCR4, a key regulator of stem cell migration, is overexpressed in many cancers and linked to heightened metastatic potential, especially in breast cancer. Although not directly quantified here, the observed invasive behavior of 4T1 spheroids indicates the role of CXCR4-mediated chemokine signaling in promoting invasive behavior and metastatic spread.

Mono NIH3T3

In contrast to the mono 4T1 spheroids, mono NIH3T3 spheroids remained compact with minimal to no invasion, displaying only minimal outward migration at later time points (Figures 4.2, 4.7, 4.8). This behavior is consistent with literature that suggests that NAFs, like NIH3T3 cells, generally do not invade surrounding tissue and maintain controlled proliferation and baseline metabolic activity [33]. In contrast, as discussed in Section 2.1, CAFs exhibit distinct biological properties [14]. CAFs are metabolically reprogrammed, rich in glutamine, and express high levels of TEM8. Under chronic nutrient deprivation, a condition driven by the elevated metabolic demands of tumors, cancer cells exploit this glutamine supply to sustain survival [67].

In the LCCG, mono NIH3T3 spheroids exhibited clear signs of matrix remodeling, but no evidence of collagen degradation (Figure D.1, Figure D.3, Figure D.4). Research suggests highly invasive cancer cells have a significantly greater capacity to remodel and degrade the collagen matrix, while the NIH3T3 cell line only moderately affects collagen remodeling [15].

Heterospheroids

In the heterospheroid condition, invasion was intermediate: more invasive than mono NIH3T3 spheroids, but less than mono 4T1 spheroids (Figures 4.2, 4.7, 4.8). Morphologically, 4T1 cells appeared to lead the invasion front, indicating they may drive the outward movement in mixed spheroid populations. This suggests that while fibroblasts are not inherently invasive, they may modulate or support 4T1-mediated invasion. Several mechanisms could underlie this interaction, like ECM remodeling, secretion of signaling molecules, or changes in local matrix mechanics (Subsection 2.1.2).

Fibroblast effects on tumor progression vary with tumor stage and context. While mechanisms remain unclear, tumors may experience both collagen-driven promotion and inhibition, with the net outcome depending on the dominant influence [67]. CAFs from invasive breast tumors promote tumor growth more effectively than NAFs, which can inhibit tumor cell proliferation (Section 2.1). These differences arise from the elevated ECM components, remodeling enzymes, and growth factors like IGF II in CAFs, driving tumor progression [14][28].

Since the NIH3T3 fibroblasts used in the current study are NAFs, they likely inhibited 4T1 cells, resulting in less invasive heterospheroids compared to mono 4T1 spheroids [29]. This finding is con-

sistent with Li et al. (2011), who observed that 4T1 cells proliferate more effectively without fibroblasts, although their study was conducted in Matrigel rather than collagen [24]. Interestingly, heterospheroids seemed to mostly degrade the collagen matrix, rather than remodel (Figure D.1, Figure D.3, Figure D.4). Therefore indicating collagen-mediated tumor promotion [67]. Together, these findings highlight the complex role of fibroblasts and collagen remodeling in modulating tumor invasion and progression within the extracellular matrix.

5.2.2. Spheroid Behavior in HCCG

In the 4.0 mg/mL collagen condition (HCCG), invasion was effectively suppressed across all spheroid types (Figure 4.3). Even the highly invasive 4T1 cells remained confined, with only minimal morphological changes over time (Figure 4.3C). Heterospheroids and mono NIH3T3 spheroids similarly showed no signs of protrusion or outward migration (Figure 4.3A, B). Interestingly, all spheroids in the HCCG maintain high circularity, suggesting that denser matrices physically restrict cell movement. This aligns with van der Net et al. (2024), who reported that denser matrices with smaller pores promote solid-like, non-invasive spheroid behavior [11]. These findings further align with Gkretsi et al. (2017), who reported breast cancer cell invasion and spheroid growth in 0.5–1.0 mg/mL rat tail collagen, but spheroid size reduction at 3.0 mg/mL [68]. Similarly, the current study observed invasion at 1.5 mg/mL but inhibition at 4.0 mg/mL.

While a dense ECM may act as a physical barrier, it can also drive tumor progression by inducing morphological changes that enhance cell migration, trigger EMT, promote invasion and metastasis, and confer resistance to chemotherapy (see also Subsection 2.1.3) [33]. Moreover, ECM fibers can guide invasive behavior, with radially aligned collagen at the tumor-stroma interface supporting local dissemination. This tumor progression was not observed in the current study, as it may require longer experimental durations to develop.

Interestingly, both the mono 4T1 spheroids and the heterospheroids in this condition primarily exhibited collagen degradation (Figure D.2). This might suggest that the small pore size restricts invasion, and the cells have not yet fully adapted to the dense matrix. Nonetheless, the observed degradation could reflect an early phase of collagen-mediated tumor promotion. These findings highlight the critical role of matrix density in regulating invasive behavior through restricted pore size and limited matrix degradation.

Collectively, the findings reinforce the conclusion that matrix porosity, through its influence on fibrillar architecture and steric accessibility (pore size), plays a central role in modulating tumor cell invasion. The lack of a notable difference in cellular behavior and pore size between rat tail and bovine collagens at the low concentrations may be attributed to compositional differences between the sources. An inverse relationship was observed between collagen concentration and pore size.

6

Conclusion

This chapter concludes the main findings in relation to the research question.

This study highlights the key role of collagen pore size and fiber architecture in regulating breast cancer spheroid invasion. Mono 4T1, mono NIH3T3, and 1:1 heterospheroids were embedded in four collagen concentrations: 1.5 and 4.0 mg/mL rat tail, and 2.4 and 3.3 mg/mL bovine, to mimic the ECM. Pore sizes ranged from 0.82 to 0.44 µm, and 0.98 to 0.79; respectively. Although rat tail and bovine concentrations were matched for stiffness [64], their pore sizes differed, indicating that stiffness and porosity are not inherently coupled across sources. Pore size was shown to dictate the degree of invasion, aligning with previous findings [21] [32]. Higher collagen concentrations reduced pore size in both sources. However, differences in collagen source and fiber architecture influenced porosity and consistency. Rat tail collagen formed denser networks with smaller pores, while bovine collagen produced larger bundles with bigger pores [62][63]. As a result, higher concentrations were needed in bovine gels to match the invasion properties of rat tail gels. Furthermore, matrix composition and consistency was more evident in rat tail collagen gels.

This lead to, finally, addressing the research question: How does matrix porosity influence the invasion of hetero-tumor spheroids?

Heterospheroids demonstrated increased invasion in matrices with larger pores (1.5 mg/mL rat tail, 2.4–3.3 mg/mL bovine), where reduced steric hindrance promoted cell migration and outward invasion. Mono 4T1 spheroids invaded most extensively, as they exhibited extensive protrusive activity and matrix infiltration. Heterospheroids also illustrated invasion, though to a lesser extent, suggesting that while fibroblasts (NAFs) contribute to matrix remodeling and paracrine signaling, their presence may also support spheroid cohesion that partially restrains outward migration. Notably, relatively high matrix degradation was observed in heterospheroids. This enhanced degradation may enable greater invasion at longer durations.

In 4.0 mg/mL rat tail collagen gel, smaller pores limited invasion for all spheroid types, including aggressive 4T1 spheroids. All three spheroid types remained compact and circular. Through the reduced pore size, the dense matrix acted as a physical barrier restricting movement and remodeling. Tumor progression likely required a longer experimental duration, either to allow fibroblasts to adopt a more pro-tumorigenic phenotype or for cancer cells to soften and adapt to confined environments by squeezing through smaller pores.

The hypothesis that 4T1 spheroids grow fastest, followed by heterospheroids, and NIH3T3 spheroids slowest was only partly supported. Heterospheroid growth resembled NIH3T3, except for earlier invasion onset, likely due to limited NAFs-to-CAFs transition. Invasion was greater in LCCG with larger pores than in HCCG, confirming pore size as a key determinant of invasion timing.

Interestingly, all heterospheroids, in both the LCCG and HCCG, initially exhibit fibroblasts localized at the periphery (Appendix H). Over time, these fibroblasts migrate toward the core, while the cancer cells move outward. This highlights the aggressive nature of the tumor cells [69]. This could reflect tumor dominance and mimic early metastasis.

Overall, tumor behavior in collagen hydrogels depends on pore size, collagen source, and cell–matrix interactions. LCCG with larger pores promote invasion; HCCG with smaller pores restrict it, highlighting porosity as a crucial determinant in designing realistic in vitro tumor models.

7

Limitations & Recommendations

This study presents encouraging findings on how collagen matrix porosity influences the invasion and growth dynamics of 4T1 breast cancer spheroids, NIH3T3 fibroblast spheroids, and their co-cultures. However, several challenges were encountered during the project, which may have impacted the consistency and reliability of the results. To address these, a set of recommendations is outlined below. Additional suggestions are also provided to guide future research and improve experimental outcomes.

7.1. Challenges of the Current Study

A notable issue was the suspected degradation of rat tail collagen (Appendix F), potentially caused by improper handling during shipping or inherent batch-to-batch variability, with this particular batch exhibiting particularly poor quality. Since the exact onset of collagen degradation could not be determined, it remains unclear which experiments were affected. Therefore, it is strongly recommended to repeat all experiments involving rat tail collagen to ensure the validity of the reported findings.

Another challenge was the vertical migration/sinking of spheroids. This movement out of the focal plane (z-direction) during the 24-hour time-lapse experiments, occured especially when working with highly invasive 4T1 cells. This reduced the number of usable measurements per experiment. To mitigate this in future experiments, a larger matrix volume can be used both for the base layer and for embedding the spheroids. A thicker layer of collagen above and below the spheroid increases mechanical resistance, helping to physically anchor the spheroid and reduce vertical (z-direction) displacement. Additionally, employing z-stack imaging with automated focus correction can help maintain the spheroids within the focal range throughout time-lapse acquisition.

Additionally, the mono 4T1 spheroids in 3.3 mg/mL bovine collagen exhibited large error bars, indicating high variability that warrants experimental repetition. An explanation for the high variability is perhaps that at this intermediate collagen concentration of 3.3 mg/mL, the matrix pore size and stiffness may be less uniform. Circularity measurements across bovine collagen conditions, particularly in heterospheroids, also illustrated substantial variability. This may reflect segmentation inaccuracies stemming from the challenges of multi-channel fluorescence imaging. In heterospheroids, cells are exposed to laser excitation twice per time point, once for each fluorescent label, unlike monospheroids, which require only single-channel imaging. This increased exposure may contribute to photobleaching (Appendix H), reducing signal quality over time. Optimizing segmentation parameters or employing alternative image processing workflows may help improve measurement consistency.

Another limitation was the difficulty in obtaining consistent and comparable matrix stiffness values, such as Storage Modulus and Young's Modulus, from the literature. Differences in collagen source, concentration, gelation protocols, and measurement methods contribute to significant variability. Therefore, it is strongly recommended to perform rheological measurements in-house and under the same experimental conditions. This approach will ensure accurate characterization of matrix mechanics and enable more reliable correlations between stiffness, pore size, and cellular behavior.

7.2. Suggestions for Follow-Up Experiments

While promising, this study presents a simplified model of the TME, using only two cell types in a 1:1 ratio. To improve biological relevance, the ratio of cancer cells to fibroblasts should be selected based on the specific tumor type being modeled. Literature frequently cites cancer cell–to–fibroblast ratios of 1:3 and 1:5, as these proportions better represent stromal-rich tumors. Additionally, delayed seeding, where fibroblasts are introduced 24 hours after cancer cells, has been used to mimic the temporal recruitment of stromal cells during tumor development. These experimental variations significantly affect spheroid organization, invasion dynamics, and matrix remodeling. Thus, further investigation is needed to determine how different cell ratios and seeding strategies influence tumor–stroma interactions and invasive behavior [70]–[76].

To further improve physiological relevance, incorporating additional cell types such as macrophages or endothelial cells could more accurately model the TME and uncover critical cell–cell and cell–matrix dynamics in cancer progression. Macrophages, because they appear early in tumorigenesis and co-evolve with cancer cells, and endothelial cells because they are recruited at later stages. Both play distinct and complementary roles in shaping the TME [13].

Furthermore, the fibroblasts used in this study were NAFs, which may not fully mimic the pro-tumorigenic behavior of CAFs. A more representative approach would involve either using primary CAFs or extending the culture duration to permit NAFs to CAFs transformation, as shown by Orimo et al. (2006), who demonstrated that cancer cells recruit NAFs and induce their myofibroblastic transformation to promote tumor progression (see also Section 2.1) [14].

Another recommended experiment stems from the limitation that, while morphological metrics such as area, circularity, and aspect ratio (Appendix G) provided valuable insights into invasion patterns, the underlying molecular mechanisms, like MMPs activity or SDF-1/CXCR4 signaling, were not directly assessed. This constrains the ability to interpret how matrix porosity influences invasion at a molecular level. To address this, future studies should incorporate pathway-specific inhibitors or molecular blockers. Doing so would allow direct evaluation of the signaling processes driving cancer cell invasion and stromal remodeling, helping to validate the mechanistic hypotheses outlined in Chapter 5.

Another additional future experiment could involve incorporating microfluidic models, which allow for precise analysis of how cell–cell and cell–matrix interactions, matrix stiffness, fluid dynamics (interstitial and shear flow), hypoxia, and biochemical (cytokine and metabolic) gradients influence cancer cell migration [77]. Unlike conventional static in vitro models, microfluidics more accurately replicate the complexity of the TME, enabling the study of both single-cell and collective migration under physiologically relevant conditions.

Finally, to better replicate the complexity of human collagen networks, a hybrid gel composed of both rat tail and bovine collagen may be advantageous. Riedel et al. (2019) suggested that blending these sources can produce collagen networks that more closely resemble in vivo human ECM architecture, potentially enhancing the translational relevance of such in vitro models [60].

Bibliography

[1] *Worldwide cancer data | World Cancer Research Fund*. [Online]. Available: https://www.wcrf.org/preventing-cancer/cancer-statistics/worldwide-cancer-data/#global-cancer-incidence-in-women.

[2] N. Harbeck, F. Penault-Llorca, J. Cortes, *et al.*, "Breast cancer," *Nature Reviews Disease Primers 2019 5:1*, vol. 5, no. 1, pp. 1–31, Sep. 2019, ISSN: 2056-676X. DOI: 10.1038/s41572-019-0111-2. [Online]. Available: https://www.nature.com/articles/s41572-019-0111-2.

[3] *Breast cancer*. [Online]. Available: https://www.who.int/news-room/fact-sheets/detail/breast-cancer.

[4] *BRCA Gene Changes: Cancer Risk and Genetic Testing Fact Sheet - NCI*. [Online]. Available: https://www.cancer.gov/about-cancer/causes-prevention/genetics/brca-fact-sheet.

[5] *Triple-negative Breast Cancer | Details, Diagnosis, and Signs | American Cancer Society*. [Online]. Available: https://www.cancer.org/cancer/types/breast-cancer/about/types-of-breast-cancer/triple-negative.html.

[6] C. Liang, X. Liu, J. Yu, *et al.*, "Hypericin photoactivation induces triple-negative breast cancer cells pyroptosis by targeting the ROS/CALR/Caspase-3/GSDME pathway," *Journal of Advanced Research*, Jan. 2025, ISSN: 2090-1232. DOI: 10.1016/J.JARE.2025.01.042. [Online]. Available: https://linkinghub.elsevier.com/retrieve/pii/S2090123225000591.

[7] W. D. Foulkes, I. E. Smith, and J. S. Reis-Filho, "Triple-Negative Breast Cancer," *New England Journal of Medicine*, vol. 363, no. 20, pp. 1938–1948, Nov. 2010, ISSN: 0028-4793. DOI: 10.1056/NEJMRA1001389. [Online]. Available: https://www.nejm.org/doi/full/10.1056/nejmra1001389.

[8] Z. Zhou, F. Guo, J. Zhang, *et al.*, "Facile integration of a binary nano-prodrug with αPD-L1 as a translatable technology for potent immunotherapy of TNBC," *Acta Biomaterialia*, Jan. 2025, ISSN: 1742-7061. DOI: 10.1016/J.ACTBIO.2025.01.038. [Online]. Available: https://linkinghub.elsevier.com/retrieve/pii/S1742706125000467.

[9] *Triple Negative Breast Cancer (TNBC) | Penn Medicine*. [Online]. Available: https://www.pennmedicine.org/conditions/triple-negative-breast-cancer#.

[10] S. D. Siegel, M. M. Brooks, J. D. Berman, *et al.*, "Neighborhood factors and triple negative breast cancer: The role of cumulative exposure to area□level risk factors," *Cancer Medicine*, vol. 12, no. 10, p. 11 760, May 2023, ISSN: 20457634. DOI: 10.1002/CAM4.5808. [Online]. Available: https://pmc.ncbi.nlm.nih.gov/articles/PMC10242317/.

[11] A. van der Net, Z. Rahman, A. D. Bordoloi, *et al.*, "EMT-related cell-matrix interactions are linked to states of cell unjamming in cancer spheroid invasion," *iScience*, vol. 27, no. 12, p. 111 424, Dec. 2024, ISSN: 25890042. DOI: 10.1016/J.ISCI.2024.111424. [Online]. Available: https://pmc.ncbi.nlm.nih.gov/articles/PMC11665421/.

[12] T. Yuan, D. Gao, S. Li, and Y. Jiang, "Co-culture of tumor spheroids and monocytes in a collagen matrix-embedded microfluidic device to study the migration of breast cancer cells," *Chinese Chemical Letters*, vol. 30, no. 2, pp. 331–336, Feb. 2019, ISSN: 1001-8417. DOI: 10.1016/J.CCLET.2018.07.013.

[13] D. Rama-Esendagli, G. Esendagli, G. Yilmaz, and D. Guc, "Spheroid formation and invasion capacity are differentially influenced by co-cultures of fibroblast and macrophage cells in breast cancer," *Molecular Biology Reports*, vol. 41, no. 5, pp. 2885–2892, Jan. 2014, ISSN: 15734978. DOI: 10.1007/S11033-014-3144-3/FIGURES/5. [Online]. Available: https://link.springer.com/article/10.1007/s11033-014-3144-3.

[14] A. Orimo and R. A. Weinberg, “Stromal fibroblasts in cancer: A novel tumor-promoting cell type,” *Cell Cycle*, vol. 5, no. 15, pp. 1597–1601, Aug. 2006, ISSN: 15514005. DOI: 10.4161/CC.5.15.3112. [Online]. Available: https://www.tandfonline.com/action/journalInformation?journalCode=kccy20.

[15] C. L. Chiu, M. A. Digman, and E. Gratton, “Cell Matrix Remodeling Ability Shown by Image Spatial Correlation,” *Journal of Biophysics*, vol. 2013, no. 1, p. 532 030, Jan. 2013, ISSN: 1687-8019. DOI: 10.1155/2013/532030. [Online]. Available: https://onlinelibrary.wiley.com/doi/full/10.1155/2013/532030%20https://onlinelibrary.wiley.com/doi/abs/10.1155/2013/532030%20https://onlinelibrary.wiley.com/doi/10.1155/2013/532030.

[16] M. Plodinec, M. Loparic, C. A. Monnier, *et al.*, “The nanomechanical signature of breast cancer,” *NATURE NANOTECHNOLOGY* |, vol. 7, 2012. DOI: 10.1038/NNANO.2012.167. [Online]. Available: www.nature.com/naturenanotechnology.

[17] J. Alcaraz, H. Mori, C. M. Ghajar, D. Brownfield, R. Galgoczy, and M. J. Bissell, “Collective epithelial cell invasion overcomes mechanical barriers of collagenous extracellular matrix by a narrow tube-like geometry and MMP14-dependent local softening,” *Integrative Biology*, vol. 3, no. 12, pp. 1153–1166, Dec. 2011, ISSN: 17579694. DOI: 10.1039/C1IB00073J. [Online]. Available: https://dx.doi.org/10.1039/c1ib00073j.

[18] G. Wishart, P. Gupta, G. Schettino, A. Nisbet, and E. Velliou, “3d tissue models as tools for radiotherapy screening for pancreatic cancer,” *The British Journal of Radiology*, vol. 94, no. 1120, p. 20 201 397, Apr. 2021, ISSN: 1748880X. DOI: 10.1259/BJR.20201397. [Online]. Available: https://pmc.ncbi.nlm.nih.gov/articles/PMC8010544/.

[19] S. C. Brüningk, I. Rivens, C. Box, U. Oelfke, and G. ter Haar, “3D tumour spheroids for the prediction of the effects of radiation and hyperthermia treatments,” *Scientific Reports 2020 10:1*, vol. 10, no. 1, pp. 1–13, Feb. 2020, ISSN: 2045-2322. DOI: 10.1038/s41598-020-58569-4. [Online]. Available: https://www.nature.com/articles/s41598-020-58569-4.

[20] A. P. Cameron, S. Gao, Y. Liu, and C. X. Zhao, “Impact of hydrogel biophysical properties on tumor spheroid growth and drug response,” *Biomaterials Advances*, vol. 149, p. 213 421, Jun. 2023, ISSN: 2772-9508. DOI: 10.1016/J.BIOADV.2023.213421.

[21] A. Guzman, M. J. Ziperstein, and L. J. Kaufman, “The effect of fibrillar matrix architecture on tumor cell invasion of physically challenging environments,” *Biomaterials*, vol. 35, no. 25, pp. 6954–6963, Aug. 2014, ISSN: 0142-9612. DOI: 10.1016/J.BIOMATERIALS.2014.04.086.

[22] G. Hassan, S. M. Afify, S. Kitano, *et al.*, “Cancer Stem Cell Microenvironment Models with Biomaterial Scaffolds In Vitro,” *Processes 2021, Vol. 9, Page 45*, vol. 9, no. 1, p. 45, Dec. 2020, ISSN: 2227-9717. DOI: 10.3390/PR9010045. [Online]. Available: https://www.mdpi.com/2227-9717/9/1/45/htm%20https://www.mdpi.com/2227-9717/9/1/45.

[23] N. M. Anderson and M. C. Simon, “Tumor Microenvironment,” *Current biology : CB*, vol. 30, no. 16, R921, Aug. 2020, ISSN: 18790445. DOI: 10.1016/J.CUB.2020.06.081. [Online]. Available: https://pmc.ncbi.nlm.nih.gov/articles/PMC8194051/.

[24] L. Li and Y. Lu, “Optimizing a 3D Culture System to Study the Interaction between Epithelial Breast Cancer and Its Surrounding Fibroblasts,” *Journal of Cancer*, vol. 2, no. 1, pp. 458–466, 2011, ISSN: 1837-9664. DOI: 10.7150/JCA.2.458. [Online]. Available: http://www.jcancer.org.

[25] I. Dagogo-Jack and A. T. Shaw, “Tumour heterogeneity and resistance to cancer therapies,” *Nature Reviews Clinical Oncology 2017 15:2*, vol. 15, no. 2, pp. 81–94, Nov. 2017, ISSN: 1759-4782. DOI: 10.1038/nrclinonc.2017.166. [Online]. Available: https://www.nature.com/articles/nrclinonc.2017.166.

[26] S. L. Floor, J. E. Dumont, C. Maenhaut, and E. Raspe, “Hallmarks of cancer: of all cancer cells, all the time?” *Trends in Molecular Medicine*, vol. 18, no. 9, pp. 509–515, Sep. 2012, ISSN: 1471-4914. DOI: 10.1016/J.MOLMED.2012.06.005.

[27] D. P. Simon and G. D. Hammer, “Adrenocortical stem and progenitor cells: Implications for adrenocortical carcinoma,” *Molecular and Cellular Endocrinology*, vol. 351, no. 1, pp. 2–11, Mar. 2012, ISSN: 0303-7207. DOI: 10.1016/J.MCE.2011.12.006.

[28] A. Sadlonova, Z. Novak, M. R. Johnson, *et al.*, "Breast fibroblasts modulate epithelial cell proliferation in three-dimensional in vitro co-culture.," *Breast cancer research : BCR*, vol. 7, no. 1, pp. 1–14, Nov. 2005, ISSN: 1465542X. DOI: 10.1186/BCR949/FIGURES/8. [Online]. Available: https://link.springer.com/articles/10.1186/bcr949%20https://link.springer.com/article/10.1186/bcr949.

[29] Y. Zhao, M. Shen, L. Wu, *et al.*, "Stromal cells in the tumor microenvironment: accomplices of tumor progression?" *Cell Death & Disease 2023 14:9*, vol. 14, no. 9, pp. 1–24, Sep. 2023, ISSN: 2041-4889. DOI: 10.1038/s41419-023-06110-6. [Online]. Available: https://www.nature.com/articles/s41419-023-06110-6.

[30] Z. Mai, Y. Lin, P. Lin, X. Zhao, and L. Cui, "Modulating extracellular matrix stiffness: a strategic approach to boost cancer immunotherapy," *Cell Death & Disease 2024 15:5*, vol. 15, no. 5, pp. 1–16, May 2024, ISSN: 2041-4889. DOI: 10.1038/s41419-024-06697-4. [Online]. Available: https://www.nature.com/articles/s41419-024-06697-4.

[31] A. Krohn, Y. H. Song, F. Muehlberg, L. Droll, C. Beckmann, and E. Alt, "CXCR4 receptor positive spheroid forming cells are responsible for tumor invasion in vitro," *Cancer Letters*, vol. 280, no. 1, pp. 65–71, Jul. 2009, ISSN: 0304-3835. DOI: 10.1016/J.CANLET.2009.02.005.

[32] Y. Li and E. Kumacheva, "Hydrogel microenvironments for cancer spheroid growth and drug screening," *Science Advances*, vol. 4, no. 4, Apr. 2018, ISSN: 23752548. DOI: 10.1126/SCIADV.AAS8998/ASSET/698EF8B6-4AF7-4C8D-91B4-A5F230963787/ASSETS/GRAPHIC/AAS8998-F5.JPEG. [Online]. Available: https://www.science.org/doi/10.1126/sciadv.aas8998.

[33] K. Beslmüller, R. R. d. Mercado, G. H. Koenderink, E. H. Danen, and T. Schmidt, "Matrix stiffness affects spheroid invasion, collagen remodeling and the effective reach of stress into the ECM," *bioRxiv*, p. 2025.03.14.643241, Mar. 2025. DOI: 10.1101/2025.03.14.643241. [Online]. Available: https://www.biorxiv.org/content/10.1101/2025.03.14.643241v1%20https://www.biorxiv.org/content/10.1101/2025.03.14.643241v1.abstract.

[34] J. Tien, U. Ghani, Y. W. Dance, *et al.*, "Matrix Pore Size Governs Escape of Human Breast Cancer Cells from a Microtumor to an Empty Cavity," *iScience*, vol. 23, no. 11, p. 101 673, Nov. 2020, ISSN: 25890042. DOI: 10.1016/J.ISCI.2020.101673. [Online]. Available: https://pmc.ncbi.nlm.nih.gov/articles/PMC7599434/.

[35] B. K. Brisson, B. Dekky, A. C. Berger, *et al.*, "Tumor-restrictive type III collagen in the breast cancer microenvironment: prognostic and therapeutic implications," *Research Square*, rs.3.rs–2 631 314, Apr. 2023, ISSN: 23744677. DOI: 10.21203/RS.3.RS-2631314/V1. [Online]. Available: https://pmc.ncbi.nlm.nih.gov/articles/PMC10120781/.

[36] M. Badaoui, C. Mimsy-Julienne, C. Saby, *et al.*, "Collagen type 1 promotes survival of human breast cancer cells by overexpressing Kv10.1 potassium and Orai1 calcium channels through DDR1-dependent pathway," *Oncotarget*, vol. 9, no. 37, p. 24 653, May 2017, ISSN: 19492553. DOI: 10.18632/ONCOTARGET.19065. [Online]. Available: https://pmc.ncbi.nlm.nih.gov/articles/PMC5973854/.

[37] H. S. Lee, A. W. Ha, and W. K. Kim, "Effect of resveratrol on the metastasis of 4T1 mouse breast cancer cells in vitro and in vivo," *Nutrition Research and Practice*, vol. 6, no. 4, pp. 294–300, Aug. 2012, ISSN: 19761457. DOI: 10.4162/NRP.2012.6.4.294. [Online]. Available: https://synapse.koreamed.org/articles/1051228.

[38] P. Blázquez-Carmona, R. Ruiz-Mateos, J. Barrasa-Fano, *et al.*, "Quantitative atlas of collagen hydrogels reveals mesenchymal cancer cell traction adaptation to the matrix nanoarchitecture," *Acta Biomaterialia*, vol. 185, pp. 281–295, Sep. 2024, ISSN: 1742-7061. DOI: 10.1016/J.ACTBIO.2024.07.002.

[39] S. Banerjee, W. C. Lo, P. Majumder, *et al.*, "Multiple roles for basement membrane proteins in cancer progression and EMT," *European Journal of Cell Biology*, vol. 101, no. 2, p. 151 220, Apr. 2022, ISSN: 0171-9335. DOI: 10.1016/J.EJCB.2022.151220.

[40] R. Zhou, L. Xu, M. Ye, M. Liao, H. Du, and H. Chen, "Formononetin inhibits migration and invasion of MDA-MB-231 and 4T1 breast cancer cells by suppressing MMP-2 and MMP-9 through PI3K/AKT signaling pathways," *Hormone and Metabolic Research*, vol. 46, no. 11, pp. 753–760, 2014, ISSN: 14394286. DOI: 10.1055/S-0034-1376977/ID/R2014-01-0020-0011/BIB. [Online]. Available: http://www.thieme-connect.com/products/ejournals/html/10.1055/s-0034-1376977%20http://www.thieme-connect.de/DOI/DOI?10.1055/s-0034-1376977.

[41] B. Afsharimani, J. Baran, S. Watanabe, D. Lindner, P. J. Cabot, and M. O. Parat, "Morphine and breast tumor metastasis: The role of matrix-degrading enzymes," *Clinical and Experimental Metastasis*, vol. 31, no. 2, pp. 149–158, Feb. 2014, ISSN: 02620898. DOI: 10.1007/S10585-013-9616-3/FIGURES/6. [Online]. Available: https://link.springer.com/article/10.1007/s10585-013-9616-3.

[42] S. L. Ham, R. Joshi, G. D. Luker, and H. Tavana, "Engineered Breast Cancer Cell Spheroids Reproduce Biologic Properties of Solid Tumors," *Advanced Healthcare Materials*, vol. 5, no. 21, pp. 2788–2798, Nov. 2016, ISSN: 2192-2659. DOI: 10.1002/ADHM.201600644. [Online]. Available: https://onlinelibrary.wiley.com/doi/full/10.1002/adhm.201600644%20https://onlinelibrary.wiley.com/doi/abs/10.1002/adhm.201600644%20https://advanced.onlinelibrary.wiley.com/doi/10.1002/adhm.201600644.

[43] Y. Xiao and D. Yu, "Tumor microenvironment as a therapeutic target in cancer," *Pharmacology & therapeutics*, vol. 221, p. 107 753, May 2020, ISSN: 1879016X. DOI: 10.1016/J.PHARMTHERA.2020.107753. [Online]. Available: https://pmc.ncbi.nlm.nih.gov/articles/PMC8084948/.

[44] D. Lv, Z. Hu, L. Lu, H. Lu, and X. Xu, "Three-dimensional cell culture: A powerful tool in tumor research and drug discovery," *Oncology Letters*, vol. 14, no. 6, p. 6999, Dec. 2017, ISSN: 17921082. DOI: 10.3892/OL.2017.7134. [Online]. Available: https://pmc.ncbi.nlm.nih.gov/articles/PMC5754907/.

[45] L. Chen, Z. Xiao, Y. Meng, *et al.*, "The enhancement of cancer stem cell properties of MCF-7 cells in 3D collagen scaffolds for modeling of cancer and anti-cancer drugs," *Biomaterials*, vol. 33, no. 5, pp. 1437–1444, Feb. 2012, ISSN: 0142-9612. DOI: 10.1016/J.BIOMATERIALS.2011.10.056.

[46] E. C. Costa, A. F. Moreira, D. de Melo-Diogo, V. M. Gaspar, M. P. Carvalho, and I. J. Correia, "3D tumor spheroids: an overview on the tools and techniques used for their analysis," *Biotechnology Advances*, vol. 34, no. 8, pp. 1427–1441, Dec. 2016, ISSN: 0734-9750. DOI: 10.1016/J.BIOTECHADV.2016.11.002.

[47] F. Pampaloni, E. G. Reynaud, and E. H. Stelzer, "The third dimension bridges the gap between cell culture and live tissue," *Nature Reviews Molecular Cell Biology 2007 8:10*, vol. 8, no. 10, pp. 839–845, Oct. 2007, ISSN: 1471-0080. DOI: 10.1038/nrm2236. [Online]. Available: https://www.nature.com/articles/nrm2236.

[48] W. H. Abuwatfa, W. G. Pitt, and G. A. Husseini, "Scaffold-based 3D cell culture models in cancer research," *Journal of Biomedical Science 2024 31:1*, vol. 31, no. 1, pp. 1–39, Jan. 2024, ISSN: 1423-0127. DOI: 10.1186/S12929-024-00994-Y. [Online]. Available: https://jbiomedsci.biomedcentral.com/articles/10.1186/s12929-024-00994-y%20http://creativecommons.org/publicdomain/zero/1.0/.

[49] A. Cacciamali, R. Villa, and S. Dotti, "3D Cell Cultures: Evolution of an Ancient Tool for New Applications," *Frontiers in Physiology*, vol. 13, p. 836 480, Jul. 2022, ISSN: 1664042X. DOI: 10.3389/FPHYS.2022.836480. [Online]. Available: https://pmc.ncbi.nlm.nih.gov/articles/PMC9353320/.

[50] *Three-dimensional breast cancer spheroids for preclinical assessment | TU Delft Repository*. [Online]. Available: https://repository.tudelft.nl/record/uuid:79c7dc29-f806-4022-8231-8beddc567853.

[51] *Sci-Hub | Engineering Multi□Cellular Spheroids for Tissue Engineering and Regenerative Medicine. Advanced Healthcare Materials, 2000608 | 10.1002/adhm.202000608*. [Online]. Available: https://sci-hub.se/https://doi.org/10.1002/adhm.202000608.

[52] S. L. Maguire, B. Peck, P. T. Wai, *et al.*, "Three-dimensional modelling identifies novel genetic dependencies associated with breast cancer progression in the isogenic MCF10 model," *The Journal of Pathology*, vol. 240, no. 3, pp. 315–328, Nov. 2016, ISSN: 1096-9896. DOI: 10.1002/PATH.4778. [Online]. Available: https://onlinelibrary.wiley.com/doi/full/10.1002/path.4778%20https://onlinelibrary.wiley.com/doi/abs/10.1002/path.4778%20https://pathsocjournals.onlinelibrary.wiley.com/doi/10.1002/path.4778.

[53] S. Nath and G. R. Devi, "Three-Dimensional Culture Systems in Cancer Research: Focus on Tumor Spheroid Model," *Pharmacology & therapeutics*, vol. 163, p. 94, Jul. 2016, ISSN: 1879016X. DOI: 10.1016/J.PHARMTHERA.2016.03.013. [Online]. Available: https://pmc.ncbi.nlm.nih.gov/articles/PMC4961208/.

[54] Y. L. Yang, L. M. Leone, and L. J. Kaufman, "Elastic moduli of collagen gels can be predicted from two-dimensional confocal microscopy," *Biophysical Journal*, vol. 97, no. 7, pp. 2051–2060, Oct. 2009, ISSN: 15420086. DOI: 10.1016/j.bpj.2009.07.035. [Online]. Available: https://www.cell.com/action/showFullText?pii=S0006349509012995%20https://www.cell.com/action/showAbstract?pii=S0006349509012995%20https://www.cell.com/biophysj/abstract/S0006-3495(09)01299-5.

[55] *Sci-Hub | Three-dimensional collagenous niche and azacytidine selectively promote time-dependent cardiomyogenesis from human bone marrow-derived MSC spheroids. Biotechnology and Bioengineering, 115(8), 2013–2026 | 10.1002/bit.26714*. [Online]. Available: https://sci-hub.se/10.1002/bit.26714.

[56] A. D. Doyle, "Generation of 3D collagen gels with controlled, diverse architectures," *Current protocols in cell biology / editorial board, Juan S. Bonifacino ... [et al.]*, vol. 72, p. 10.20.1, 2016, ISSN: 19342616. DOI: 10.1002/CPCB.9. [Online]. Available: https://pmc.ncbi.nlm.nih.gov/articles/PMC5030718/.

[57] V. V. Artym and K. Matsumoto, "Imaging Cells in Three-Dimensional Collagen Matrix," *Current protocols in cell biology / editorial board, Juan S. Bonifacino ... [et al.]*, vol. CHAPTER, no. SUPP.48, Unit, 2010, ISSN: 19342500. DOI: 10.1002/0471143030.CB1018S48. [Online]. Available: https://pmc.ncbi.nlm.nih.gov/articles/PMC2988473/.

[58] *Introduction*. [Online]. Available: https://imagej.net/learn/.

[59] A. E. Carpenter, T. R. Jones, M. R. Lamprecht, *et al.*, "CellProfiler: Image analysis software for identifying and quantifying cell phenotypes," *Genome Biology*, vol. 7, no. 10, pp. 1–11, Oct. 2006, ISSN: 14747596. DOI: 10.1186/GB-2006-7-10-R100/FIGURES/4. [Online]. Available: https://genomebiology.biomedcentral.com/articles/10.1186/gb-2006-7-10-r100.

[60] S. Riedel, P. Hietschold, C. Krömmelbein, *et al.*, "Design of biomimetic collagen matrices by reagent-free electron beam induced crosslinking: Structure-property relationships and cellular response," *Materials & Design*, vol. 168, p. 107 606, Apr. 2019, ISSN: 0264-1275. DOI: 10.1016/J.MATDES.2019.107606.

[61] A. Hayn, T. Fischer, and C. T. Mierke, "Inhomogeneities in 3D Collagen Matrices Impact Matrix Mechanics and Cancer Cell Migration," *Frontiers in Cell and Developmental Biology*, vol. 8, p. 593 879, Nov. 2020, ISSN: 2296634X. DOI: 10.3389/FCELL.2020.593879/FULL. [Online]. Available: https://pmc.ncbi.nlm.nih.gov/articles/PMC7674772/.

[62] Y. Shinsato, A. D. Doyle, W. Li, and K. M. Yamada, "Direct comparison of five different 3D extracellular matrix model systems for characterization of cancer cell migration," *Cancer Reports*, vol. 3, no. 5, e1257, Oct. 2020, ISSN: 25738348. DOI: 10.1002/CNR2.1257. [Online]. Available: https://pmc.ncbi.nlm.nih.gov/articles/PMC7941507/.

[63] *Collagen Type I, Rat Tail or Bovine | 3D Cell Culture | ibidi*. [Online]. Available: https://ibidi.com/collagen/107-collagen-type-i.html#specifications.

[64] *Advanced BioMatrix - PureCol® Solution, 3 mg/ml (bovine) #5005*. [Online]. Available: https://advancedbiomatrix.com/purecol/.

[65] *354249 | Corning® Collagen I, High Concentration, Rat Tail, 100 mg | Corning*. [Online]. Available: https://ecatalog.corning.com/life-sciences/b2c/US/en/Surfaces/Extracellular-Matrices-ECMs/Corning%C2%AE-Collagen/p/354249.

[66] M. Pires Figueiredo, S. Rodríguez-Fernández, F. Copes, and D. Mantovani, "Review of collagen type I-based hydrogels: focus on composition-structure-properties relationships," *npj Biomedical Innovations 2025 2:1*, vol. 2, no. 1, pp. 1–21, May 2025, ISSN: 3005-1444. DOI: 10.1038/s44385-025-00018-w. [Online]. Available: https://www.nature.com/articles/s44385-025-00018-w.

[67] K. S. Hsu, J. M. Dunleavey, C. Szot, *et al.*, "Cancer cell survival depends on collagen uptake into tumor-associated stroma," *Nature Communications 2022 13:1*, vol. 13, no. 1, pp. 1–18, Nov. 2022, ISSN: 2041-1723. DOI: 10.1038/s41467-022-34643-5. [Online]. Available: https://www.nature.com/articles/s41467-022-34643-5.

[68] V. Gkretsi, A. Stylianou, M. Louca, and T. Stylianopoulos, "Identification of Ras suppressor-1 (RSU-1) as a potential breast cancer metastasis biomarker using a three-dimensional in vitro approach," *Oncotarget*, vol. 8, no. 16, p. 27 364, 2017, ISSN: 19492553. DOI: 10.18632/ONCOTARGET.16062. [Online]. Available: https://pmc.ncbi.nlm.nih.gov/articles/PMC5432341/.

[69] B. A. Pulaski and S. Ostrand-Rosenberg, "Mouse 4T1 Breast Tumor Model," *Current Protocols in Immunology*, vol. 39, no. 1, pp. 1–20, Oct. 2000, ISSN: 1934-368X. DOI: 10.1002/0471142735.IM2002S39. [Online]. Available: https://onlinelibrary.wiley.com/doi/full/10.1002/0471142735.im2002s39%20https://onlinelibrary.wiley.com/doi/abs/10.1002/0471142735.im2002s39%20https://currentprotocols.onlinelibrary.wiley.com/doi/10.1002/0471142735.im2002s39.

[70] I. Yakavets, A. Francois, A. Benoit, J. L. Merlin, L. Bezdetnaya, and G. Vogin, "Advanced co-culture 3D breast cancer model for investigation of fibrosis induced by external stimuli: optimization study," *Scientific Reports*, vol. 10, no. 1, pp. 1–11, 2020, ISSN: 20452322. DOI: 10.1038/s41598-020-78087-7. [Online]. Available: https://doi.org/10.1038/s41598-020-78087-7.

[71] S. Singh, S. Tran, J. Putman, and H. Tavana, "Three-dimensional models of breast cancer–fibroblasts interactions," *Experimental Biology and Medicine*, vol. 245, no. 10, pp. 879–888, 2020, ISSN: 15353699. DOI: 10.1177/1535370220917366.

[72] S. Hofmann, R. Cohen-Harazi, Y. Maizels, and I. Koman, "Patient-derived tumor spheroid cultures as a promising tool to assist personalized therapeutic decisions in breast cancer," *Translational Cancer Research*, vol. 11, no. 1, pp. 134–147, 2022, ISSN: 22196803. DOI: 10.21037/tcr-21-1577.

[73] B. S. Nielsen, N. H. Madsen, J. Larsen, I. Skandorff, M. Gad, and K. Holmstrøm, "Architectural organization and molecular profiling of 3D cancer heterospheroids and their application in drug testing," *Frontiers in Oncology*, vol. 14, no. July, pp. 1–13, 2024, ISSN: 2234943X. DOI: 10.3389/fonc.2024.1386097.

[74] Z. Huang, P. Yu, and J. Tang, "Characterization of triple-negative breast cancer MDA-MB-231 cell spheroid model," *OncoTargets and Therapy*, vol. 13, pp. 5395–5405, 2020, ISSN: 11786930. DOI: 10.2147/OTT.S249756.

[75] D. L. Priwitaningrum, J. B. G. Blondé, A. Sridhar, *et al.*, "Tumor stroma-containing 3D spheroid arrays: A tool to study nanoparticle penetration," *Journal of Controlled Release*, vol. 244, pp. 257–268, 2016, ISSN: 18734995. DOI: 10.1016/j.jconrel.2016.09.004. [Online]. Available: http://dx.doi.org/10.1016/j.jconrel.2016.09.004.

[76] D. L. Priwitaningrum, K. Pednekar, A. V. Gabriël, *et al.*, "Evaluation of paclitaxel-loaded polymeric nanoparticles in 3D tumor model: impact of tumor stroma on penetration and efficacy," *Drug Delivery and Translational Research*, vol. 13, no. 5, pp. 1470–1483, 2023, ISSN: 21903948. DOI: 10.1007/s13346-023-01310-1. [Online]. Available: https://doi.org/10.1007/s13346-023-01310-1.

[77] P. Mehta, Z. Rahman, P. ten Dijke, and P. E. Boukany, "Microfluidics meets 3D cancer cell migration," *Trends in Cancer*, vol. 8, no. 8, pp. 683–697, Aug. 2022, ISSN: 24058033. DOI: 10.1016/J.TRECAN.2022.03.006/ASSET/A9803112-355A-4799-8597-06509A6180BB/MAIN.ASSETS/GR3.JPG. [Online]. Available: https://www.cell.com/action/showFullText?pii=S2405803322000723%20https://www.cell.com/action/showAbstract?pii=S2405803322000723%20https://www.cell.com/trends/cancer/abstract/S2405-8033(22)00072-3.

[78] *10x PBS buffer (10x Phosphate Buffered Saline)*. [Online]. Available: https://www.lifescience.net/protocols/34/10x-pbs-buffer-10x-phosphate-buffered-saline/.

A

List of Reagents Used

A.1. Cell Culture Reagents

Below is a table containing all the chemicals used for cell culture

Table A.1: Reagents used for cell culture.

Material	Supplier	Article Number
70% Ethanol	Central warehouse L&M	WH001483
DMEM 1x	Thermo Fisher Scientific (via website voor life, Acros Invitrogen, Pierce)	11574546
RPMI 1x	Thermo Fisher Scientific (via website voor life, Acros Invitrogen, Pierce)	11504566
Trypsin	Thermo Fisher Scientific (via website voor life, Acros Invitrogen, Pierce)	11570626
FBS (Fetal Bovine Serum)	Thermo Fisher Scientific (via website voor life, Acros Invitrogen, Pierce)	11560636
Anti-Anti (Antibiotic-Antimycotic)	Merck Sigma	A5955-100ML
DPBS 1x	Thermo Fisher Scientific (via website voor life, Acros Invitrogen, Pierce)	12559069
4T1 Mouse Mammary Cells	TU Delft, ChemE Department	n/a
NIH3T3 Mouse Fibroblast Cells	TU Delft, ChemE Department	n/a

A.2. Collagen Gel Preparation Reagents

Below is a table containing all the chemicals used for collagen gels

Table A.2: Reagents used for collagen preparation.

Material	Supplier	Article Number
$NaHCO_3$	J. T. Baker	0263-1kg
HEPES	Merck Sigma	H3375-100G
10x DMEM	Thermo Fisher Scientific (via website voor life, Acros Invitrogen, Pierce)	11584486
NaOH Pellets	VWR (Avantor) International BV	1.06498.1000
MilliQ Water	n/a	n/a
NaCl	Central warehouse L&M	WH001042
KCl	Central warehouse L&M	WH001035
Na_2HPO_4	Merck Sigma	71643-1KG
KH_2PO_4	Merck Sigma	P5655-500G
HCl	Hach	884-49
Rat Tail Collagen (11.23 mg/mL)	Corning	-
Bovine Collagen (10 mg/mL)	Advanced BioMatrix	-

A.3. Buffers

10x RB Buffer: 1.1 g $NaHCO_3$ + 2.4 g HEPES. Fill to 50 mL with MilliQ water [56].

0.5M NaOH buffer: 0.3 g NaOH pellets. Fill to 15 mL with MilliQ water [56].

10x PBS Buffer: 0.8 g NaCl + 0.02 g KCl + 0.144 g Na_2HPO_4 + 0.027 g KH_2PO_4 + HCl (to adjust pH to 7.4). Fill to 10 mL with MilliQ water [78].

B

Optimized Pipetting Techniques for Spheroid Transfer

To achieve successful transfer of spheroids from the ULA-plate into the collagen I gel, the following protocol was used/utilized:

1. Take out as much old medium as possible from the well of the 96-well plate
2. Add 100 µL fresh medium
3. Vigorously pipet up and down alongside the well's perimeter twice to loosen the spheroids
4. Quickly take up 100 µL media, which will now contain spheroids, and transfer to an Eppendorf tube
5. Repeat steps 2-4 until acceptable amount of spheroids have been transferred
6. Repeat steps 1-5 for each well
7. Wait approximately 5 min. for the spheroids to settle at the bottom of the Eppendorf tube

Due to 20 spheroids being necessary per gel condition, and 160 spheroids being made in total, 1/8 of the spheroids need to be transferred to the gel (per condition). For convenience and easier pipetting, 50 µL medium containing spheroids needs to be transferred. Therefore the following steps were required:

8. Carefully take out media, without disturbing the spheroids, until 400 µL is left
9. Vigorously pipet up and down to loosen the spheroids from the clump they formed at the bottom of the Eppendorf tube
10. Quickly take up 50 µL (1/8 of 400 µL) medium containing spheroids. This will contain approximately 20 spheroids (1/8 of the total of 160 spheroids)
11. Immediately transfer to gel and pipet up and down a few to times to ensure mixing

C

CellProfiler Segmentation

Image analysis for this study was performed using CellProfiler 5.0 (Broad Institute), an open-source software designed for high-throughput biological image analysis. A custom pipeline was used to systematically process the acquired images, including preprocessing, segmentation, and measurement extraction. The pipeline comprised 23 modules, executed sequentially to ensure consistent and reproducible results.

Below, a detailed description of the key steps and settings of the pipeline is provided.

C.1. Pipeline Description

C.1.1. Images Module

- Purpose: Loads the images to be analyzed.
- Function: Defines the type of images (like .tiff, .png, etc.) and filters them by file name or metadata.
- Used in this study: Representing sequential time-lapse frames, Input1 and Input2 were both loaded. These datasets were identical in content, except that Input1 spanned timepoints t = 0 to t = 23, while Input2 covered t = 1 to t = 24. This one-frame offset allowed for direct frame-to-frame subtraction to analyze temporal changes.

C.1.2. Metadata Module

- Purpose: Extracts metadata from images, like experimental conditions, acquisition settings, or timepoints.
- Function: Take information from file names, paths, or external files for grouping or further analysis.
- Used in this study: No metadata extraction

C.1.3. NamesAndTypes Module

- Purpose: Assigns roles to the images (identifying images as nuclei, cytoplasm, etc.).
- Function: Links images to specific channels (DAPI, GFP, etc.) and defines relationships between images.
- Used in this study: 2 make-a-directory rules. The first selects input1 and the second selects input2. These directories can later be compared to each other

C.1.4. Groups Module

- Purpose: Groups images based on metadata (e.g., by well, timepoint, or experimental condition).
- Function: Ensures related images are analyzed together in the correct order.
- Used in this study: No grouping images

C.1.5. ImageMath Module

- Purpose: Perform initial image processing by mathematically subtracting input1 and input2, creating Stack3

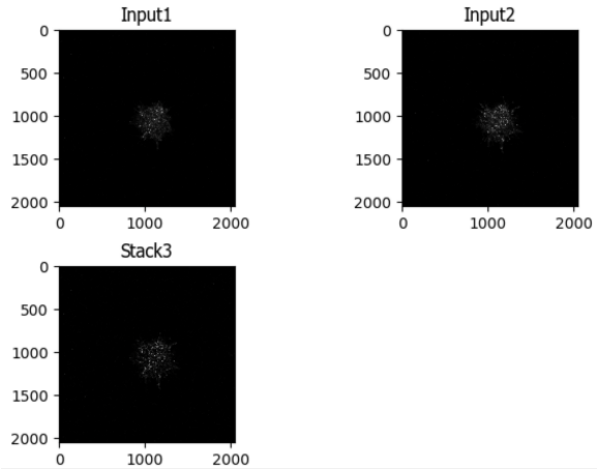

Figure C.1: Step 5 in the pipeline. ImageMath

C.1.6. ReduceNoise Module

- Remove or reduce image noise while preserving important structural details like edges. This improves the quality of the image for more accurate downstream analysis (object identification or segmentation)

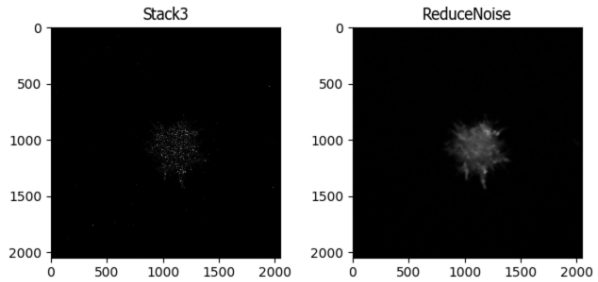

Figure C.2: Step 6 in the pipeline. ReduceNoise

C.1.7. GaussianFilter Module

- Smoothing the image using a Gaussian kernel, more aggressive than median filtering.
- Sigma (standard deviation) controls the amount of blur: Low sigma → less blur (fine detail preserved) High sigma → more blur (smoother image)

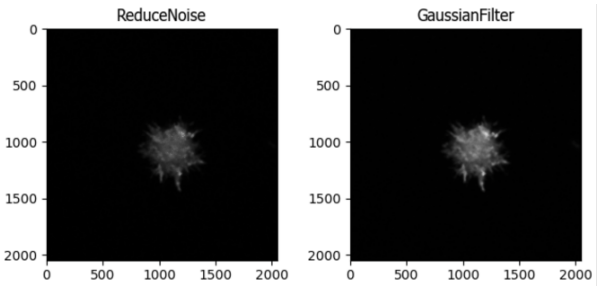

Figure C.3: Step 7 in the pipeline. GaussianFilter

C.1.8. Smooth Module

- The Smooth module allows you to apply different types of smoothing (blurring) or enhancement filters to an image.
- These operations can reduce random noise, enhance or suppress specific features (small spots, edges), prepare the image for more accurate segmentation or thresholding

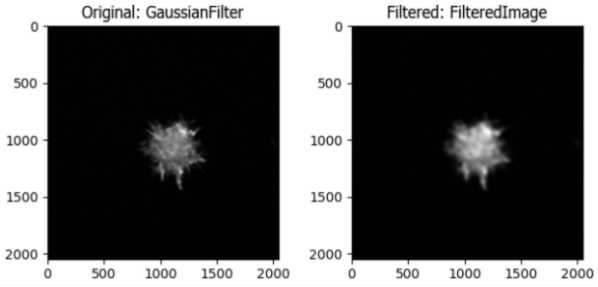

Figure C.4: Step 8 in the pipeline. Smooth

C.1.9. SaveImages

- The resulting filtered image is saved (’FilteredImage’)

C.1.10. IdentifyPrimaryObjects Module

- Purpose: Identify the primary objects (cells, spheroids) in the image based on the processed data.
- Use the previously saved images (’FilteredImage’)
- Rename the output (’Obj’)

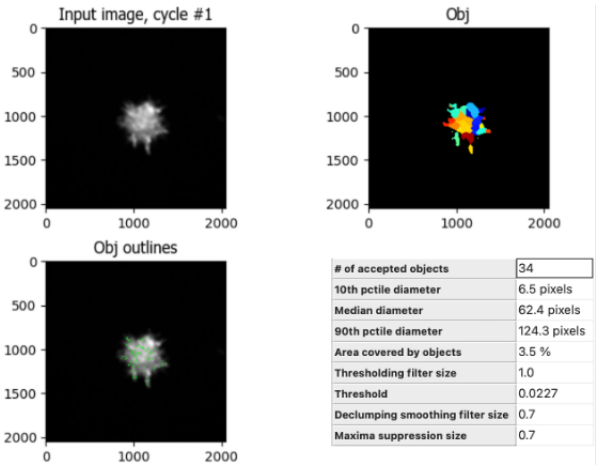

Figure C.5: Step 10 in the pipeline. IdentifyPrimaryObjects

C.1.11. ExpandOrShrinkObjects Module

- Purpose: Adjust the size of the segmented objects to account for missed edges or to simplify the shape.
- Use ’Obj’
- Rename the Output ’ObjExp’

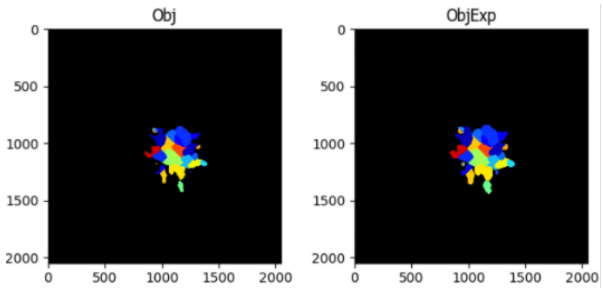

Figure C.6: Step 11 in the pipeline. ExpandOrShrinkObjects

C.1.12. SplitOrMergeObjects Module

- Purpose: Split incorrectly merged objects or merge objects that are too fragmented.
- Use 'ObjExp'
- Rename the Output 'ObjExpMer'

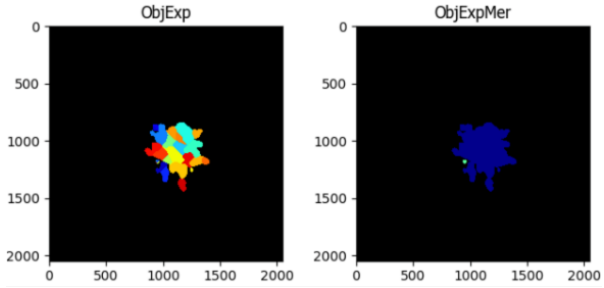

Figure C.7: Step 12 in the pipeline. SplitOrMergeObjects

C.1.13. FillObjects Module

- Purpose: Fill internal gaps or holes within segmented objects to make them solid.
- Why Here: Guarantees that measurements (like area or shape) are based on complete objects, reducing the risk of inaccurate data.
- Use 'ObjExpMer'
- Rename the Output 'ObjExpMerFil'

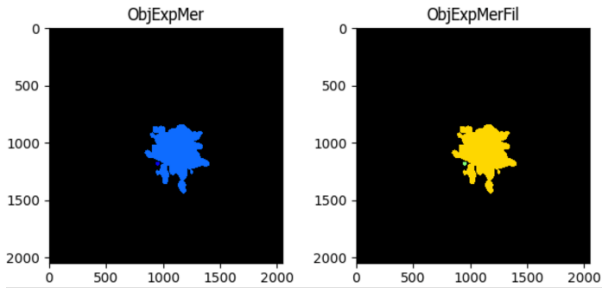

Figure C.8: Step 13 in the pipeline. FillObjects

C.1.14. MeasureObjectsSizeShape Module

- Purpose: Calculate size and shape properties (area, perimeter, eccentricity, etc.) of the segmented objects, including the mean, median, and standard deviation
- Use 'ObjExpMerFil'

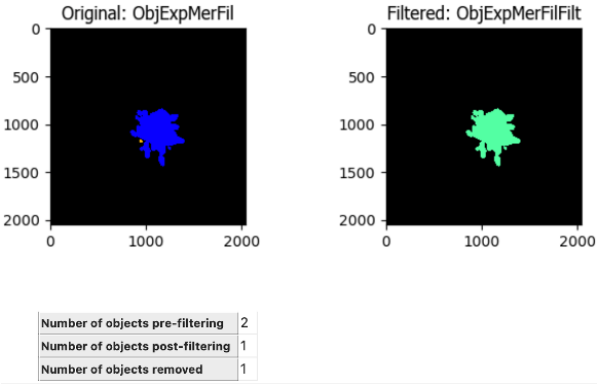

Figure C.9: Step 15 in the pipeline. FilterObjects

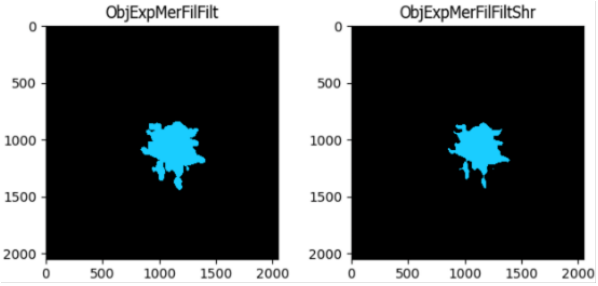

Figure C.10: Step 16 in the pipeline. ExpandOrShrinkObjetcs

C.1.15. FilterObjects Module

- Purpose: Filter out objects based on predefined criteria (size, shape, intensity, etc.)
- Still use ‘ObjExpMerFil’ because there was no new Output name given in the previous step
- Rename the Output ’ObjExpMerFilFilt’

C.1.16. ExpandOrShrinkObjects Module

- Purpose: Again, expand or shrink the objects.
- Why: This second use of ExpandOrShrinkObjects allows further refinement, after measuring and filtering objects. It can help to adjust the boundaries more accurately based on the filtered objects.
- Use ’ObjExpMerFilFilt’
- Rename the Output ’ObjExpMerFilFiltShr’

C.1.17. MeasureObjectsSizeShape Module

- Purpose: Recalculate the size and shape metrics after the second round of boundary adjustments.
- Why: After modifying the objects, it’s important to measure their properties again to ensure accuracy and update measurements after the refinement steps.

C.1.18. CalculateMath Module

- The CalculateMath module in CellProfiler performs mathematical operations on images or measurement values. It is here used to calculate the major and the minor axislength for the Aspect Ratio.

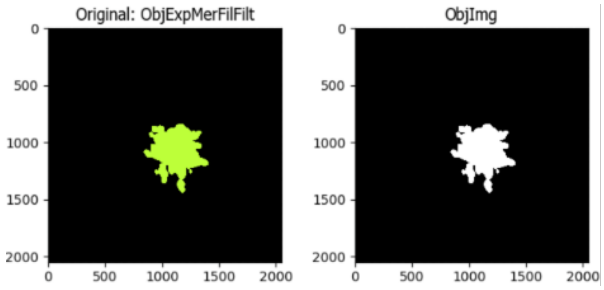

Figure C.11: Step 20 in the pipeline. ConvertObjectsToImage

C.1.19. ExportToSpreadsheet Module

- Purpose: Export the measurements of the objects (size, shape, etc.) to a spreadsheet for further analysis.
- Ensure that the Output location is set correctly
- Use ’comma delimiter’ for the .csv

C.1.20. ConvertObjectsToImage Module

- Purpose: Convert the final segmented objects into an image format (binary, grayscale, or label) for visualization or further processing.
- Use ’ObjExpMerFilFiltShr’
- Rename the Output ’ObjImg’

C.1.21. ImageMath Module

- Purpose: Perform another mathematical subtraction on the image
- Here ’ObjImg’ (the difference between input1 and input2 after all processing steps) and ’Stack3’ (the original absolute difference between input1 and input2) are subtracted
- Rename Output ’ObjImgMat’

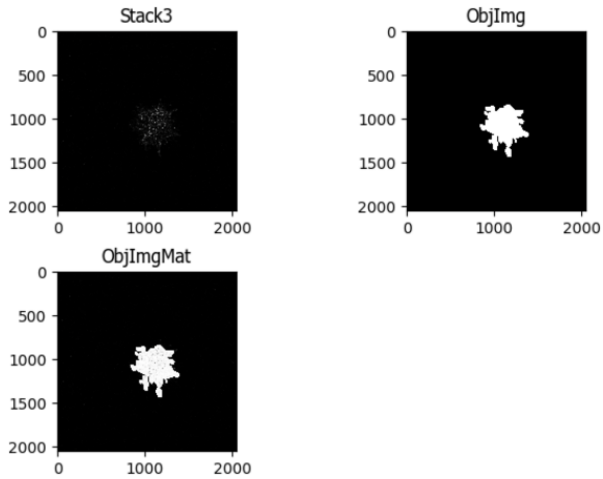

Figure C.12: Step 21 in the pipeline. ImageMath

C.1.22. ImageMath Module

- Purpose: Another round of image processing.

- Here ’ObjImgMat’ and ’Stack3’ are subtracted
- Rename Output ’Stack3Seg’

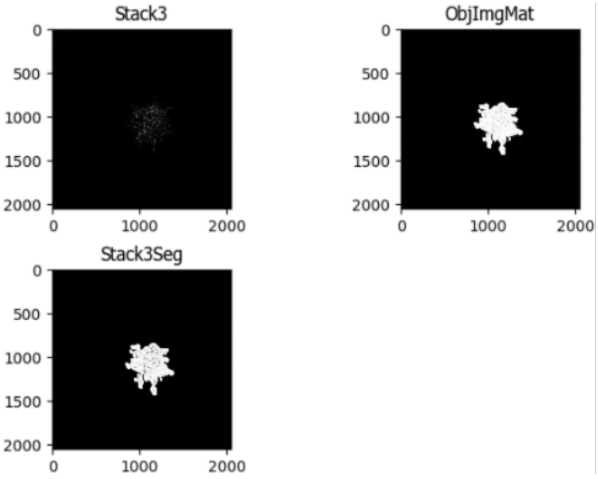

Figure C.13: Step 22 in the pipeline. ImageMath

C.1.23. SaveImages

- Purpose: Save the final processed images after all the operations.

C.2. Segmentation Images

An example of the CellProfiler segmentation is featured below (Figure C.14). Mono 4T1 spheroids in 1.5 mg/mL collagen gel is used.

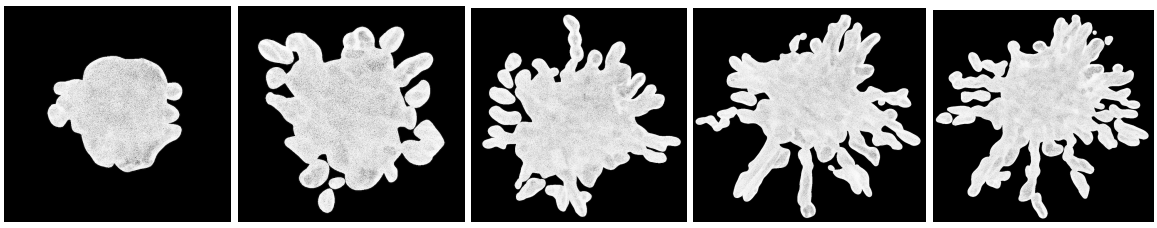

(a) t=0 **(b)** t=6h **(c)** t=12h **(d)** t=18h **(e)** t=24h

Figure C.14: CellProfiler pipeline example of mono 4T1 spheroids in 1.5 mg/mL rat tail collagen gel

D

Results Temporal Collagen Remodeling and Degradation

The way the three spheroid types affect the collagen matrix is described below.

D.1. Rat Tail Collagen Gels

In the 1.5 mg/mL rat tail collagen condition, mono 4T1 spheroids appear to impact the matrix most prominently (Figure D.1C). From t = 0, where the collagen signal is relatively low, to t = 24h, fluorescence intensity around the spheroid increases noticeably, suggesting an accumulation or realignment of collagen fibers. This pattern implies that mono 4T1 spheroids may attract and remodel the surrounding collagen. However, the presence of dark gaps in the matrix also points to local degradation, indicating that both remodeling and breakdown processes are occurring. Mono NIH3T3 spheroids also show signs of matrix remodeling, as fluorescence gradually increases over time (Figure D.1B). Unlike the 4T1 condition, there are no distinct dark gaps, suggesting that NIH3T3 cells primarily induce collagen remodeling without significant degradation. In contrast, heterospheroids seem to primarily degrade the collagen matrix. The highest fluorescence signal is observed at t = 0, but by t = 12h, a pronounced dark void appears where the spheroid was initially located (Figure D.1A), suggesting extensive local matrix degradation rather than remodeling.

In stark contrast to the 1.5 mg/mL rat tail collagen, the 4.0 mg/mL rat tail collagen condition shows no apparent signs of collagen remodeling, as no increase in fluorescence is observed over time. Instead, both mono 4T1 spheroids (Figure D.2C) and heterospheroids (Figure D.2A) appear to primarily degrade the matrix, as indicated by the emergence of dark voids around the spheroids.

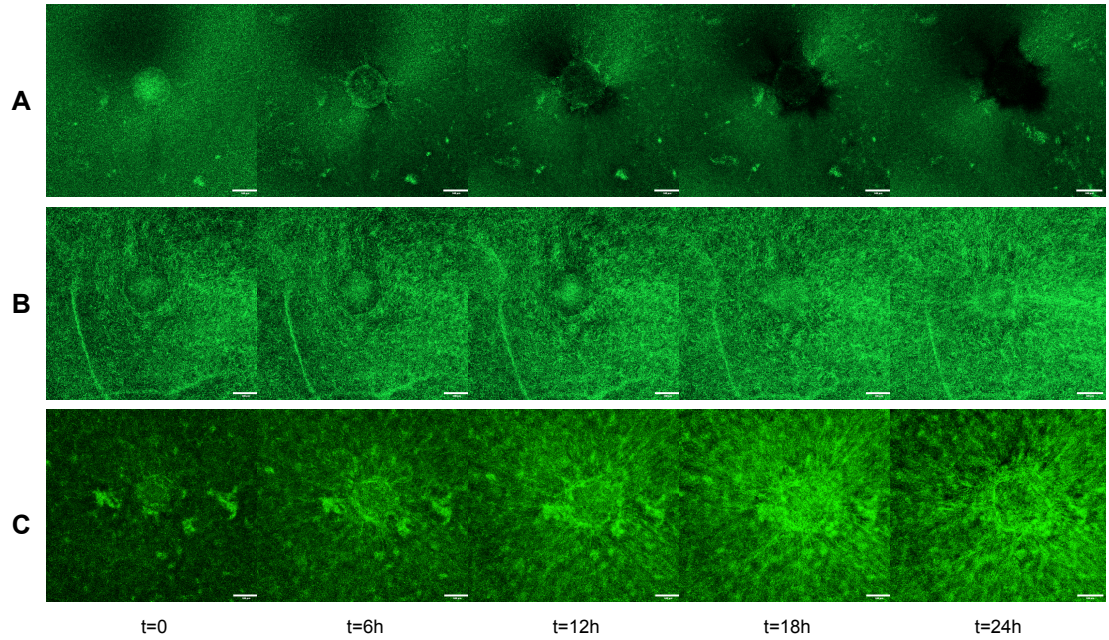

Figure D.1: Temporal progression of 1.5 mg/mL rat tail collagen gel. x-axis illustrates time in hours. A) 1:1 heterospheroids. B) Mono NIH3T3 spheroids. C) Mono 4T1 spheroids. Scale bars correspond to 100 µm.

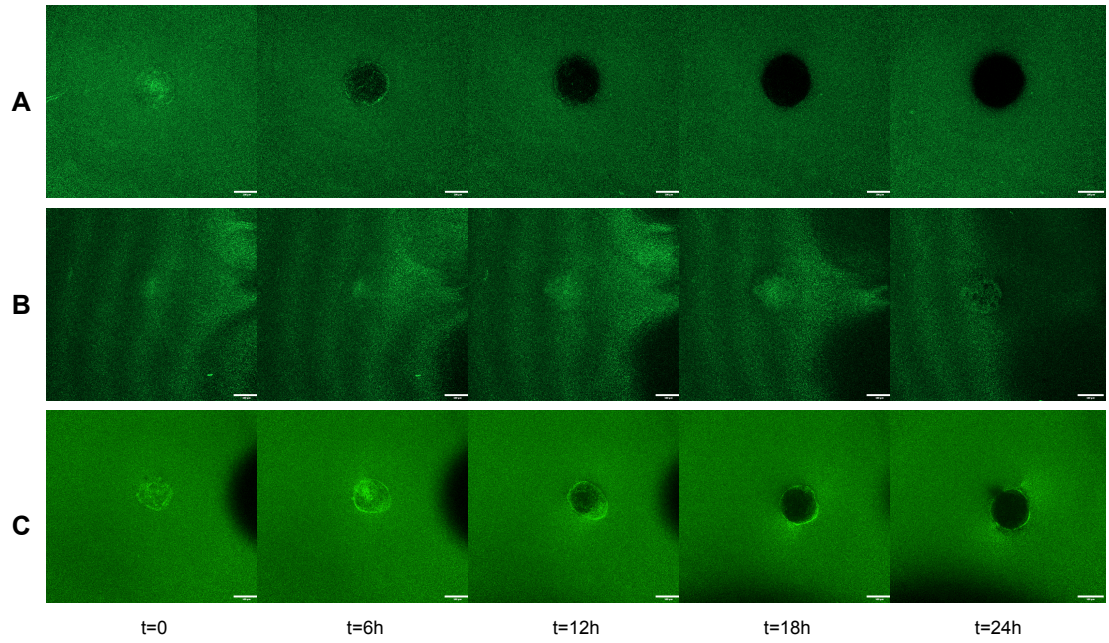

Figure D.2: Temporal progression of 4.0 mg/mL rat tail collagen gel. x-axis illustrates time in hours. A) 1:1 heterospheroids. B) Mono NIH3T3 spheroids. C) Mono 4T1 spheroids. Scale bars correspond to 100 µm.

D.2. Bovine Collagen Gels

In the 2.4 mg/mL bovine collagen, mono 4T1 spheroids appear to remodel the matrix most actively, as indicated by a clear increase in fluorescence over time (Figure D.3C). In contrast, mono NIH3T3 spheroids show little to no effect on the collagen structure, with no notable changes in fluorescence (Figure D.3B). The heterospheroids, similar to those in the 1.5 mg/mL rat tail collagen, seem to primarily degrade the matrix without evidence of remodeling, as suggested by the development of dark voids over time (Figure D.3A).

Observations in the 3.3 mg/mL bovine collagen closely mirror those seen at 2.4 mg/mL. Once again,

mono 4T1 spheroids appear to remodel the matrix most prominently, as evidenced by increasing fluorescence over time (Figure D.4C). Mono NIH3T3 spheroids show little to no impact on the collagen structure, with no apparent fluorescence change (Figure D.4B). In contrast, heterospheroids lead to the formation of a dark void over time (t = 18h), indicating matrix degradation without remodeling (Figure D.4A).

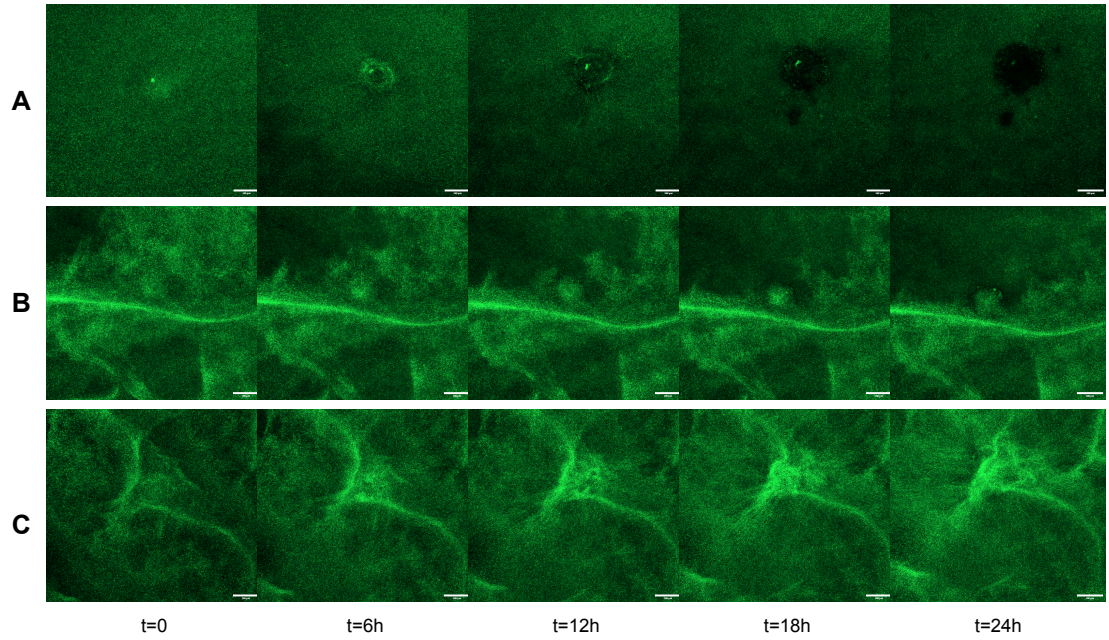

Figure D.3: Temporal progression 2.4 mg/mL bovine collagen gel. x-axis illustrates time in hours. A) 1:1 heterospheroids. B) Mono NIH3T3 spheroids. C) Mono 4T1 spheroids. Scale bars correspond to 100 µm.

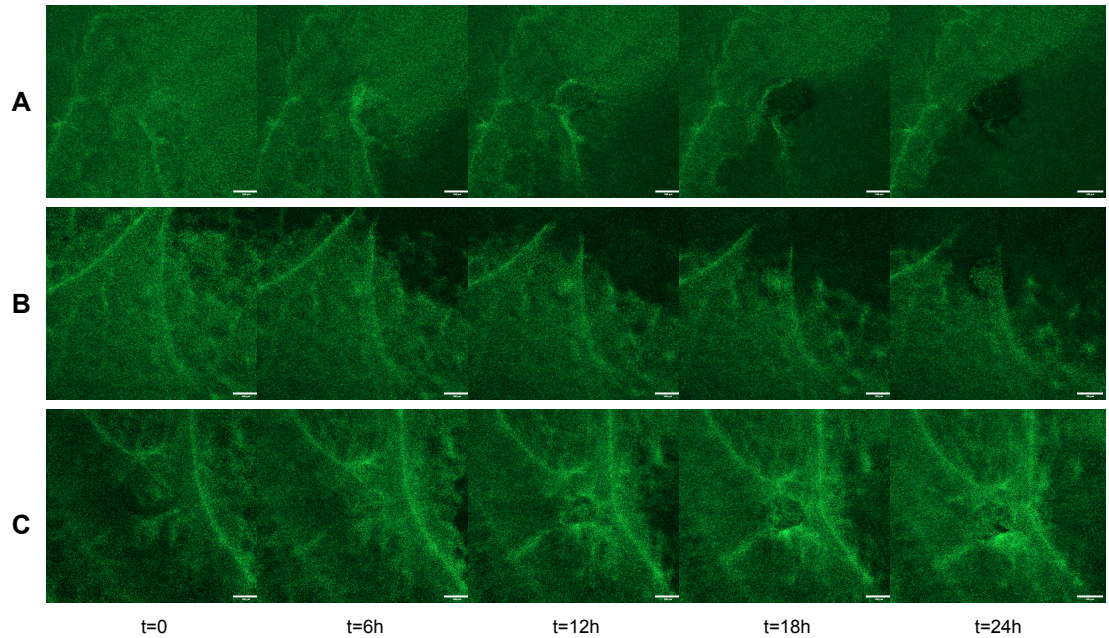

Figure D.4: Temporal progression of 3.3 mg/mL bovine collagen gel. x-axis illustrates time in hours. A) 1:1 heterospheroids. B) Mono NIH3T3 spheroids. C) Mono 4T1 spheroids. Scale bars correspond to 100 µm.

Overall, collagen remodeling and degradation varied by cell type and gel concentration. Mono 4T1 spheroids consistently showed the strongest remodeling activity, particularly in 1.5 mg/mL rat tail and 2.4–3.3 mg/mL bovine collagen, as evidenced by increased fluorescence over time. In the 1.5 mg/mL

rat tail condition, this remodeling was accompanied by some local matrix degradation, indicated by dark gaps. Mono NIH3T3 spheroids induced modest collagen remodeling without degradation, while heterospheroids primarily degraded the matrix across all conditions, forming dark voids and showing little to no remodeling. In the denser 4.0 mg/mL rat tail collagen, no remodeling was observed; both mono 4T1 and heterospheroids showed only degradation. These patterns highlight the distinct matrix interactions of each spheroid type and the influence of collagen concentration and source on remodeling dynamics.

E

Bubble Size Detection and Analysis

The detection and quantification of bubbles within collagen gel images were performed using a custom Python-based image analysis pipeline developed by Iain Muntz. The following sections provide an explanation of the method, alongside the corresponding code, followed by the presentation of experimental results in the form of processed images.

E.1. Bubble Script

As a preprocessing step, images were first binarized using Otsu's B & W thresholding method, followed by conversion to RGB format to ensure compatibility with downstream analysis tools. No brightness adjustments were applied, preserving the original pixel intensity distributions. Next, grayscale conversion and inversion were performed to enhance contrast, after which a Difference of Gaussians (DoG) filter was applied to emphasize features within a specific size range (bubble-like structures). This was followed by total variation denoising to suppress high-frequency noise. An adaptive local threshold was then used to generate a binary mask highlighting potential bubble regions. From this binary mask, a Euclidean Distance Map (EDM) was computed and smoothed with a Gaussian filter (σ = 7 pixels) to produce a continuous representation of local distances from object boundaries. Local maxima within the EDM, identified using an 8-connected neighborhood criterion, were assumed to correspond to bubble centers, with the peak values representing the radii of the largest inscribed circles. A pore count was obtained as well by counting all the peaks. Furthermore, the radii were doubled and converted to diameters in micrometers using a pixel-to-micron scale factor (0.1036 µm/pixel). The resulting distribution of bubble diameters was visualized using a histogram, and a Gaussian distribution was fit to the data to extract the mean and standard deviation, providing a quantitative assessment of the gel's porosity. Figure E.1 provides an overview of the code's workflow.

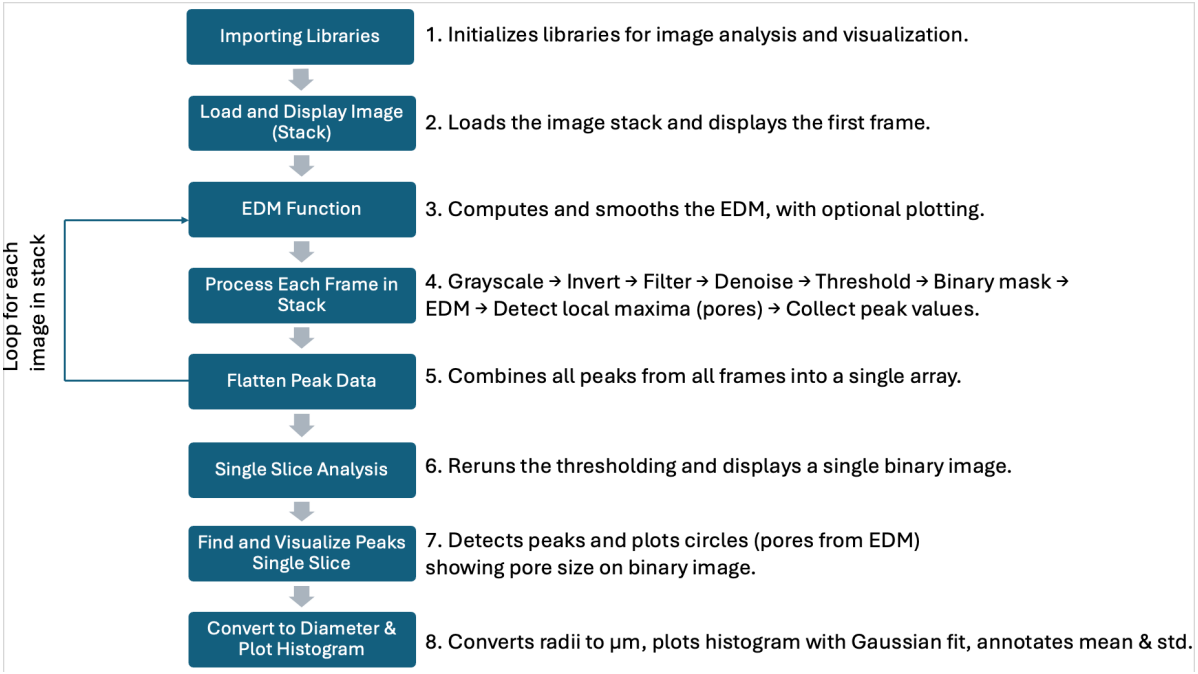

Figure E.1: Workflow diagram illustrating the key steps of the bubble detection code, from image preprocessing to pore identification and analysis.

The full code is shown below:

```
# Importing the required libraries
import numpy as np                                          # For numerical operations
import matplotlib.pyplot as pl                              # For visualizing images and
    ↪ histograms
from PIL import Image, ImageSequence, ImageOps              # For image processing, opening,
    ↪ inverting, and iterating over image sequences (stacks)
import os
import sys
from scipy import signal                                    # Contains image filtering,
    ↪ Euclidean Distance Map (EDM), and statistical functions.
import scipy
from skimage import filters                                 # Contains image thresholding and
    ↪ filtering functions.
from skimage.restoration import (denoise_tv_chambolle, estimate_sigma)   #Used for image
    ↪ denoising and noise estimation.
import scipy.stats as ss

# Loading and Displaying the selected image

scale = 0.1035803 #9.6543 #6.7                                          # Conversion
    ↪ factor from pixels to micrometers
a = Image.open('//Volumes/Expansion/Ayesha_MEP/Python/Porosity experiments/t=24_bubblescript/
    ↪ Rat/3A_Hetero_t=72/col_1.5_40x.tif')
#('//Volumes/Expansion/Ayesha_MEP/Python/t=24_bubblescript/Bovine/4B_MonoFibro/MonoFibro_2.4
    ↪ _40x-2-test-1-rgb.tif')  #NIET BRIGHTNESS!!! Otsu B&W en daarna rgb          # Where
    ↪ does the directory go????
length = sum(1 for _ in ImageSequence.Iterator(a))          # Determines the number of frames
    ↪ in the image sequence (if it's a stack).
pl.imshow(a)                                                # Displays the image.

#calculate the Euclidean Distance Map (EDM) and smooth it with a gaussian kernel of width (
    ↪ standard dev of gaussian) 3 pixels
def edmCalc(image, plots = False):
    edm = scipy.ndimage.morphology.distance_transform_edt(image)
    edm = scipy.ndimage.gaussian_filter(edm,5) #nice met 5 #werkt met edm,10 #original edm,3
    if plots:
        pl.imshow(edm)
        pl.colorbar()
```

```
    return edm

#for stack
fullPeaks = []
for i in range(length):
    frame = ImageSequence.Iterator(a)[i].convert('L') #convert to grayscale first
    c = np.asarray(ImageOps.invert(frame))
    #c = np.asarray(ImageOps.invert(ImageSequence.Iterator(a)[i]).convert('L'))
    #bandpass filter using difference of gaussians method
    filteredImage = filters.difference_of_gaussians(c, 2,20) #werkt met 2,50 #3,30
    filteredImage2 = denoise_tv_chambolle(filteredImage, weight = 0.1) #c, weight 0.1 #nice met 1.0
    block_size = estimate_sigma(c)*21.

    #adaptive threshold
    threshOffset = -0.05
    local_threshold_in = filters.threshold_local(filteredImage2, block_size, offset=threshOffset)
    binary_adaptive_filt = np.asarray(filteredImage2 > local_threshold_in).astype('uint8')

    b = np.asarray(binary_adaptive_filt)

    edm = edmCalc(b)
    #find the positions of all peaks of the EDM where a peak is defined by being greater than its 8 neighbours
    peakPositions = find2dpeaks(edm)
    #peak values in EDM is equal to the circle that corresponds to that bubble
    edmPeaks = edm[peakPositions.T[0],peakPositions.T[1]]
    fullPeaks.append(edmPeaks)
    print(f"Frame {i+1}: {len(edmPeaks)} pores detected")
allPeaks = np.concatenate(fullPeaks).ravel()
print(f"Total number of pores detected in stack: {len(allPeaks)}")
#print(allPeaks)
#print(fullPeaks)

#for slice
#run filtering
#c = np.asarray(ImageOps.invert(a).convert('L'))

#bandpass filter using difference of gaussians method
#filteredImage = denoise_tv_chambolle(c, weight = 0.1)
block_size = estimate_sigma(c)*21.
threshOffset = -0.05
local_threshold_in = filters.threshold_local(filteredImage2, block_size, offset=threshOffset)
binary_adaptive_filt = np.asarray(filteredImage2 > local_threshold_in).astype('uint8')

b = np.asarray(binary_adaptive_filt)

pl.imshow(b, cmap = 'gray')

#find peaks in the euclidean distance map, ONLY FOR SLICE

edm = edmCalc(b, plots = False)
#find the positions of all peaks of the EDM where a peak is defined by being greater than its 8 neighbours
peakPositions = find2dpeaks(edm)
#peak values in EDM is equal to the circle that corresponds to that bubble
edmPeaks = edm[peakPositions.T[0],peakPositions.T[1]]
allPeaks = edmPeaks

#shows the example for the last image in the stack (can be fairly easily edited to be any image)
fig, ax = pl.subplots(figsize = (10,10))
ax.imshow(b, cmap = 'gray') #a,cmap
ax.plot(peakPositions.T[1], peakPositions.T[0], ls = 'None', marker = 'x', color = 'r')
for i in range(len(edmPeaks)):
    ax.add_patch(pl.Circle((peakPositions.T[1][i], peakPositions.T[0][i]), edmPeaks[i], fill = False, color = 'r'))

# Convert EDM peaks to diameters (µm)
scale = 0.1035803  # µm/pixel (from your ImageJ metadata)
```

```
diameters = 2 * allPeaks * scale

# Plot histogram
fig = pl.figure(1, figsize=(15, 10))
pl.hist(diameters, bins=20, density=True, alpha=0.6)

# Calculate mean/std for Gaussian fit
mean = np.mean(diameters)
std = np.std(diameters)

# Generate and plot the Gaussian curve
x = np.linspace(np.min(diameters), np.max(diameters), 100)
pl.plot(x, ss.norm.pdf(x, mean, std), '-', linewidth=3, label='Normal Fit')

# Add text and labels
pl.text(0.5, 0.7, f'Mean = {mean:.2f} µm\nstd = {std:.2f} µm', fontsize=30, transform=pl.gca
    ↪ ().transAxes)
pl.xlabel(r'Diameter ($\mu$m)', fontsize=32)
pl.ylabel('Probability Density', fontsize=24)
pl.xticks(fontsize=26)
pl.yticks(fontsize=26)
pl.legend(fontsize=20)
pl.grid(True, linestyle='--', alpha=0.3)
pl.show()


print(f"Mean diameter: {mean:.2f} µm")
print(f"Std deviation: {std:.2f} µm")
```

E.2. Pore Size Distribution and Count Across Collagen Conditions

The pore size distribution in 1.5 mg/mL rat tail collagen (Figure E.2) shows that heterospheroids exhibited a mean pore diameter of 0.83 µm, mono NIH3T3 spheroids had a mean of 0.78 µm, and mono 4T1 spheroids displayed a mean of 0.86 µm. All three conditions exhibited comparable pore sizes. Interestingly, mono 4T1 spheroids showed the largest pores, followed by heterospheroids, suggesting that in this gel concentration, heterospheroids may behave more similarly to mono 4T1 spheroids. This trend may reflect the remodeling activity of the aggressive 4T1 cells within the heterospheroids.

In 4.0 mg/mL rat tail collagen (Figure E.3), a notable decrease in pore size is observed relative to the 1.5 mg/mL condition. Heterospheroids exhibited a mean diameter of 0.47 µm, mono NIH3T3 spheroids 0.42 µm, and mono 4T1 spheroids 0.44 µm. The overall similarity in pore size across all conditions suggests minimal matrix remodeling at this higher collagen density, likely due to limited cellular invasion or matrix degradation.

The 2.4 mg/mL bovine collagen condition (Figure E.4) resulted in pore sizes closer to those in the 1.5 mg/mL rat tail collagen. Heterospheroids showed a mean diameter of 1.07 µm, mono NIH3T3 spheroids 1.24 µm, and mono 4T1 spheroids 0.62 µm. In this case, heterospheroids resembled mono NIH3T3 spheroids more closely, indicating that fibroblasts may dominate the matrix remodeling response in this gel formulation.

A similar pattern was seen in the 3.3 mg/mL bovine collagen condition (Figure E.5), where pore sizes were again comparable to the 2.4 mg/mL and 1.5 mg/mL gels. Mean pore diameters were 0.90 µm for heterospheroids, 0.94 µm for mono NIH3T3 spheroids, and 0.53 µm for mono 4T1 spheroids. As in the 2.4 mg/mL condition, heterospheroids exhibited pore sizes more similar to those of the mono NIH3T3 spheroids, further suggesting a fibroblast-dominated remodeling pattern under these conditions.

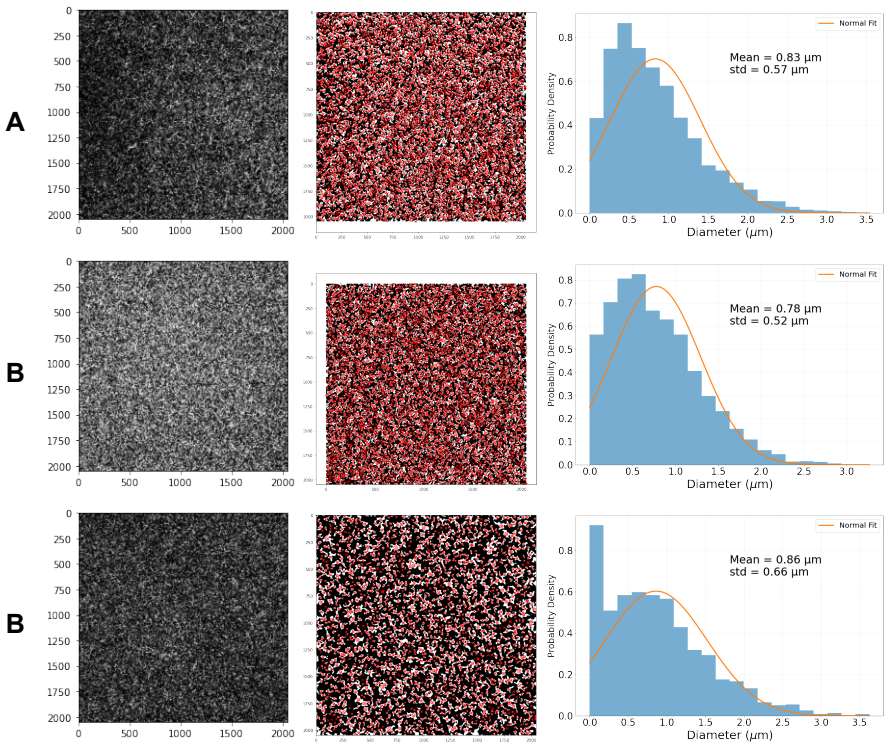

Figure E.2: Pore size distribution in 1.5 mg/mL rat tail collagen. A) Heterospheroids exhibited a mean pore diameter of 0.83 µm. B) Mono NIH3T3 spheroids showed a mean diameter of 0.78 µm. C) Mono 4T1 spheroids had a mean diameter of 0.86 µm.

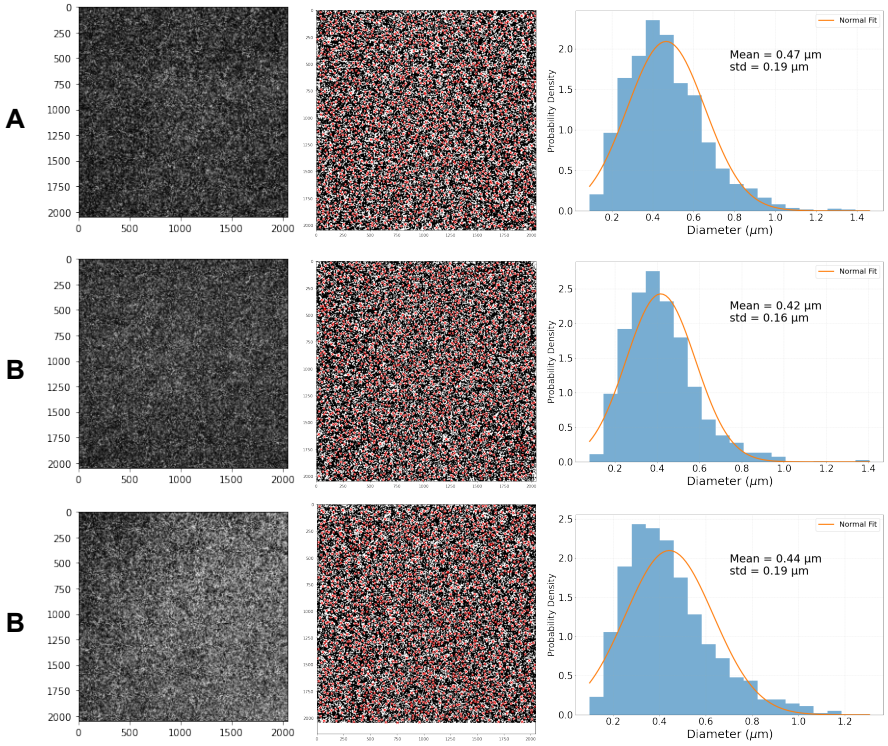

Figure E.3: Pore size distribution in 4.0 mg/mL rat tail collagen. A) Heterospheroids exhibited a mean pore diameter of 0.47 µm. B) Mono NIH3T3 spheroids showed a mean diameter of 0.42 µm. C) Mono 4T1 spheroids had a mean diameter of 0.44 µm.

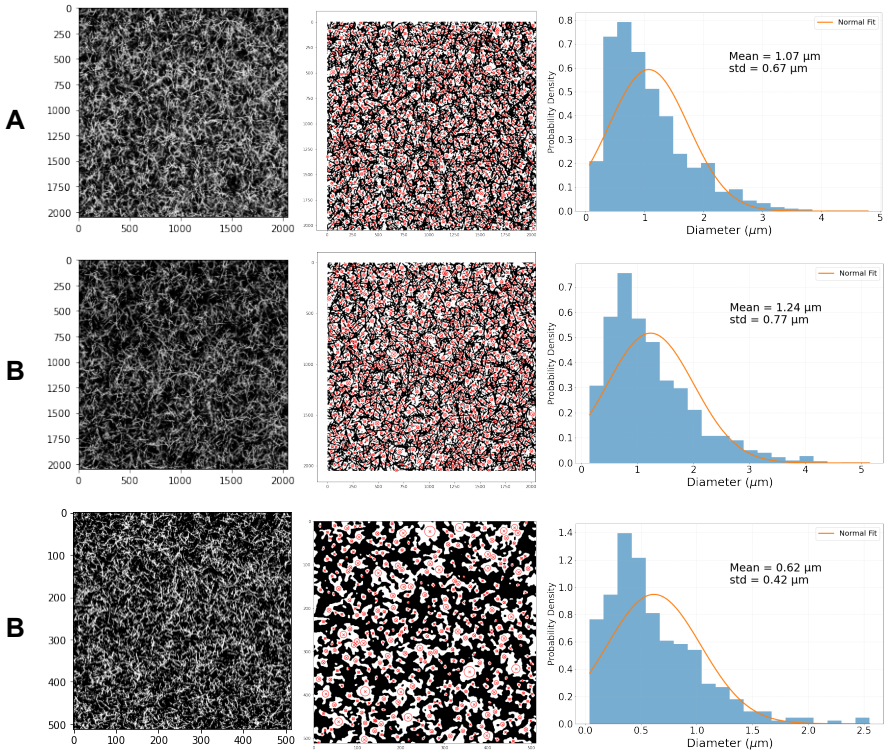

Figure E.4: Pore size distribution in 2.4 mg/mL bovine collagen. A) Heterospheroids exhibited a mean pore diameter of 1.07 µm. B) Mono NIH3T3 spheroids showed a mean diameter of 1.24 µm. C) Mono 4T1 spheroids had a mean diameter of 0.62 µm.

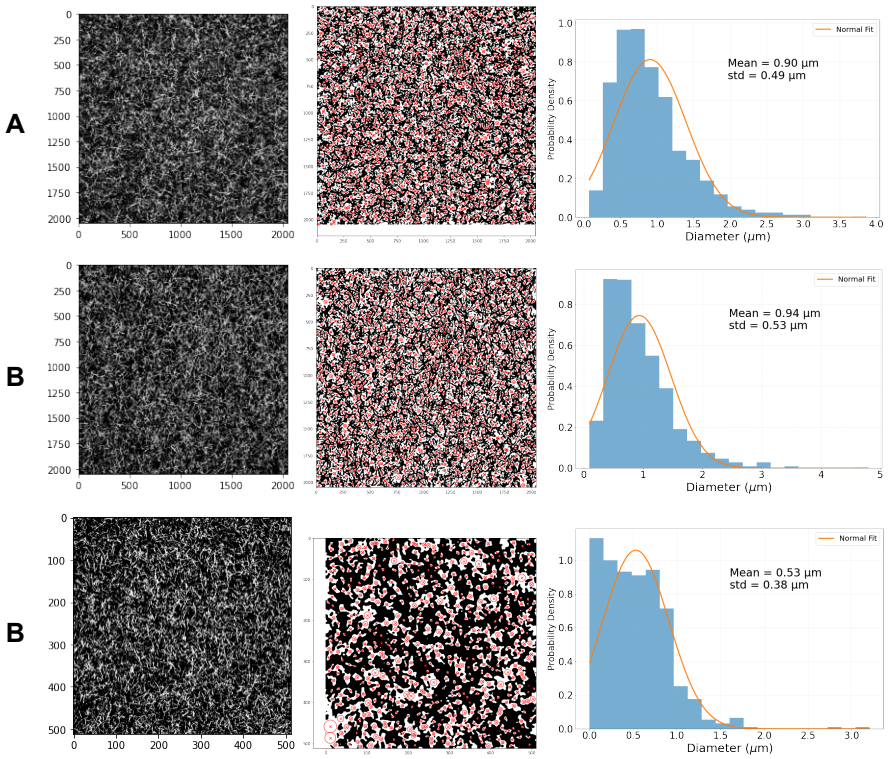

Figure E.5: Pore size distribution in 3.3 mg/mL bovine collagen. A) Heterospheroids exhibited a mean pore diameter of 0.90 µm. B) Mono NIH3T3 spheroids showed a mean diameter of 0.94 µm. C) Mono 4T1 spheroids had a mean diameter of 0.53 µm.

The total number of pores identified across conditions (Table E.1) reveals clear trends in matrix porosity as influenced by collagen concentration, source, and spheroid composition. In 1.5 mg/mL rat tail collagen, both heterospheroids (3681 pores) and mono NIH3T3 spheroids (3762 pores) showed substantially higher pore counts than mono 4T1 spheroids (1936 pores). Increasing the collagen concentration to 4.0 mg/mL resulted in a significant reduction in pore count for heterospheroids (1592 pores) and mono 4T1 spheroids (1131 pores). Surprisingly, mono NIH3T3 spheroids in this condition showed the highest pore count (4959 pores), potentially indicating enhanced fibroblast activity or imaging/segmentation errors.

In bovine collagen, the 2.4 mg/mL condition yielded the highest heterospheroid pore count (3314 pores), followed by mono NIH3T3 (1198) and mono 4T1 (230). This pattern persisted in the 3.3 mg/mL gels, where heterospheroids (1340 pores) and mono NIH3T3 spheroids (1361) again exceeded mono 4T1 spheroids (569). Notably, mono 4T1 spheroids consistently exhibited the lowest pore counts across all conditions, reinforcing the idea that 4T1 cells alone may degrade the matrix.

In contrast to the pore size, the pore count of the 1.5 mg/mL, 2.4 mg/mL and 3.3 mg/mL gels are not similar.

Table E.1: Total pores per source, per concentration, per spheroid type

Collagen Source	Collagen Concentration (mg/mL)	Spheroid Type	Total Pores
Rat tail	1.5	Hetero	3681
		Mono NIH3T3	3762
		Mono 4T1	1936
	4.0	Hetero	1592
		Mono NIH3T3	4959
		Mono 4T1	1131
Bovine	2.4	Hetero	3314
		Mono NIH3T3	1198
		Mono 4T1	230
	3.3	Hetero	1340
		Mono NIH3T3	1361
		Mono 4T1	569

F

Rat Tail Collagen Decline

Collagen gel experiments initially used rat tail collagen. However, as shown in Figure F.1, the collagen quality gradually deteriorated over time. In the first experiment (28-02-2025), fibers are clearly visible in the 1.5 mg/mL gel. By the third experiment (07-03-2025), a noticeable reduction in fiber presence is observed. The 4.0 mg/mL gel showed issues from the start, likely due to the challenges of mixing such a viscous solution. This is supported by the appearance of collagen blobs in samples from 28-02-2025 and 05-03-2025.

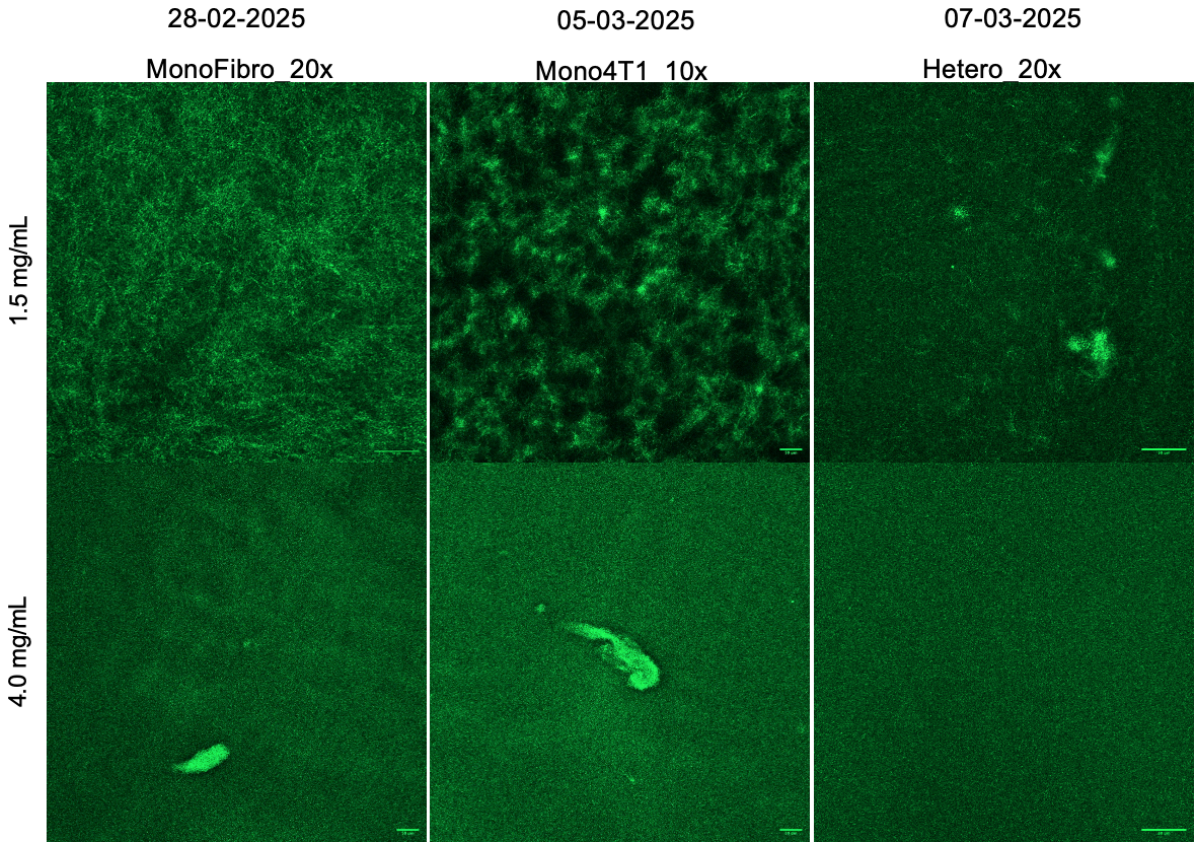

Figure F.1: Gradual decline in collagen gel quality, as evident by the delcining amount of fibers. Scale bars correspond to 50 µm.

A repeat experiment was conducted using heterospheroids. As shown in Figure F.2, the 1.5 mg/mL gel could no longer physically retain the spheroids, leading to rapid migration beyond the field of view,

contrasting with earlier results obtained before the collagen quality declined (Figure 4.2). Additionally, Figure F.3 shows spheroid invasion at t=24h in the 4.0 mg/mL gel condition, which was not observed prior to the decline in collagen quality (Figure 4.3). These findings further suggest that the matrix had lost its intended density and structural integrity.

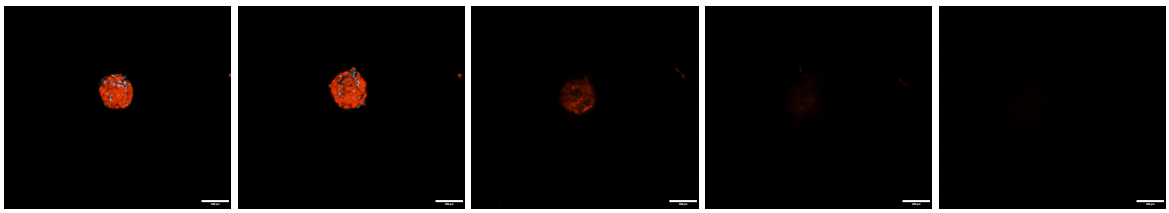

(a) t=0 **(b)** t=6h **(c)** t=12h **(d)** t=18h **(e)** t=24h

Figure F.2: Temporal progression of Mono4T1 in 1.5 mg/mL reduced quality collagen gel

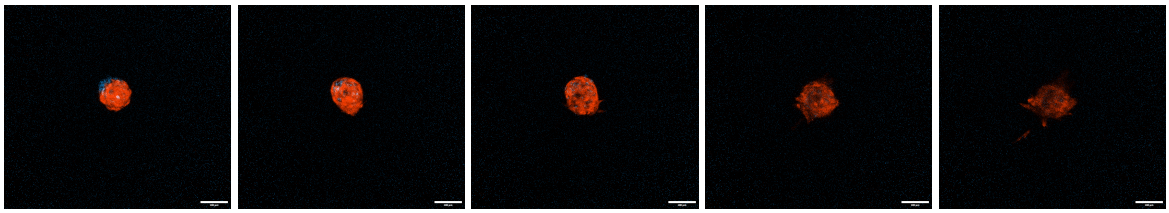

(a) t=0 **(b)** t=6h **(c)** t=12h **(d)** t=18h **(e)** t=24h

Figure F.3: Temporal progression of Mono4T1 in 4.0 mg/mL reduced quality collagen gel

To assess the initial quality of the collagen, a gel-only experiment was conducted prior to cell experiments (Figure F.4, 26-02-2025). Following the observed decline in collagen quality during subsequent experiments (Figure F.1), a second gel-only test was performed on 25-03-2025. As shown in Figure F.4, a clear reduction in visible fibers was evident. Furthermore, the visible fibers no longer formed a network as seen previously; instead, they appeared short and stubby.

Multiple parameters were modified in an attempt to resolve the issue, including the use of freshly-made buffers, an updated protocol (Chapter 3, Protocol II), new 10x DMEM, new batches of rat tail collagen, and vortexing during preparation, but none of these changes restored the original gel quality.

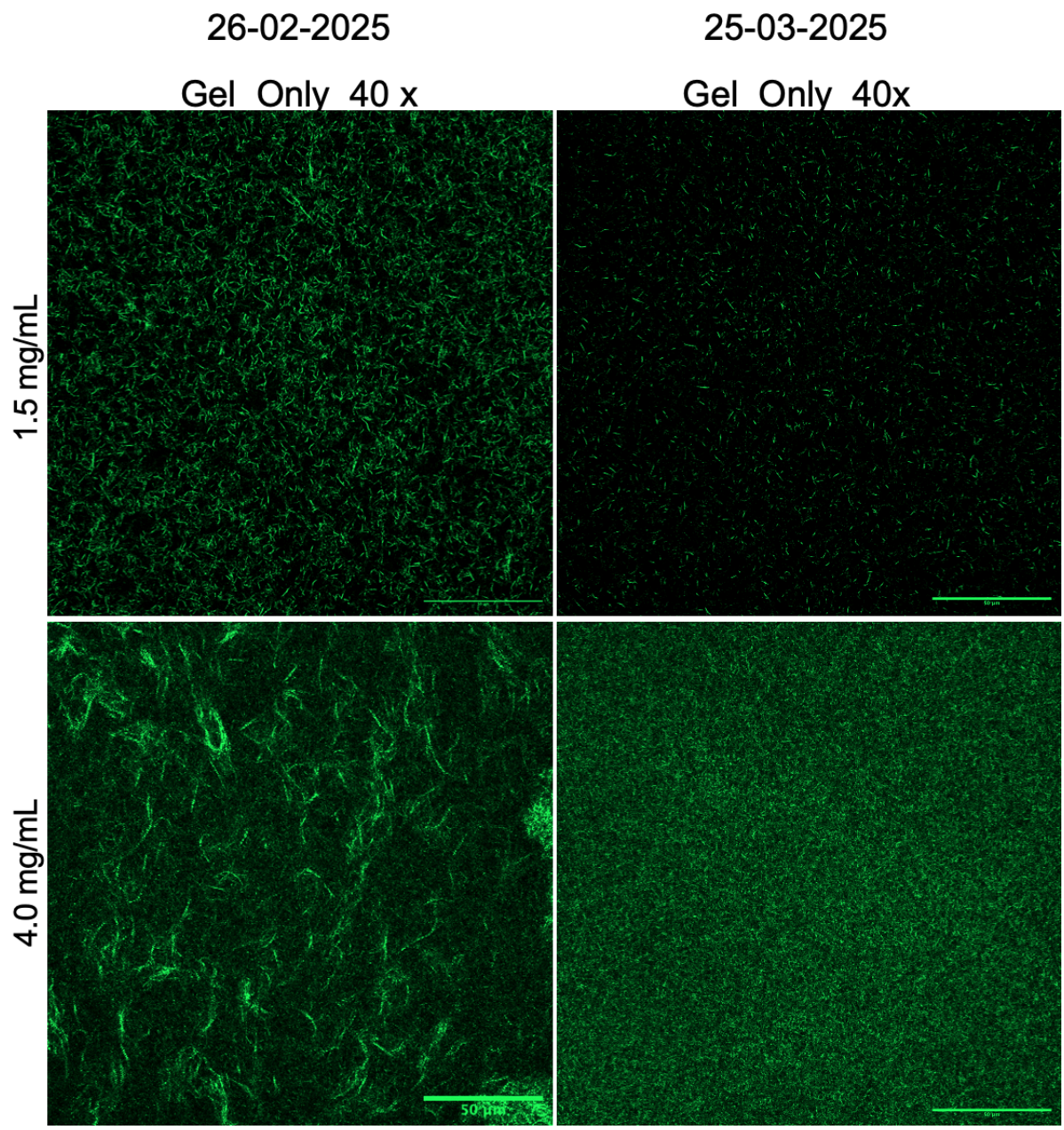

Figure F.4: Comparison between the initial gel-only experiment and a later one following the observed decline in collagen quality. Scale bars correspond to 50 µm.

Ultimately, after obtaining bovine collagen from the BioNanoScience Department at TU Delft, it became evident that the issue stemmed from the collagen itself. As shown in Figure F.5, gels prepared with the borrowed bovine collagen (using both Protocol I and Protocol II) exhibited clearly visible fibers, with Protocol I producing slightly more distinct results. In contrast, gels prepared with rat tail collagen showed no visible fibers, regardless of the protocol used, and despite previous results demonstrating that Protocol I should produce clearly visible fibers. This confirmed that the degradation in gel quality was due to the rat tail collagen. As a result, all subsequent experiments were conducted using bovine collagen and protocol I.

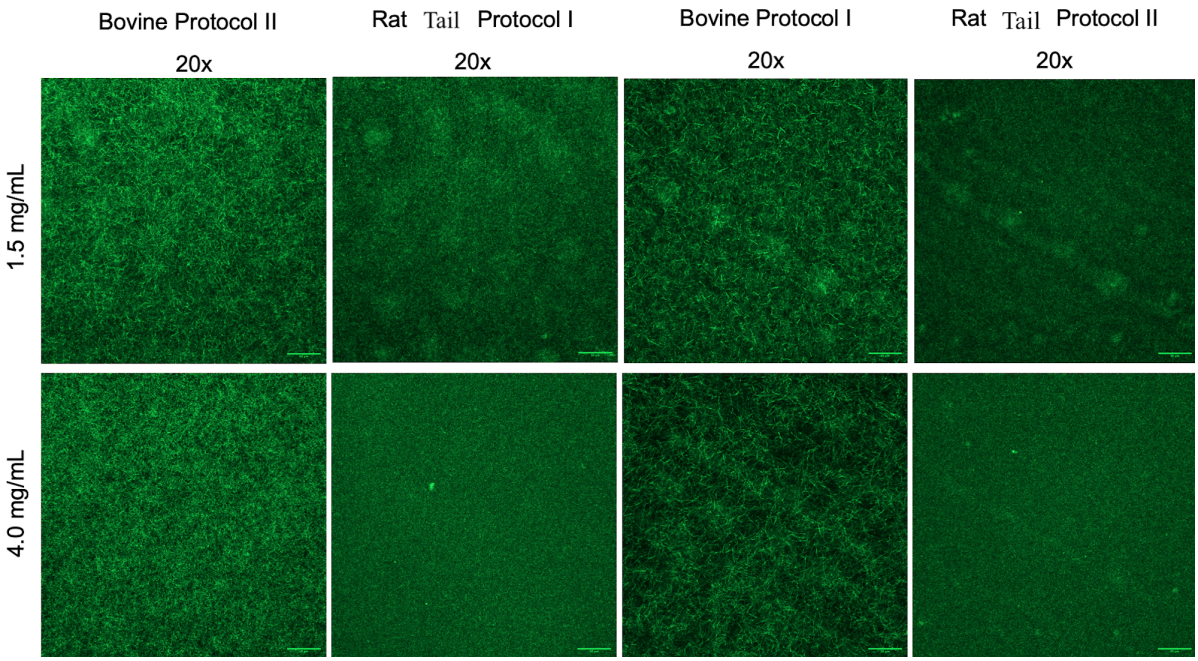

Figure F.5: Troubleshooting with bovine collagen and Protocol II. Scale bars correspond to 50 µm.

According to Corning itself, the collagen should remain stable for at least three months post-shipment (when stored at 4°C), which includes approximately two weeks in transit, leaving an expected minimum of 2.5 months of usability [65].
Possible reasons for the sudden decline in collagen quality could be:

- Contamination
- Batch-to-Batch variability
- Improper storage conditions during shipping/handling

The collagen is tested for bacteria, fungi and mycoplasma before shipping [65]. Given that experiments were performed aseptically, in a biosafety cabinet, it seems unlikely that contamination would be the problem.

The other two potential causes cannot be directly verified. In practice, the collagen remained functional for only one month, falling short of the expected stability window.

G

Aspect Ratio

The effect of the aspect ratio in this study provides insights into how spheroid shape changes in response to different collagen environments, reflecting underlying biological processes such as invasion, matrix remodeling, or mechanical constraint. It is defined as the ratio of the major to minor axis of the spheroid, and serves as a proxy for shape deformation, where a value near 1 indicates a near-perfectly round spheroid, and higher values suggest elongation or asymmetry. Variations in aspect ratio can indicate invasive behavior, as cells extend outward and disrupt spheroid symmetry, or they may reflect mechanical constraints imposed by a denser matrix that prevents shape deformation.

In the 1.5 mg/mL rat tail collagen, only the heterospheroids exhibited noticeable changes in aspect ratio (Figure G.1). In the 4.0 mg/mL rat tail collagen, only mono 4T1 spheroids showed slight variations (Figure G.2). At 2.4 (Figure G.3)and 3.3 (Figure G.4) mg/mL bovine collagen, all three spheroid types displayed slight changes in aspect ratio.

The observation that heterospheroids in 1.5 mg/mL rat tail collagen show some aspect ratio changes suggests active interaction with and remodeling of the matrix, while limited aspect ratio variation in the 4.0 mg/mL rat tail collagen implies more constrained behavior. Additionally, differences between spheroid types, such as mono 4T1 versus mono NIH3T3, highlight how cancer cells and fibroblasts contribute differently to matrix interaction, with fibroblast-rich conditions potentially preserving structural cohesion. Therefore, tracking aspect ratio changes helps contextualize how cellular composition and matrix properties influence spheroid morphology and invasive dynamics.

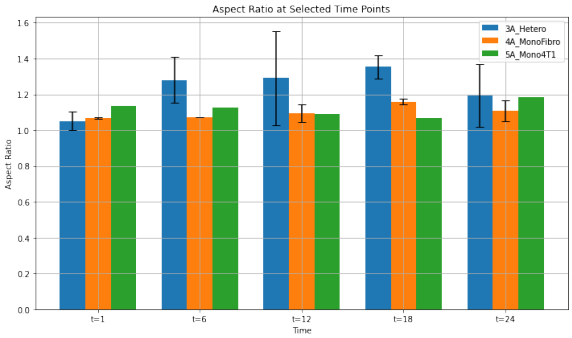

Figure G.1: Aspect Ratio for 1.5 mg/mL collagen

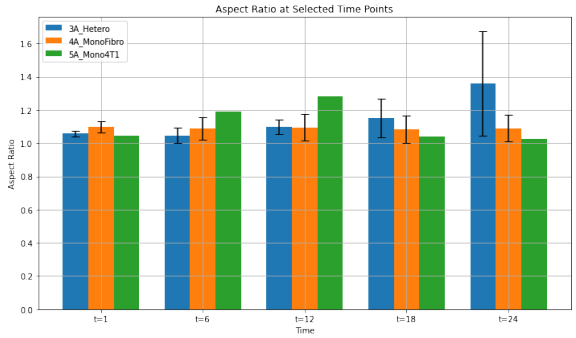

Figure G.2: Aspect Ratio for 4.0 mg/mL collagen

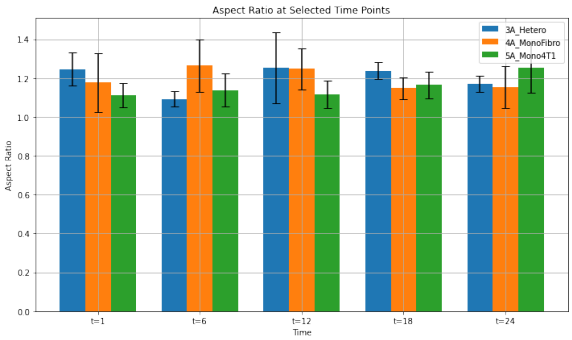

Figure G.3: Aspect Ratio for 2.4 mg/mL bovine collagen

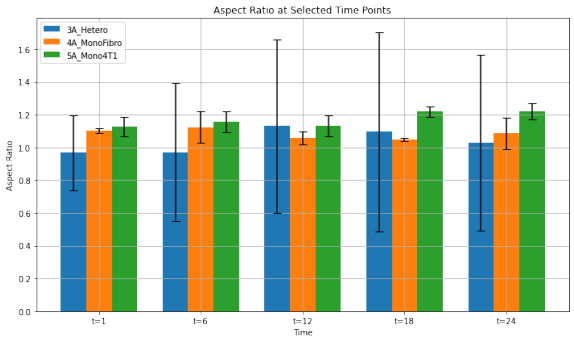

Figure G.4: Aspect Ratio 3.3 mg/mL bovine collagen

H

Spheroid Architecture

In the 1.5 mg/mL gel condition, the separated (“split”) 4T1 cells (Figure H.1C) did not exhibit the same aggressive behavior as the mono 4T1 spheroids (Figure 4.2C), suggesting that the presence of NIH3T3 fibroblasts or the structural context of heterospheroids might suppress or alter 4T1 cell invasiveness in such low concentration matrices.

The split NIH3T3 cells (Figure H.1B) could not be reliably compared to mono NIH3T3 spheroids (Figure 4.2B), as their measurements were inconsistent and lacked interpretable trends, likely due to challenges in segmentation or tracking when cells are no longer confined within a compact spheroid structure. Interestingly, both split 4T1 and split NIH3T3 cells show a decrease in signal over time. While segmentation or tracking challenges, particularly once cells disperse from the compact spheroid structure, could contribute, photobleaching is another possible explanation. Heterospheroid cells were imaged twice with the laser, potentially increasing their sensitivity to repeated exposure and compromising fluorescence signal quality. This is supported by the fact thta the monospheroids (Figure 4.2) did not illustrate loss of signal.

In the 4.0 mg/mL gel condition, the split 4T1 cells (Figure H.2C) and the split NIH3T3 cells (Figure H.2B) closely resembled the behavior of the monospheroids (Figure 4.6C, B). Similar to the 1.5 mg/mL split conditions (Figure H.1), both both split 4T1 and split NIH3T3 cells show a decrease in signal over time.

In both the 2.4 mg/mL (Figure H.3) and 3.3 mg/mL (Figure H.4) bovine collagen conditions, the split 4T1 cells followed a similar growth pattern to mono 4T1 spheroids (Figure 4.7C, Figure 4.8C). The split NIH3T3 cells were particularly difficult to analyze due to a pronounced decrease in fluorescence signal and their dispersion beyond the compact spheroid structure.

Distinguishing and separately analyzing the split 4T1 and NIH3T3 cell populations within the heterospheroids proved particularly challenging. As the experiment progressed, signal loss, likely due to photobleaching, led to frequent segmentation errors. In many cases, the reduced signal prevented accurate cell boundary identification, making it difficult to track individual populations over time. These limitations ultimately affected the reliability of quantitative analyses, particularly for dynamic behaviors such as migration or dispersion outside the core spheroid structure.

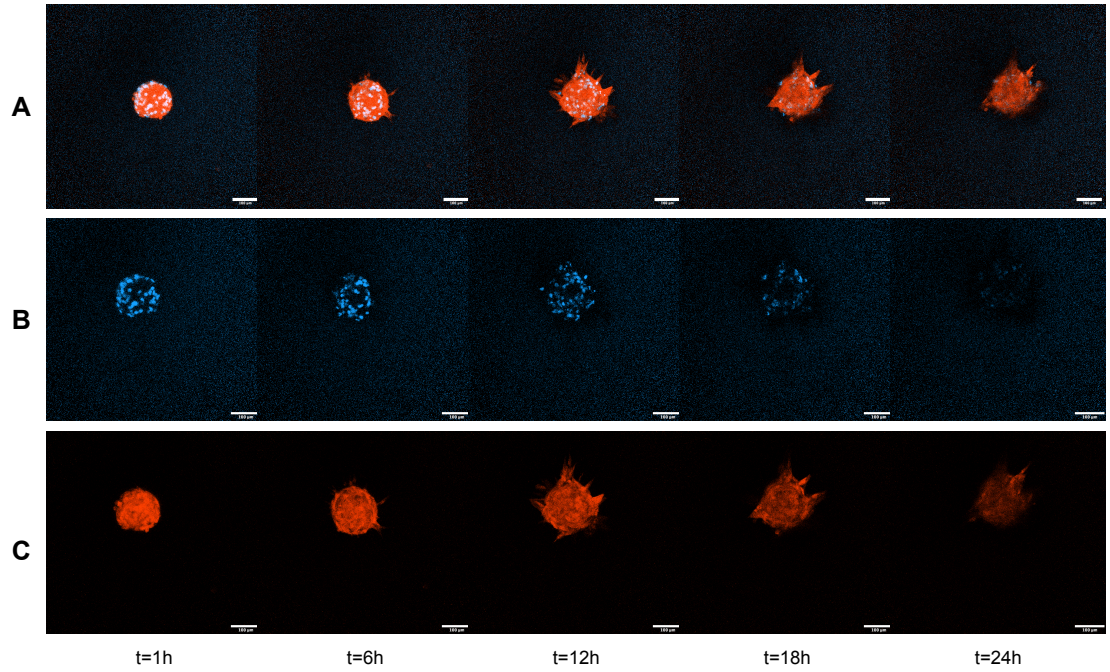

Figure H.1: Temporal progression of 1:1 heterospheroids in 1.5 mg/mL rat tail collagen gel. x-axis illustrates time in hours. A) Heterospheroids (1:1), showing the evolution from early compact structures to more irregular and invasive shapes. B) The split NIH3T3 from the heterospheroids C) The split 4T1 from the heterospheroids. Scale bars correspond to 100 µm.

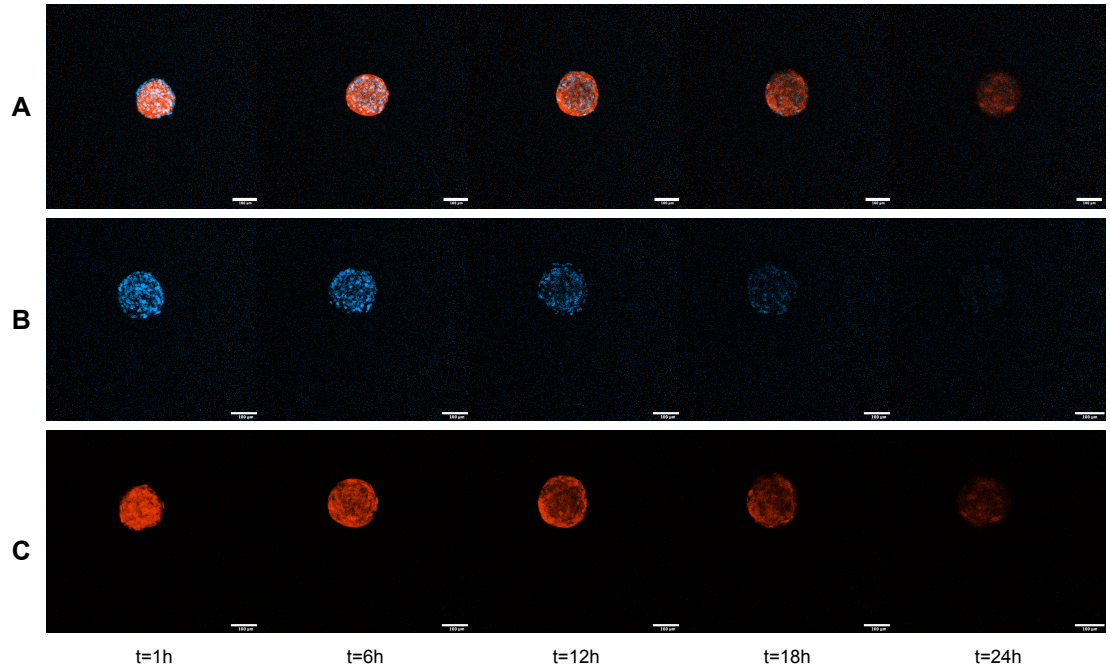

Figure H.2: Temporal progression of spheroids in 4.0 mg/mL rat tail collagen gel. x-axis illustrates time in hours. A) Heterospheroids (1:1), showing compact structures throughout the 24 hours. B) The split NIH3T3 from the heterospheroids C) The split 4T1 from the heterospheroids. Scale bar corresponds to 100 µm.

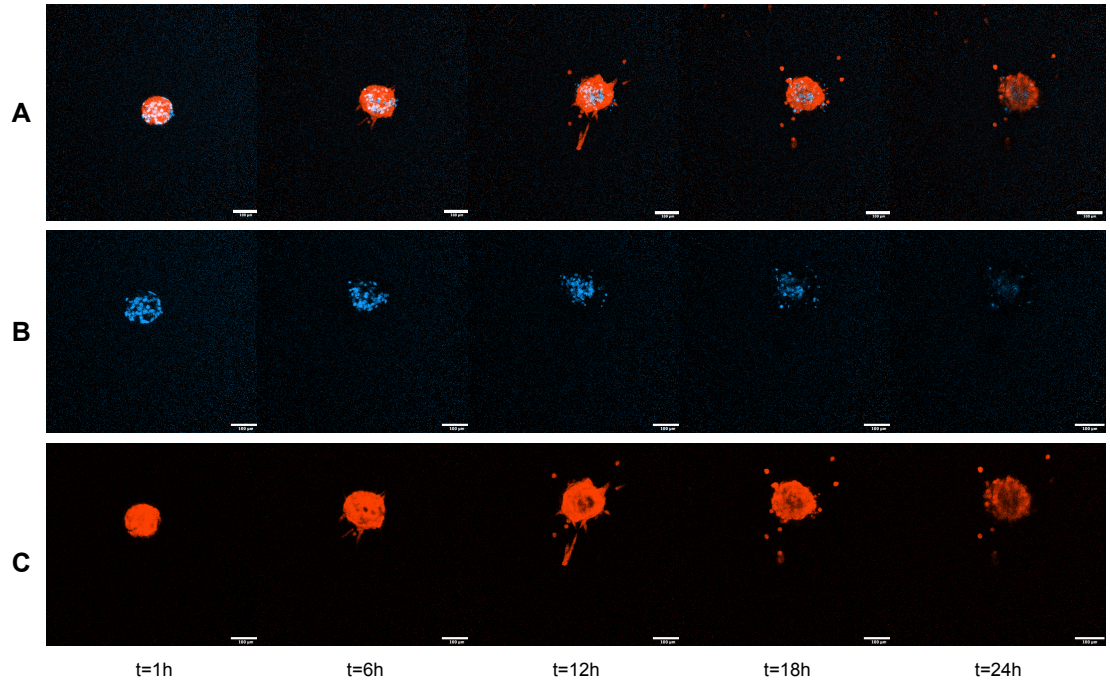

Figure H.3: Temporal progression of spheroids in 2.4 mg/mL bovine collagen gel. x-axis illustrates time in hours. A)Heterospheroids (1:1), showing the evolution from early compact structures to more irregular and invasive shapes. B) The split NIH3T3 from the heterospheroids C) The split 4T1 from the heterospheroids. Scale bars correspond to 100 µm.

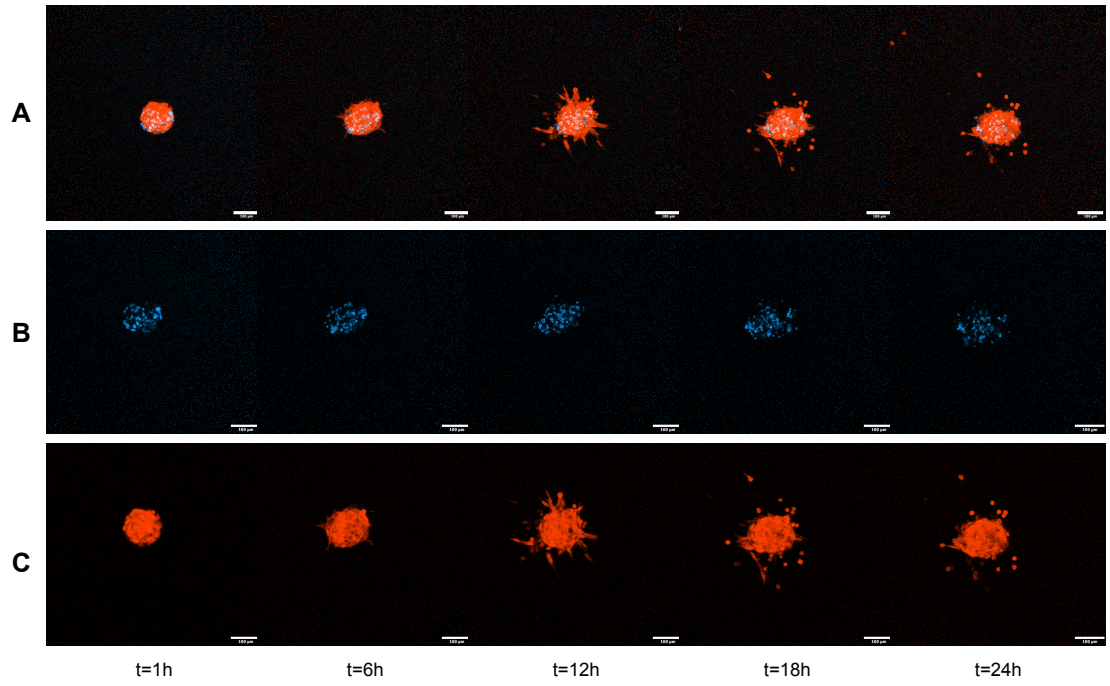

Figure H.4: Temporal progression of spheroids in 3.3 mg/mL bovine collagen gel. x-axis illustrates time in hours. A)Heterospheroids (1:1), showing the evolution from early compact structures to more irregular and invasive shapes. B) The split NIH3T3 from the heterospheroids C) The split 4T1 from the heterospheroids. Scale bars correspond to 100 µm.